東京大学
THE UNIVERSITY OF TOKYO

Doctoral Dissertation (Digest version)

博士論文（要約）

Research on Integrated Optical Phased Arrays for High-Resolution Imaging

（高分解能イメージングに向けた集積光フェーズドアレイに関する研究）

令和４年 12 月 1 日　提出

指導教員　種村拓夫 准教授

東京大学大学院工学系研究科
電気系工学専攻

福井 太一郎

Abstract

Optical beam steering device is a fundamental building block of various optical sensing and communication system, including light detection and ranging (LiDAR), bioimaging systems, photonic switching, free space optical communication, and so on. While conventional beam steering devices based on the mechanical rotation of mirrors have been widely deployed, they suffer from inherent disadvantages originating from their mechanical nature, such as poor reliability, short lifetime, poor tolerance against mechanical perturbation, low speed, and large device size. Therefore, non-mechanical beam steering devices based on integrated photonics technology have been widely studied to overcome these issues. In particular, the optical phased array (OPA) is a promising candidate since it does not require external optics and can realize seamless and on-demand beam steering. OPAs realize beam steering by emitting precisely phase-controlled light from N antennas. By leveraging the electro-optic phase shifters available on the integrated photonics platform, OPAs can realize high-speed beam scanning of over hundreds of MHz. Furthermore, the light sources, optical detectors, and the driver circuit can be integrated with the beam steering functionality on an ultra-compact semiconductor chip by leveraging advanced integration technologies.

One of the daunting challenges of the OPA is the difficulty and cost of scaling the number of phase shifters N. Since the number of resolvable points of a conventional uniformly spaced OPA (UOPA) is almost equal to N, it is mandatory to scale N to $1,000 \sim 10,000$. However, issues such as packaging, wiring, driver circuit complexity, and power consumption become prominent when N becomes large. In particular, the control of the optical phase becomes a critical issue. Due to several reasons, such as fabrication-induced optical phase errors, crosstalk between phase shifters, and the performance variation of the phase shifters, it is highly challenging to control an OPA deterministically. In current laboratory experiments, the driving condition of the phase shifters is derived based on iterative optimization algorithms with feedback from the observed output wavefront. Such optimization will become superlinearly complex at larger N. To realize deterministic control of OPAs, which is mandatory to deploy OPAs in practical systems, photonic circuits for optical phase monitoring are required. However, realizing such an optical phase monitoring circuit will also become costly at large N as well.

In this work, in order to alleviate such issues, we propose and demonstrate a novel class of OPA: the non-redundant OPA (NROPA). In the NROPA, the optical antennas are located based on the non-redundant array (NRA) concept, where duplication of displacement vectors between the position of the antennas is eliminated. Thanks to the NRA concept, the autocorrelation function of the electric field distribution at the OPA output plane can be broadly distributed with minimal N. As a result, an ultimately large number of resolvable points scaling with N^2 can be attained, which is in clear contrast to the case of UOPA , where the number of resolvable points scales only with N. In the NROPA, N can be minimized for a given number of resolvable points, therefore, the complexity and difficulty induced by increasing N can be minimized.

First, we study the FFP theoretically in depth in order to clarify the requirements for realizing a large number of resolvable points for a given N. The relationship between the near field pattern (NFP) $E(\mathbf{r})$, far field pattern (FFP) $F(\mathbf{\Theta})$, the intensity distribution $I(\mathbf{\Theta})$ of the FFP, and the autocorrelation function $\mathscr{R}_{EE}(\mathbf{\Delta})$ of the NFP is discussed. The importance of judiciously engineering the location of the antennas so that $\mathscr{R}_{EE}(\mathbf{\Delta})$ distributes broadly as possible. We introduce the NRA, which is a class of arrays that width and flatness of $\mathscr{R}_{EE}(\mathbf{\Delta})$ can be maximized for a given N by locating the antennas based on it. We present systematic numerical analysis to support our theory and to clarify the advantages and disadvantages of the NROPA concept.

We then designed and fabricated a silicon photonic NROPA chip to demonstrate the concept experimentally. The silicon photonic OPA was a 2D NROPA with its 127 antennas located based on a Costas array. In order to characterize the chip, we built an experimental setup consisting of the OPA chip, lens system, and driver circuit. The experiment system was carefully built so that the beam steering characteristics of the OPA chip could be accurately evaluated. A nice and sharp beam was obtained and steered by optimizing the driving signals of the phase shifters. The obtained FFP showed excellent agreement with the theory. The number of resolvable points was estimated to be ~19,000 points, the largest number reported to date for an OPA operating at a single wavelength, despite the relatively small number of antennas.

Next, we investigate the use of NROPA in the speckle-based single-pixel imaging (SSPI) scheme. In the SSPI, the optical phase shifters could be driven by pseudo-random signals, and therefore the complexity of driving the OPA can be further simplified. We comparatively and systematically investigate SSPI using NROPA and UOPA theoretically and numerically. We quantitatively derive the number of resolvable points for each case based on theory and support it from numerical analysis. As a result, a significant improvement in the number of resolvable points can be attained by employing the NROPA, as long as the signal-to-noise ratio of the system is sufficient. We then build an experiment setup to study SSPI using NROPA. The

experiment setup including the optical system and the chip is improved for the SSPI. Although the SSPI is yet to be demonstrated experimentally, it should be possible by solving the issues underlying in the current setup.

Finally, we design and characterize an OPA with an integrated photonic circuit for on-chip optical phase monitoring. In order to deterministically control the OPA chip, it is mandatory to monitor the optical phase propagating through all waveguides due to the inherent optical phase error induced by fabrication errors and crosstalk between phase shifters. The optical phase monitoring circuit is highly compatible with the NROPA concept; an OPA with $O\left(N^2\right)$ resolvable points can be deterministically controlled with only N phase monitoring ports. We first theoretically and numerically study the required optical phase monitoring accuracy and photocurrent detection accuracy. We then design and characterize a silicon NROPA with on-chip phase monitors. Clear matching between the retrieved optical phase and the FFPs is successfully observed.

Through this series of work, we have investigated the possibility of minimizing the complexity and difficulties of implementing and controlling an OPA for a given number of resolvable points. We have theoretically, numerically, and experimentally studied various strategies, including the NROPA, SSPI, and phase monitors. In particular, the NROPA and the related theoretical discussions should provide an in-depth understanding of the widely studied non-uniform-array-based OPA, which until today suffered from the lack of theoretical understanding and employed iterative optimization or brute-force strategies for the array design. The SSPI would be a supplemental strategy to further simplify the driving complexity, and the phase monitor should open up the pathway towards on-chip deterministic control of OPA.

Contents

CHAPTER 1

INTRODUCTION

1. Beam steering devices

A beam steering device is a device that scans the propagation direction of the light. It is a critical building block of various optical sensing, projection, or communication systems with complex functionalities. Traditionally, optical beam scanning was realized by mechanical scanning of a mirror. Here, we start from briefly reviewing the vast application of beam scanning devices. Many emerging applications have arisen from the drastic change in the social and technological environment in the past few decades. As a result, it is beginning to become difficult to meet the demand for beam steering technology just by traditional mechanical devices.

Light detection and ranging (LiDAR) [1], which is an optical counterpart of RADAR (radio detecting and ranging), is one of the most typical and demanding applications that requires beam steering. LiDAR is a technology to measure the depth information of the target, i.e., how far the surrounding objects are. Acquisition of such depth information can be realized by utilizing a pulsed light source [time of flight (ToF) method] or the frequency-modulated continuous wave (FWCM) light source as a physical probe to sense the target[*1]. In either case, typically, the light source needs to be steered in order to acquire a 2D map of the depth information so that thorough information of the surrounding scene can be obtained[*2].

[*1] There are two main methodologies to measure the distance from the target. The first method is the ToF method. The target is probed by an optical pulse launched from the system, and the light reflected from the target is detected by a photodetector. Thanks to the finite speed of light, the time the light took to bounce back from the target is a realistically measurable delay. Another method is the frequency-modulated continuous wave method (FMCW) method, where the launched light is a continuous wave laser light source with linear frequency modulation. By coherently detecting the reflected light using the local light as a reference, the distance of the target can be extracted from the beat frequency. At the cost of a relatively complex system, the FMCW method provides several unique advantages, including shot-noise-limited high detectivity, background light immunity due to the interferometric detection principle, and the availability to measure the velocity of the target.

[*2] In fact, there are two main approaches to obtaining a 2D map: the flash LiDAR or the beam steering method. Flash LiDAR, a commercially available technology, uses an array of single photon avalanche photodiodes (SPADs) to detect the reflected light. A broad area beam illuminates the scene, and a lens system is used to image the scene to the SPAD-array plane, just as in a normal camera. Although this is a realistic and cheap approach, the optical power per detection pixel becomes weak. Moreover, for systems that will co-exist with

The distance information is critically important for realizing autonomous systems such as autonomous vehicles and automated factories, so as to prevent the machine from accidentally crashing into surrounding objects, such as the pedestrian*3. There are now numerous political, industrial, and technological concepts, such as Society 5.0 [2] and Industry 4.0 [3], provisioning that in the near future, such highly automated systems will be implemented everywhere, represented by autonomous vehicles. However, the cost, size, and power consumption of the current beam steering devices based on the mechanically rotating mirrors are problematic for LiDARs to be widely deployed everywhere. Moreover, the mechanical nature of the current beam scanning devices limits the reliability of the system since it is weak to mechanical vibrations, and the device lifetime is limited. Also, the relatively slow scanning speed of the mechanical beam steering devices is currently limiting the frame rate of the system.

Another application where beam steering devices are required is the advanced imaging systems represented by the bioimaging systems. In bioimaging systems, the target information is obtained by various means, including fluorescence or Raman signals [4–6]. In such systems, it is commonly required to employ a beam scanner to scan the probe light or/and the signal light so as to obtain a 2D image. Beam scanners in such systems sometimes make the system bulky and limit the frame rate of the imaging due to the limited operation speed. Therefore, it is desirable to realize beam scanning devices that can overcome these issues so as to decrease the system cost or improve the performance of the systems. Other applications, such as displays for augmented reality or virtual reality also demand non-mechanical, compact, and high-speed beam scanners as well [7]. Free space optical communication is another emerging application that requires beam steering [8]. In particular, the inter-satellite communication will require non-mechanical beam steering devices since the beam scanning device's mechanical rotation will directly impact the position and the attitude of the satellite itself*4.

From these emerging application, it is now becoming increasingly important to realize non-mechanical beam steering devices that are compact, low cost, high speed, and high-reliability. As an alternative approach, various beam scanners based on micro-electro-mechanical-systems (MEMS) have recently emerged [9–11]. These MEMS-based technologies could be advantageous compared to previous mechanical beam scanners due to significantly reduced device size, improved operation speed, and high manufacturability. However, due to their mechanical

humans, the eye safety issue bounds the total optical power that can be launched from the light source. As a result, it is difficult for flash LiDAR to realize long-distance ranging. In addition, the flash LiDAR is currently incompatible with the FMCW method, as we do not have a massive array of coherent receivers that can efficiently couple to free space optical light. Therefore, the beam steering method is of siginificant importance.

*3 However, the depth information is challenging to acquire accurately from the image obtained from a camera. Moreover, to make the system secure and robust, it is highly desirable to acquire depth information by several means. In particular, LiDAR is highly promising due to the direct detection of the distance and the high spatial resolution owing to the short wavelength of light.

*4 Conventional non-mechanical beam scanning by liquid crystal suffer from poor tolerance against cosmic radiation.

nature, they still inherently suffer from poor tolerance to mechanical vibrations and short lifetime, resulting in poor reliability. In addition, other disadvantages, such as high operation voltage, also exist. Moreover, for MEMS mirrors, an inherent tradeoff between operation speed and aperture size could be another problem since MEMS mirrors utilize mechanical resonance. This resonant nature accompanies other issues, such as the impossibility of on-demand raster scanning and incompatibility with the FMCW method owing to the incoherence induced by the MEMS mirror[*5].

2. Optical phased arrays (OPAs)

As we have seen in the previous section, conventional mechanical beam scanners suffer from various issues, including cost, size, speed, reliability, and so on. Integrated photonics technology is promising for realizing non-mechanical beam scanners and alleviating the above issues. In the integrated photonics platform, various optical components, including optical waveguides, optical couplers, light sources, phase shifters, and so on, can be integrated on a single chip [12–16]. By leveraging such building blocks, non-mechanical beam steering devices can be realized. Many configuration has been previously widely proposed and studied, such as the lens-assisted focal plane switch array [17–19] and slow-light-grating [20–27].

In particular, the optical phased array (OPA) (Fig. 1.1) is one of the promising non-mechanical beam steering devices that can be realized using integrated photonics technology [28–30]. OPA realizes optical beam steering by forming an equal phase plane at the output (see Fig. 1.2). In the OPA, first, the input light is split to N waveguides by a $1 \times N$ splitter, which is typically realized by cascaded 1×2 multimode interference (MMI) couplers [31] or by a single $1 \times N$ star coupler [32]. The light propagating through each waveguide is phase-controlled independently[*6] by the phase shifter implemented in each waveguide. The light is then emitted from respective optical antennas (Fig. 1.1 and Fig. 1.2 show the case of end-fire emitting for the sake of simplicity). When an equal phase plane is formed at the output plane of the OPA, the light will be steered to the corresponding direction through Fraunhofer diffraction [33], via which the optical wavefront will experience Fourier transform. The output far-field pattern (FFP) from an OPA is depicted in Fig. 1.3. The output wavefront will become periodic due to the periodicity of the antenna layout[*7]. This period of the FFP typically determines the

[*5] This incoherence originates from the fact that the mirror does not stop each time.

[*6] In principle, the phase shifters do not necessarily have to be phase-controlled independently, but in reality, due to phase error issues and thermal crosstalks, as we discuss later, it is typically required to control all the phase shifters independently.

[*7] This periodicity can be eliminated by non-uniformly arranging the antennas so that destructive interference will occur at the location of higher order diffraction peak [34, 35]. Moreover, aliasing-free beam steering will be possible by locating the antennas with a pitch smaller than half the wavelength. Commonly, it is challenging since the coupling between adjacent waveguides will become prominent at such a small waveguide pitch.

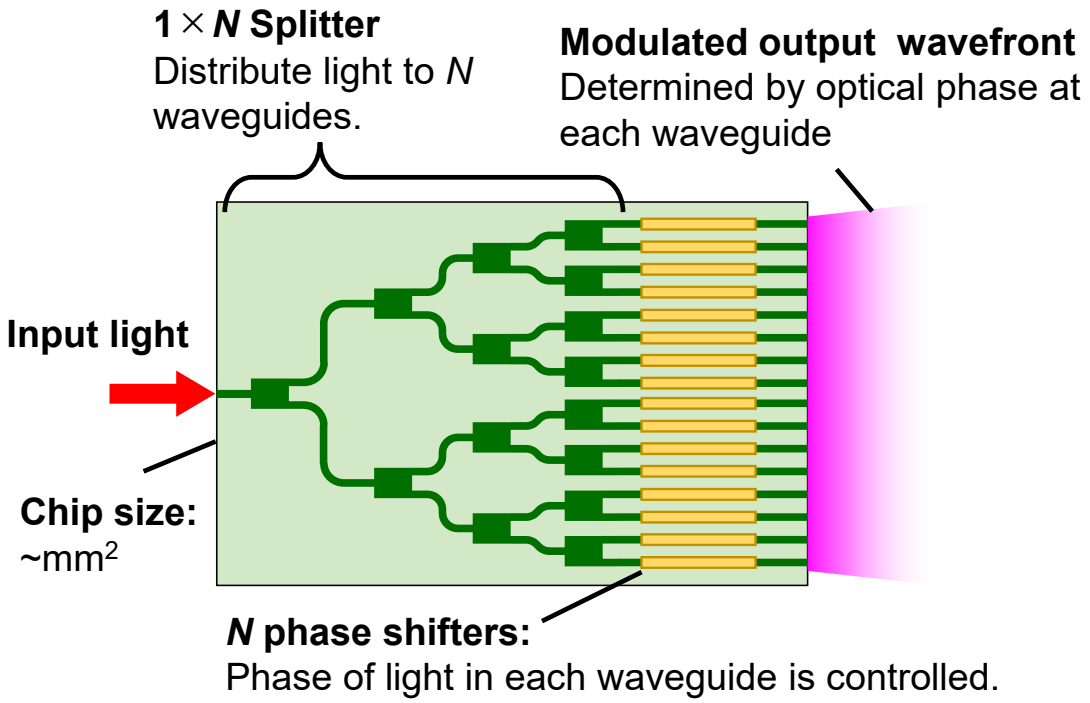

Fig. 1.1: Schematic of an integrated OPA.

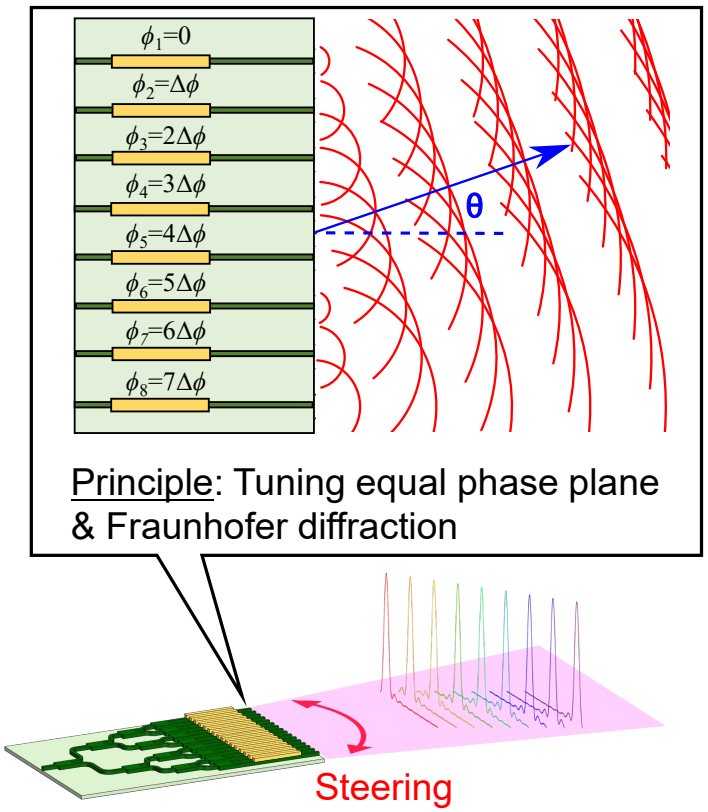

Fig. 1.2: Schematic of beam steering using an OPA.

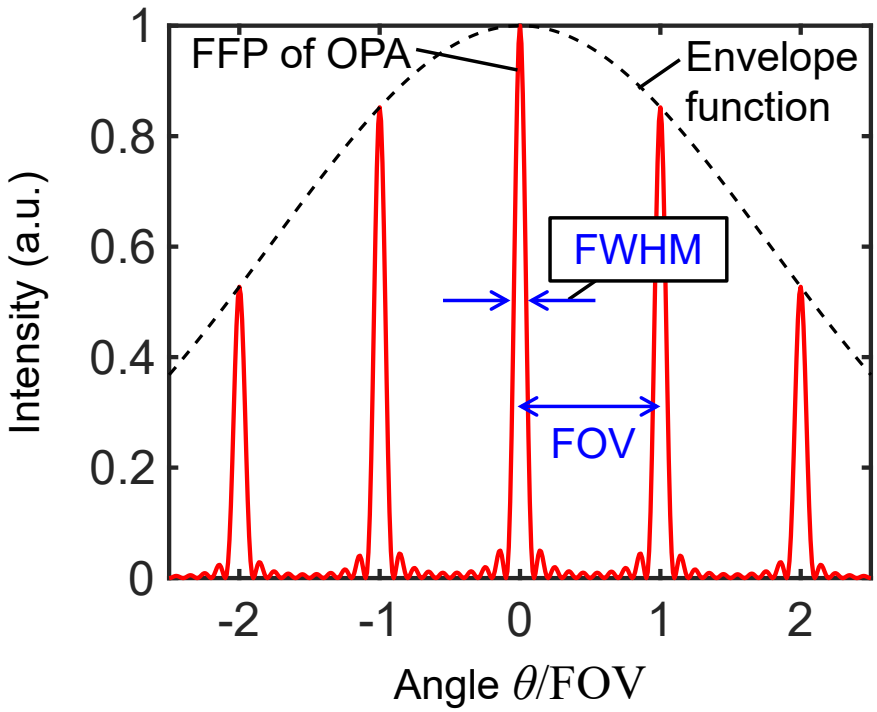

Fig. 1.3: Schematic of the FFP of an OPA.

steerable range of the beam and is commonly called the field of view (FOV) of the OPA. The OPA can function not only as a transceiver to emit the light to a specific direction but also can function as an receiver to selecetively receive the light from a specific direction.

There are mainly two configurations for an OPA: the 1D OPA or the 2D OPA. For a 1D OPA, the light is typically emitted from a long grating coupler (typically $>$ 1 mm$_{*8}$) based on waveguides with periodic perturbations. In such configuration, the 2D steering can be achieved by combining the wavelength scanning scheme; while the axis along the direction of the array can be steered by tuning the optical phase, the steering across the other direction can be accomplished by leveraging the wavelength-dependency of the emission angle of the grating emitters and a wavelength-tunable light source. On the other hand, 2D OPA, where

Several feasible methods, including the use of bent waveguides [36] or index-mismatched waveguides [37,38], have been proposed and shown to be effective in the case of 1D OPA. However, they are typically compatible only with the end-fire 1D OPA [39]. For the case of 2D OPA, it is challenging to realize such an aliasing-free waveguide pitch due to the difficulty of routing waveguides and the difficulty of designing sub-wavelength-sized antennas that could efficiently couple the light from the free space to the waveguide.

$_{*8}$ The longer the grating coupler becomes, the sharper the FFP will become. Therefore, in order to increase the number of resolvable points, it is effective to employ a long grating by very weak perturbation [40]. However, we should note that as the grating couplers become longer, the required effective refractive index accuracy of the grating emitters will increase; deviation in refractive index change will lead to a slight change in the emission angle, and as the beam becomes sharper, the tolerable emission angle will decrease. If the fabrication-induced refractive index deviation is prominent, the emission angle from the antennas will no longer be common for all the antennas for a given wavelength, and therefore, it will end up in significantly degraded beam profile.

the antennas are located in a 2D array, can realize 2D beam steering at a single wavelength just by tuning the optical phase. However, the routing of waveguides in a planar configuration and design of micron-scale antennas (typically realized by high-index-contrast gratings) with high-coupling efficiency and broad radiation angle is challenging [41] compared to the 1D OPA.

3. Research trends of OPA

The pioneering work of on-chip beam deflection was reported almost half a century ago, based on the $LiNbO_3$ platform [42, 43]. Semiconductor-based integrated OPA was then reported based on the GaAs/AlGaAs platform [44–46]. However, at the initial stage of the research, there was no concrete application of OPAs, and the research was rather motivated by scientific curiosity. In terms of application-oriented research, OPAs as a photonic switch for packet routing was explored in the late 1990s to early 2010s [47–54][*9], owing to the unique scalability of OPAs in terms of insertion loss compared to the cascaded switch strategy [55].

The research of OPAs for performing beam steering in the free space then bloomed around 2010 [56–58]. The demonstration of a large-scale OPA ($N = 64$ for an active device and $N = 4096$ for a passive device) based on the silicon photonics technology has then opened up the possibility of vast applications, including LiDAR and free space optical communication. Furthermore, striking news that an American start-up company, "Quanergy," announced the commercialization of non-mechanical LiDAR based on OPAs at 2016[*10], which further accelerated the research of OPAs. As a result, the research on OPA has accelerated rapidly until today.

There has been massive progress in the development and applications of OPA in the past decade. Thanks to the CMOS compatibility of OPAs, the electronic driver circuit can be monolithically integrated with an OPA [59–61]. The monolithic integration of laser light sources and optical amplifiers is also possible by leveraging the III-V/Si hybrid integration tecnology [62–64]. We also should note that such monolithic integration of light sources has also been demonstrated using the monolithic III-V platform [65] and should be potentially possible for many other platforms and wavelength ranges by integrating the III-V materials through the recently emerging hybrid integration technologies such as transfer printing and direct wafer bonding [66–68]. High-speed operation (> 100 MHz) of OPAs is also demonstrated by employing the electro-optic phase shifters [64, 69–72]. In terms of application, ranging based on the FMCW method has also been experimentally demonstrated [73–75]. It also can

[*9] However, to the best of my knowledge, OPAs or any photonic switches have not been deployed in commercial routers to date, and they are all electrical.

[*10] However, to the best of my knowledge, solid state LiDAR from Quanergy has not yet been deployed to date.

potentially be applied to the time-of-fligh LiDAR [76]. Moreover, many potential applications of OPA, such as optical imaging [77–85], free space optical communication [74], optical projection [69,74,86], and photonic switching [47–54], have been explored. Operation at versatile wavelengths, including visible [87–89], near-infrared [88–91], and mid-infrared [92–94], has also been demonstrated by leveraging various integration platform so as to expand the potential application of OPA. Although the weak optical power due to large insertion loss and poor power budget of 220-nm thick silicon photonics platform was problematic [*11], which is critical for long-distance ranging applications like LiDAR for autonomous vehicles, recently, handling of high power (peak output power of >700 mW) has also been demonstrated by leveraging silicon nitride waveguides [95] [*12].

4. Challenges

One of the daunting challenges of the conventional OPA is the realization of high spatial resolution without increasing the complexity and cost of the system.

In a traditional uniformly-spaced OPA (UOPA) where the antennas are located based on a uniformly spaced grid, the number of resolvable points [defined by the ratio of field of view (FOV) and the full-width-at-half-maximum (FWHM) (see Fig. 1.3), which describes the number of beams that can be packed within the FOV] is almost equal to N. Consequently, in order to attain a sufficiently large number of resolvable points (1,000~10,000) required for practical applications, N must be accordingly. Therefore, massive effort has been paid to scaling the array [60, 71, 74, 75, 89, 98, 99].

On the other hand, various issues impose significant diffiuculty in scaling N, and many of them become superlinearly serious as N increases. For example, packaging the chip becomes pretty challenging. When N is scaled to >1,000, it is not trivial at all to wirebond independently to all the phase shifters. Consequently, in [75], eight chips of application specific integrated circuit (ASIC) had to be directly flipchip-bonded on the OPA chip in order to manage the 8, 192 phase shifters, which obviously induces significant penalty in cost and manufacturability. Potentially, such an issue may be alleviated by fully integrating the driver circuit on the same chip as OPA. However, the complexity of realizing synchronously controllable digital-to-analog converters (DACs) with 1,000~10,000 parallelly operating ports and with high precision (typically > 10 bits) still remains and will impose non-trivial difficulty

[*11] Typically, the input optical power needs to be as low as ~15 dBm for a 220-nm-thick silicon photonic platform, mainly due to extremely strong optical confinement and relatively strong multi-photon absorption of silicon.

[*12] The multi-micron-thick silicon photonics platform [96] should also be promising for high-power handling due to the larger optical mode diameter, which can pave the way towards deploying silicon photonic OPA for solid-state LiDAR. Start-up called SiLC [97] is trying to realize silicon photonic FMCW LiDAR based on the multi-micron silicon photonics platform.

in scaling N.

The power consumption of the phase shifters is another issue. The thermo-optic phase shifters are the currently dominant phase shifters used for silicon photonic OPAs, due to their relatively compromisable balance between cost, power consumption, voltage, optical loss, operation speed, device reliability, and footprint[*13]. Thermo-optic phase shifters typically require mW class power consumption [128–130], and thus obviously, large power consumption will be required when N is scaled. This issue could be alleviated if highly efficient, low power consumption, and highly manufacturable phase shifters are deployed. However, the electrical power consumption at the digital-to-analog converters accompanying each phase shifter exists.

[*13] Of course, the pn-junction-based carrier depletion phase shifters, which operate at the reverse bias of the pn-junction and thus consume ultralow electrical power, are readily available on the silicon photonics platform and are widely deployed for optical communication [100]. However, due to the poor trade off between the optical loss and the refractive index change of the carrier plasma dispersion effect in silicon [101–103], these modulators suffer from inherently large insertion loss and phase-dependent insertion loss. Moreover, the refractive index change induced by the carrier density change is small ($\Delta n \sim 0.002$), carrier depletion phase shifters suffer from large operation voltage (> 5 V_{pp}) and long device length (> 1 mm) for 2π phase shift. For optical communication applications, the carrier depletion phase shifters are used in the Mach-Zehnder modulator configuration, and in order to ensure linearity of the modulated signal, the phase shift induced by the phase shifters is much smaller than 2π. Moreover, the push-pull configuration [104, 105] allows for further lower voltage operation. Therefore, the limited amount of phase shift is not critical for the optical communication application. In contrast, the OPA application will require a full 2π phase shift. Therefore, implementing the carrier depletion phase shifters for OPA application is more challenging compared to the communication application. Similarly, the pn-junction-based carrier injection phase shifters [106, 107], although it enjoys a higher efficiency compared to the carrier depletion phase shifters due to the larger optical confinement factor, suffers from the large insertion loss induced by carrier plasma dispersion effect, and the current-injecting nature of it will lead to comparative electrical power consumption compared to the thermo-optic phase shifters. Silicon-based metal-oxide-semiconductor (MOS) optical phase shifters [108, 109] are a relatively promising candidate out of the phase shifters based on the carrier effect of silicon since it enjoys relatively high efficiency due to the large confinement factor and small electrical power consumption thanks to the MOS structure. However, phase-dependent optical loss is inevitable, and its relatively complicated device structure could be problematic (as far as I know, no foundry can readily integrate the MOS phase shifters for multi-project wafers). The MEMS phase shifters are emerging optical phase shifters compatible with silicon photonics and are now being studied [110–112]. The MEMS phase shifters have various advantages, such as small insertion loss and ultra-low electrical power consumption. However, to date, foundries that can readily fabricate MEMS phase shifters on commercial multi-project wafer projects do not exist (to the best of my knowledge), possibly due to its relatively complicated suspended device structure. Moreover, due to its mechanical nature, it might suffer from the same issues as the current mechanical beam scanners, such as poor tolerance against mechanical vibrations, large operation voltage, and short device lifetime. The electro-optic effect, in particular the Pockels effect, is a means to electrically control the refractive index of a material and is inherently free from phase-dependent optical loss due to its nonlinear nature. However, due to the symmetry of silicon, the electro-optic effect cannot be obtained without exotic strategies, such as inducing very large electric field [113, 114], which requires an extremely high voltage of ~ 30 V, or by inducing large strain [115, 116], which suffers from low efficiency. The III-V/Si hybrid MOS shows an extraordinary performance of low cost and high efficiency, thanks to the excellent trade off between refractive index change and optical loss of III-V materials [117–121]. However, the direct wafer bonding process and the III-V materials will induce significant penalty in cost and manufacturability (although it could be a realistic choice if the III-V/Si hybrid laser becomes a mature light source for silicon photonics since light sources will be required anyway, and the hybrid phase shifters and the hybrid lasers could be fabricated through a similar process). Other integration platforms such as thin film lithium niobate [122–124] and III-V monolithic or membrane integration platforms [125–127] could be employed to enjoy the low-loss low-power-consumption phase shifters. However, they are inferior to silicon photonics in terms of manufacturability, cost, and integrability with driver circuits, and as a result, scaling N will become problematic.

Other issues, such as larger device footprint, poor yield (due to larger device area), and increase in optical loss (due to increased optical path length), can also impose difficulty in scaling N as well[*14].

Out of the various issues, the most prominent issue is possibly the difficulty of calibrating and controlling the driving conditions of the phase shifters. In optical waveguides, the effective refractive index deviates, originating from the waveguide width deviation inevitably induced by fabrication [135, 136]. The issue of the effective refractive index deviation of optical waveguides can be mitigated to some extent by several means, such as employing wider optical waveguides [131–134, 137][*15], utilizing the multi-micron silicon photonics platform [96][*16], and employing SiN waveguides [138–140] [*17] However, it is still challenging to realize large scale optical devices with 1,000∼10,000 components with sufficient phase accuracy. Another problematic issue is the crosstalk between the phase shifters. In particular, the commonly deployed thermo-optic phase shifters suffer from significant thermal crosstalk [129, 141]. As a result, it is incredibly challenging to deterministically drive the phase shifters without calibration and monitoring.

Therefore, a calibration step is required to optimize the driving condition of the phase shifters. However, this calibration will become increasingly difficult as N increases. Most laboratory experiments employ an off-chip system to observe the far field pattern (FFP) using a camera to perform optimization. Various optimization algorithms such as hill climb algorithm [58], genetic algorithm [142], particle swarm optimization [143], deterministic-stochastic gradient descent method [144], stepwise calibration using mechanical filtering slits [145], and rotating element field vector method [146, 147], have been explored to calibrate and optimize

[*14] In fact, the phase shifters could be eliminated by utilizing the dispersive optical phased array [131–134], where only wavelength scanning is required to steer the beam. This is realized by leveraging the wavelength-dependent relative optical phase difference of light propagating through waveguides with difference optical path lengths. However, it would be challenging to implement a large-scale OPA due to the refractive index deviation, as we explain later. Moreover, it would require an ultra-widely tunable (>100 nm) laser light source, which could be costly or challenging.

[*15] By employing wide optical waveguides as wide as $2 \sim 3$ µm, the refractive index deviation induced by optical waveguide width deviation can be minimized even in the standard 220-nm-thick silicon photonics platform since the light will be confined in silicon regardless of the waveguide width. However, the impact of silicon thickness fluctuation will limit the degree of phase accuracy.

[*16] In the multi-micron silicon photonics platform, the refractive index deviation can be minimized since almost 100% of the light is confined in silicon, and therefore the effective refractive index is almost independent of the waveguide width. In fact, we believe that the multi-micron photonics platform is promising for OPA due to other reasons as well, such as ultra-low optical loss due to extremely small sidewall roughness scattering thanks to the absence of light at the interface between Si and the cladding SiO_2, high coupling efficiency with semiconductor lasers/optical-amplifiers or fibers, and the capability of handling high-power due to large mode field diameter. However, the number of foundries available for the multi-micron silicon photonics platform is still limited, and they are not as mature as the 220-nm-thick silicon photonics platform. One possible reason could be the lack of other applications originating from some missing key components: high-speed optical phase modulators and polarization handling devices.

[*17] SiN waveguides have relatively higher optical phase accuracy owing to the smaller refractive index contrast of SiN and SiO_2 compared to that of Si and SiO_2.

the driving condition of the OPA. However, all of them become superlinearly complex and difficult as N scales. On-chip phase monitoring systems that can directly monitor the relative optical phase between light propagating through adjacent waveguides can potentially alleviate such issues [65, 148]. However, again, the number of monitoring ports and difficulty of signal processing will increase with N, and therefore, it is desirable to keep N as small as possible.

One commonly employed approach is locating the antennas based on a non-uniform array [34, 35, 63, 86, 87, 149–153]. By such non-uniform-array-based OPA, the number of resolvable points can be increased without increasing N. For example, pseudo-random arrays [34], arrays generated from iterative optimization [86, 87, 153], Gaussian arrays [63], and sub-array-based non-uniform arrays [149] have been explored. For example, in the representative examples ([34] and [86]), approximately 500 resolvable points have been demonstrated for an OPA with $N = 128$. However, the current work rather relies on brute-force-like iterative optimizations, and currently, a clear understanding of the mechanism of the resolution enhancement is missing. Moreover, the ultimately achievable number of resolvable points was remains an open question.

Another possible approach is the use of speckle-based single-pixel imaging (SSPI) scheme [154–156], also known as the ghost imaging scheme [157–160], which is a class of computational imaging. By employing the SSPI scheme, the phase shifters of the OPAs no longer have to be precisely controlled and instead can be driven by pseudo-random signals. Thus, significant simplification in the driving and calibration can be enjoyed [77–79, 81–84]. Furthermore, SSPI is compatible with the compressive sensing algorithm, which can further reduce the cost of image acquisition [161–163]. However, by SSPI itself, the number of resolvable points cannot be increased [78]. Moreover, the quantitative understanding of the number of resolvable points of SSPI using OPA was still missing.

5. Research aim

In the research presented in this dissertation, we aim to construct a pathway towards realizing an OPA with a sufficiently large number of resolvable points (>1,000~10,000) without suffering from the complexity and difficulty induced by increasing N. The core concept of the research is the *non-redundant OPA (NROPA)*, where the antennas are located based on the *non-redundant array (NRA)* concept. Compared to the previous non-uniform-array-based OPAs, where the theoretical understanding was insufficient, in this work, we present an in-depth theoretical analysis to provide a deep understanding of the fundamental physics underlying the resolution-enhancement induced by the non-uniform array. We elucidate the requirements for an optimal configuration of the non-uniform array; the autocorrelation $\mathscr{R}_{aa}(\mathbf{\Delta})$ of the function describing the array layout $a(\mathbf{r})$ must be broadened, and flattened. We propose the

concept of NROPA and theoretically show that NRA is an optimal array to locate the antennas of an OPA in order to realize high spatial resolution. We then experimentally demonstrate our concept. Further simplification of the imaging scheme is investigated by employing the speckle-based single-pixel imaging scheme (SSPI), where the requirement for precise tuning of phase shifters can be omitted. Finally, we study the on-chip calibration scheme based on on-chip optical phase monitors, which is highly compatible with the NROPA concept; an OPA with a large number of resolvable points can be calibrated and controlled by the minimal number of monitoring ports.

6. Structure of the dissertation

Figure 1.4 illustrates the structure of this dissertation. The content of each chapter is described in the followings.

In Chapter 1, we have discussed the background of this research. In particular, we have discussed the OPA as a promising non-mechanical beam steering device candidate and the technical challenges in deploying OPAs in practical systems.

In Chapter 2, we present an in-depth theoretical study of the far-field pattern (FFP) of the OPA. Through the theoretical study, we point out the importance of broadening and flattening the autocorrelation function of the array layout function. To meet such requirements, we propose the NROPA, where the antennas are located based on the NRA. The concept is verified through numerical analysis, and the advantages and drawbacks of the concept are described.

In Chapter 3, we experimentally demonstrate the NROPA concept. A silicon photonic NROPA based on a Costas array with 127 optical antennas is designed, fabricated, and characterized. Ultra-high-resolution beam steering with a state-of-the-art number of resolvable points is experimentally demonstrated.

In Chapter 4, we systematically and comparatively study the speckle-based single-pixel imaging (SSPI) scheme using an NROPA or a UOPA. The number of resolvable points for each scheme is quantitatively clarified through theoretical analysis and verified through numerical analysis.

In Chapter 5, we experimentally study the SSPI scheme using an NROPA. We build and improve the experiment setup for SSPI using NROPA. We analyze the experimentally obtained speckles patterns.

In Chapter 6, we study an OPA chip with an integrated optical phase monitoring circuit. We first present a theoretical and numerical analysis of the required optical phase accuracy and the photocurrent detection accuracy. We then experimentally demonstrate clear matching of the FFP of the OPA and the optical phase extracted from the on-chip phase monitoring circuits.

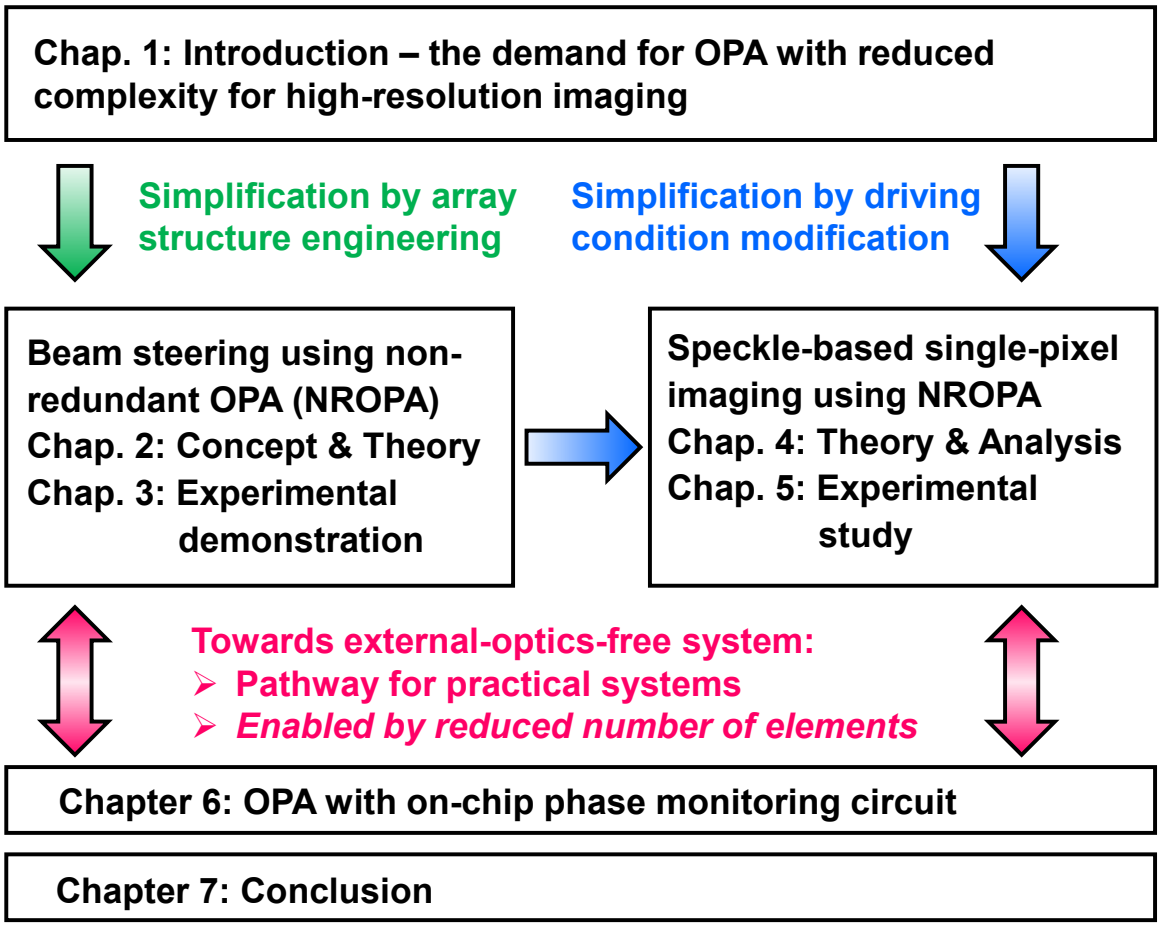

Fig. 1.4: Structure of this dissertation.

In Chapter 7, we summarize the series of work.

CHAPTER 2

PROPOSAL OF NON-REDUNDANT OPTICAL PHASED ARRAY

In Chapter 2, we start with a careful theoretical analysis of how the far-field pattern (FFP) of the OPA is determined. Through the analysis, we highlight the importance of broadening and flattening the autocorrelation function $\mathscr{R}_{aa}(\mathbf{\Delta})$ of the array layout function. Then we introduce the non-redundant OPA (NROPA), where the antennas are located based on a non-redundant array (NRA). We show that the NRA is an optimal array to obtain a sharp beam. We present some numerical analysis to support our theory.

1. Theoretical analysis of the FFP

We first start by deriving the intensity profile of the FFP and its relationship with the near-field pattern (NFP). Figure 2.1 describes the definition of the electric field distribution $E(\mathbf{r})$ and $F(\mathbf{\Theta})$ at the NFP and FFP planes, respectively. Here, $\mathbf{r} = (x, y)$ is the coordinate at the NFP plane, while $\mathbf{\Theta} = (\theta_x, \theta_y)$ denotes the lateral and longitudinal angles at the FFP. Assuming that all the optical antennas are identical, we can express $E(\mathbf{r})$ as

$$E(\mathbf{r}) = \sum_{n=1}^{N} C_n u\left(\mathbf{r} - \mathbf{r}_n\right) = u(\mathbf{r}) * \left[\sum_{n=1}^{N} C_n \delta\left(\mathbf{r} - \mathbf{r}_n\right)\right] = u(\mathbf{r}) * a(\mathbf{r}) \tag{2.1}$$

where $u(\mathbf{r})$ describes the electric field distribution from a single optical antenna at the vicinity of the emission plane, $u(\mathbf{r}) * a(\mathbf{r}) \equiv \iint u(\mathbf{r} - \mathbf{r}')a(\mathbf{r}')\mathrm{d}^2\mathbf{r}'$ denotes the convolution operation, $\mathbf{r}_n$ denotes the position of the n-th optical antenna ($n = 1, 2, ..., N$), $\delta(\mathbf{r})$ is the Dirac's delta function, and $C_n \equiv |C_n| \exp\left(\mathrm{i}\phi_n\right)$ is the complex amplitude of the light emitted from the n-th optical antenna (see Fig. 2.2 for a schematic to help your understanding). For convenience,

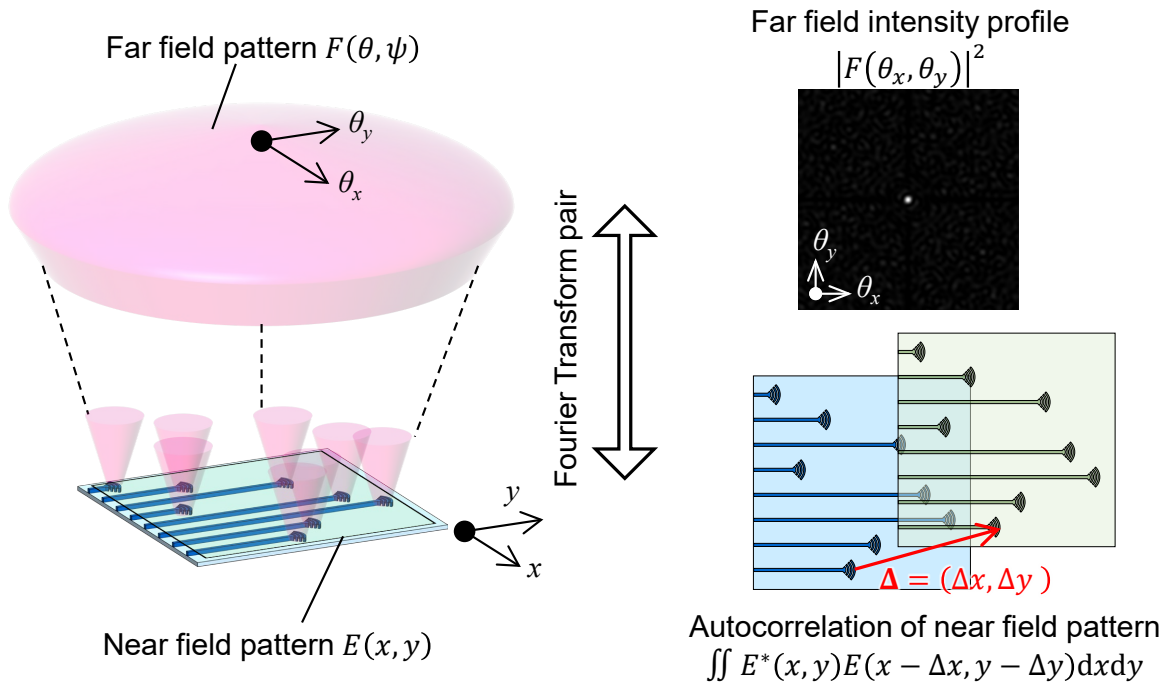

Fig. 2.1: The definition of variables and functions. The intensity distribution of the FFP is the Fourier transform of the autocorrelation function of the NFP.

we define the array layout function

$$a(\mathbf{r}) \equiv \sum_{n=1}^{N} C_n \delta(\mathbf{r} - \mathbf{r}_n) \tag{2.2}$$

to represent the entire array layout.

Since the FFP of the OPA is given as the Fourier transform of the NFP, $F(\mathbf{\Theta})$ is written as

$$F(\mathbf{\Theta}) = \iint E(\mathbf{r}) \exp\left(\mathrm{i}\beta_0 \mathbf{r} \cdot \mathbf{\Theta}\right) \mathrm{d}^2\mathbf{r}, \tag{2.3}$$

where β_0 is the wavenumber of light in the vacuum[*1]. By inserting Eq. (2.1) to Eq. (2.3) (see Fig. 2.3 to help your understanding), we obtain

$$F(\mathbf{\Theta}) = U(\mathbf{\Theta})A(\mathbf{\Theta}) = U(\mathbf{\Theta}) \sum_{n=1}^{N} C_n \exp\left[\mathrm{i}\beta_0 \left(\mathbf{r}_n \cdot \mathbf{\Theta}\right)\right]. \tag{2.4}$$

[*1] Actually, it is more accurate to use $(\sin\theta_x, \sin\theta_y)$ instead of $\mathbf{\Theta} = (\theta_x, \theta_y)$. However, in this chapter, we treat as $\theta \simeq \sin\theta$ for the sake of simplicity.

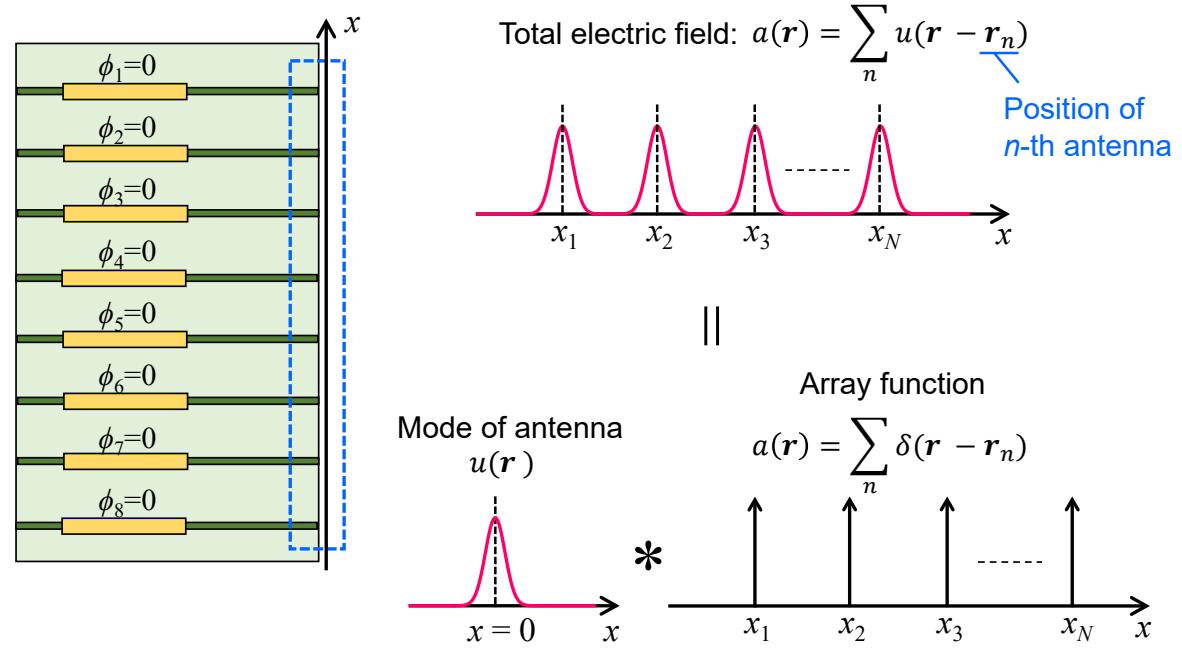

Fig. 2.2: A schematic diagram describing how the NFP of the OPA can be described. Here, for the sake of simplicity, $C_1 = C_2 = \ldots = C_N$ is assumed, which corresponds to the beam steering condition.

Here, $U(\boldsymbol{\Theta})$ is the Fourier transform of $u(\mathbf{r})$, i.e.,

$$U(\boldsymbol{\Theta}) \equiv \iint u(\mathbf{r}) \exp\left(\mathrm{i}\beta_0 \mathbf{r} \cdot \boldsymbol{\Theta}\right) \mathrm{d}^2\mathbf{r}, \tag{2.5}$$

describing the FFP of the electric field from a single optical antenna, and

$$A(\boldsymbol{\Theta}) \equiv \iint a(\mathbf{r}) \exp\left(\mathrm{i}\beta_0 \mathbf{r} \cdot \boldsymbol{\Theta}\right) \mathrm{d}^2\mathbf{r} = \sum_{n=1}^{N} C_n \exp\left[\mathrm{i}\beta_0 \left(\mathbf{r}_n \cdot \boldsymbol{\Theta}\right)\right] \tag{2.6}$$

is the Fourier transform of $a(\mathbf{r})$.

Finally, the intensity distribution of the FFP, which is important for imaging applications, can be expressed as (see Fig. 2.4 for the help of understanding)

$$I(\boldsymbol{\Theta}) = |F(\boldsymbol{\Theta})|^2 = |U(\boldsymbol{\Theta})|^2 \sum_{n=1}^{N} \sum_{m=1}^{N} C_n C_m^* \exp\left[\mathrm{i}\beta_0 \left(\mathbf{r}_n - \mathbf{r}_m\right) \cdot \boldsymbol{\Theta}\right]. \tag{2.7}$$

In Eq. 2.7, each term inside the summation $C_n C_m^* \exp\left[\mathrm{i}\beta_0 \left(\mathbf{r}_n - \mathbf{r}_m\right) \cdot \boldsymbol{\Theta}\right]$ physically represents the interference fringes generated by the lightwaves from the m-th and n-th optical antennas.

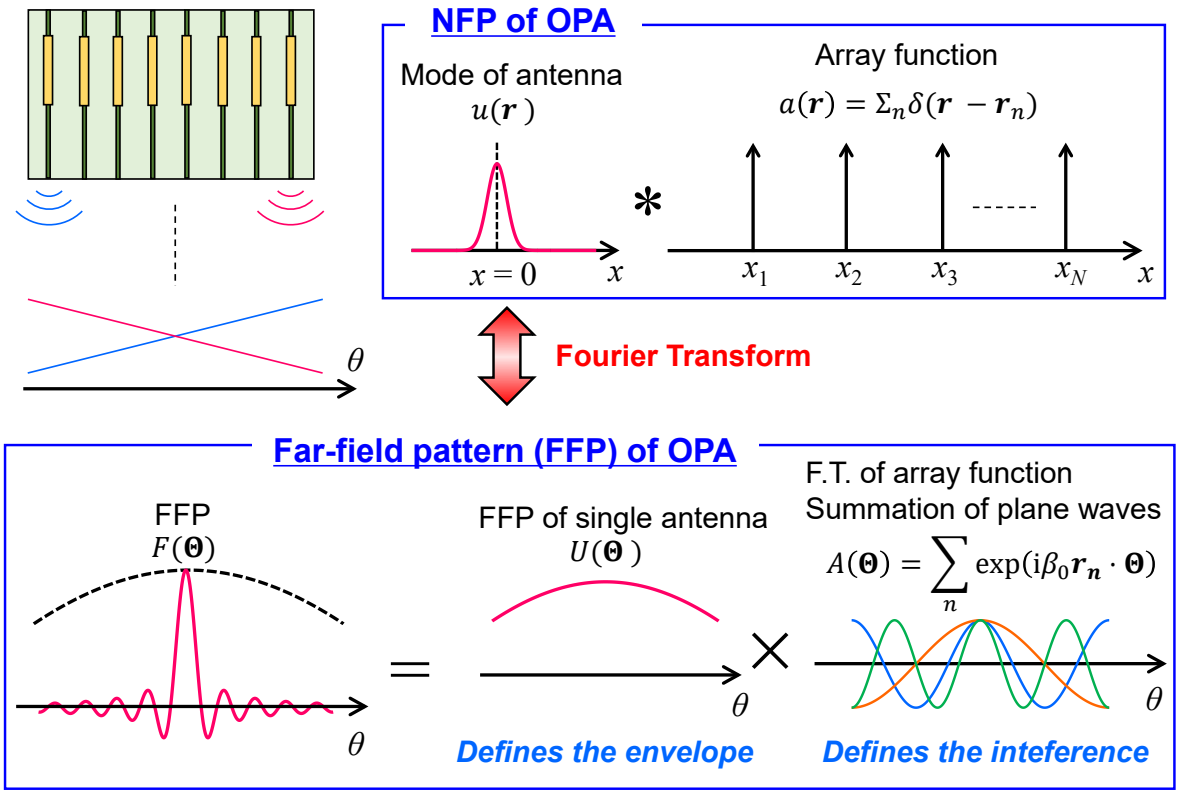

Fig. 2.3: A schematic diagram describing the relationship between the FFP and the NFP. Here, for the sake of simplicity, $C_1 = C_2 = ... = C_N$ is assumed, which corresponds to the beam steering condition.

When $\phi_1 = \phi_2 = ... = \phi_N$, a strong intensity peak is obtained at $\boldsymbol{\Theta} = (0, 0)$. This corresponds to the case of forming an equal phase plane at the emitter plane. The intensity peak can then be steered to an arbitrary angle $\boldsymbol{\Theta}_0 = (\theta_{x0}, \theta_{y0})$ within the FOV by tuning the optical phases ϕ_n so that the condition

$$\beta_0 (\mathbf{r}_n - \mathbf{r}_m) \cdot \boldsymbol{\Theta} + \phi_n - \phi_m = \beta_0 (\mathbf{r}_n - \mathbf{r}_m) \cdot (\boldsymbol{\Theta} - \boldsymbol{\Theta}_0) \tag{2.8}$$

is satisfied for all n and m $(= 1, 2, ..., N)$, which corespond to tilting the equal phase plane to the angle $\boldsymbol{\Theta}_0$. Equation 2.7 provides an important insight that the displacement vectors $\boldsymbol{\Delta}_{n,m} \equiv \mathbf{r}_n - \mathbf{r}_m$ between the optical antennas defines the spatial frequency spectrum of the FFP, and therefore, have a critical impact on determining the FFP. To investigate this aspect

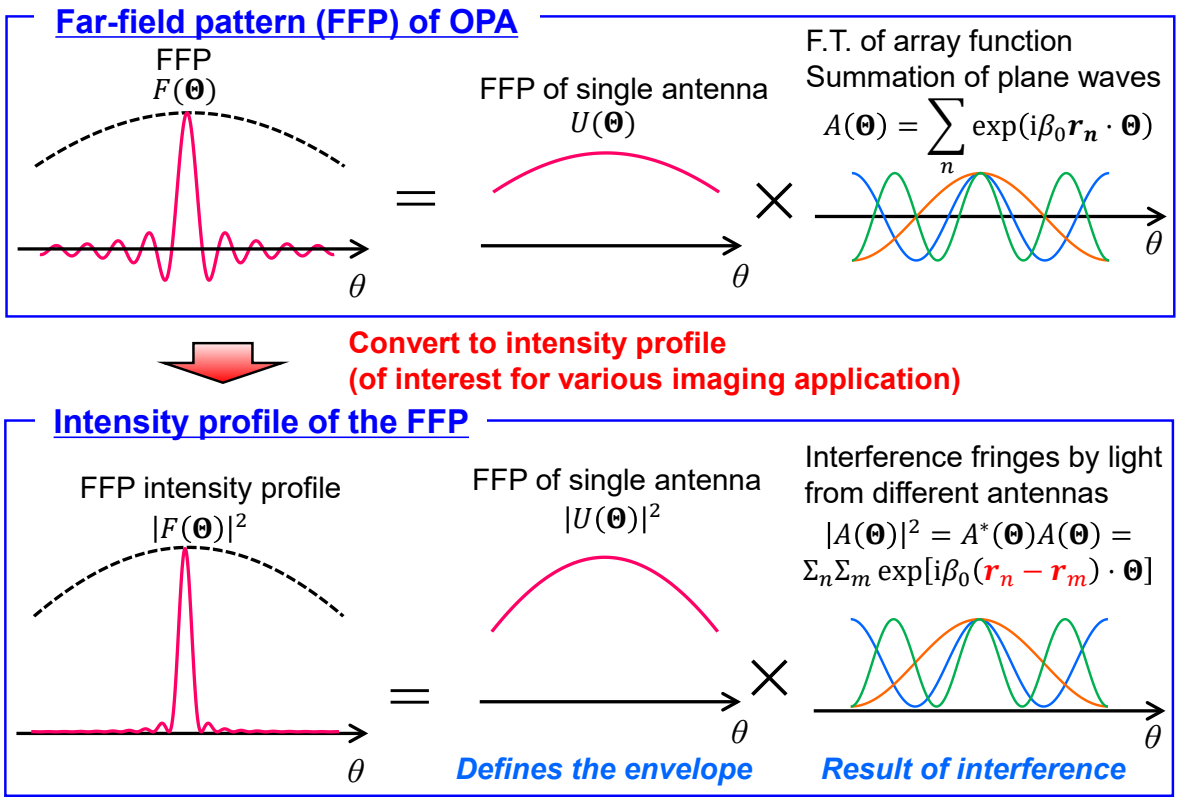

Fig. 2.4: A schematic diagram describing the relationship between the FFP and the intensity profile of the FFP. Here, for the sake of simplicity, $C_1 = C_2 = \ldots = C_N$ is assumed, which corresponds to the beam steering condition.

quantitatively, we now derive a different expression of $I(\boldsymbol{\Theta})$. From Eq. 2.3,

$$\begin{aligned} I(\boldsymbol{\Theta}) = |F(\boldsymbol{\Theta})|^2 &= \iiiint E(\mathbf{r})E^*(\mathbf{r}') \exp\left[\mathrm{i}\beta_0 (\mathbf{r} - \mathbf{r}') \cdot \boldsymbol{\Theta}\right] \mathrm{d}^2\mathbf{r}\mathrm{d}^2\mathbf{r}' \\ &= \iiiint E(\mathbf{r}' + \boldsymbol{\Delta})E^*(\mathbf{r}') \exp\left(\mathrm{i}\beta_0 \boldsymbol{\Delta} \cdot \boldsymbol{\Theta}\right) \mathrm{d}^2\boldsymbol{\Delta}\mathrm{d}^2\mathbf{r}' \\ &= \iint \mathscr{R}_{EE} \exp\left(\mathrm{i}\beta_0 \boldsymbol{\Delta} \cdot \boldsymbol{\Theta}\right) \mathrm{d}^2\boldsymbol{\Delta} \end{aligned} \tag{2.9}$$

where $\boldsymbol{\Delta} \equiv \mathbf{r} - \mathbf{r}'$. We define $\mathscr{R}_{EE}(\boldsymbol{\Delta})$ as

$$\mathscr{R}_{EE}(\boldsymbol{\Delta}) \equiv \iint E(\mathbf{r} + \boldsymbol{\Delta})E^*(\mathbf{r}) \exp\left(\mathrm{i}\beta_0 \boldsymbol{\Delta} \cdot \boldsymbol{\Theta}\right) \mathrm{d}^2\mathbf{r}, \tag{2.10}$$

which denotes the autocorrelation function of $E(\mathbf{r})$ in the spatial domain. Equation 2.9 implies that $I(\boldsymbol{\Theta})$ is the Fourier transform of $\mathscr{R}_{EE}(\boldsymbol{\Delta})$, which is reasonable from the Wiener-Khinchin theorem (see Fig. 2.5 for help in understanding). To obtain ideal $I(\boldsymbol{\Theta})$ with a fine and sharp

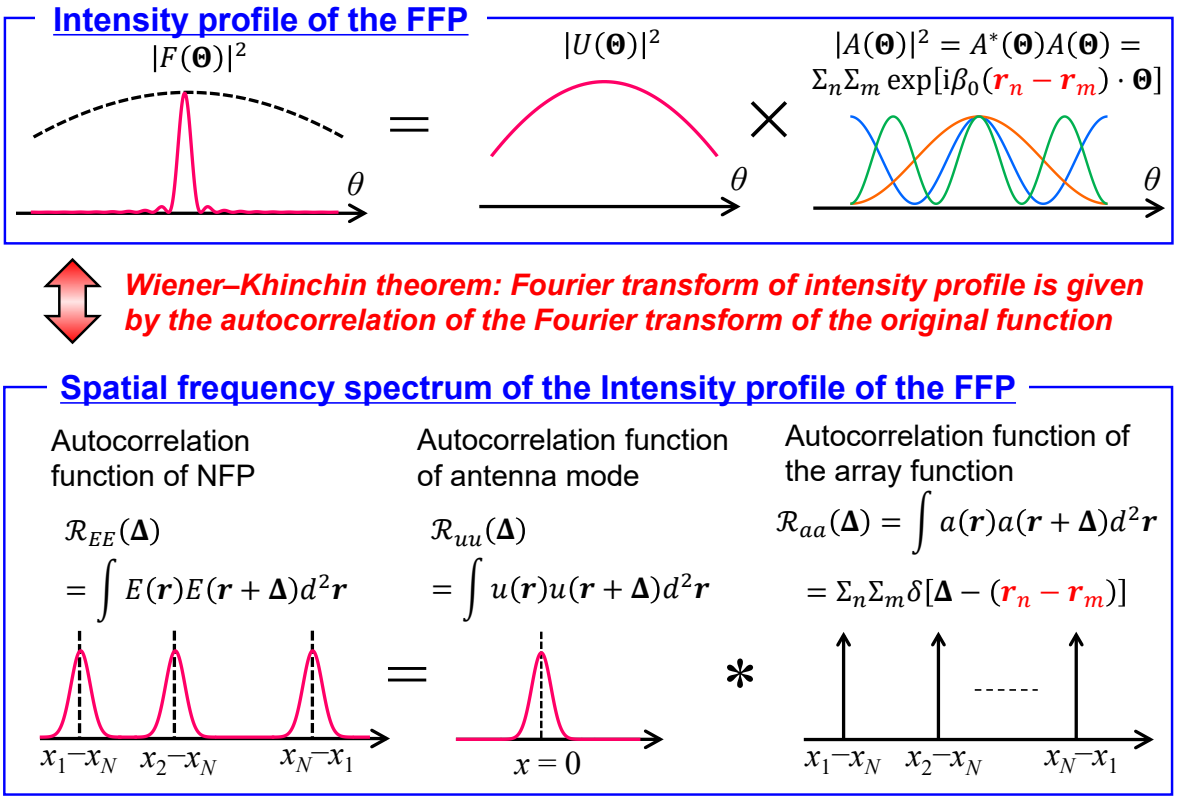

Fig. 2.5: A schematic diagram describing the relationship between the intensity profile of the FFP $I(\boldsymbol{\Theta})$ and the autocorrelation function $R_{EE}(\boldsymbol{\Delta})$. Here, for the sake of simplicity, $C_1 = C_2 = \ldots = C_N$ is assumed, which corresponds to the beam steering condition.

beam profile, therefore, it is essential to obtain as flat and broad $\mathscr{R}_{EE}(\boldsymbol{\Delta})$ as possible.

By substituting Eq. (2.1) to Eq. (2.10), we obtain

$$\begin{aligned}\mathscr{R}_{EE}(\boldsymbol{\Delta}) &= \sum_{n=1}^{N}\sum_{m=1}^{N} C_n C_m^* \iint u\left(\mathbf{r}+\boldsymbol{\Delta}-\mathbf{r}_n\right) u\left(\mathbf{r}-\mathbf{r}_m\right) \mathrm{d}^2\mathbf{r} \\ &= \sum_{n=1}^{N}\sum_{m=1}^{N} C_n C_m^* \mathscr{R}_{uu}\left(\boldsymbol{\Delta}-\boldsymbol{\Delta}_{n,m}\right) \\ &= \mathscr{R}_{uu}\left(\boldsymbol{\Delta}\right) * \sum_{n=1}^{N}\sum_{m=1}^{N} C_n C_m^* \delta\left(\boldsymbol{\Delta}-\boldsymbol{\Delta}_{n,m}\right) \\ &= \mathscr{R}_{uu}(\boldsymbol{\Delta}) * \mathscr{R}_{aa}(\boldsymbol{\Delta}).\end{aligned} \tag{2.11}$$

Here, we define

$$\mathscr{R}_{uu}(\boldsymbol{\Delta}) \equiv \iint u(\mathbf{r}+\boldsymbol{\Delta})u^*(\mathbf{r}) \exp\left(\mathrm{i}\beta_0\boldsymbol{\Delta}\cdot\boldsymbol{\Theta}\right) \mathrm{d}^2\mathbf{r} \tag{2.12}$$

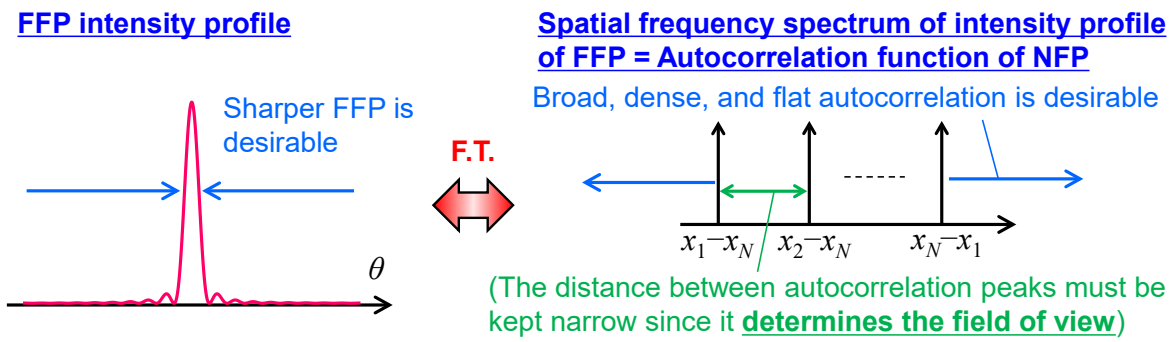

Fig. 2.6: A schematic diagram describing the requirements for realizing a sharp and fine FFP profile.

and

$$\mathscr{R}_{aa}(\mathbf{\Delta}) \equiv \iint a(\mathbf{r}+\mathbf{\Delta})a^*(\mathbf{r}) \exp\left(\mathrm{i}\beta_0 \mathbf{\Delta}\cdot\mathbf{\Theta}\right) \mathrm{d}^2\mathbf{r} = \sum_{n=1}^{N}\sum_{m=1}^{N} C_n C_m^* \delta\left(\mathbf{\Delta}-\mathbf{\Delta}_{n,m}\right), \tag{2.13}$$

which are the autocorrelation function of the electric field distribution from each antenna and the array layout function, respectively.

From Eq. (2.9) and Eq. (2.11), we can conclude that the spatial Fourier transform of the FFP from an OPA is represented by $\mathscr{R}_{EE}(\mathbf{\Delta})$, which is expressed as the convolution of $\mathscr{R}_{uu}(\mathbf{\Delta})$ and $\mathscr{R}_{aa}(\mathbf{\Delta})$ From Eq. (2.12), however, $\mathscr{R}_{uu}(\mathbf{\Delta})$ quickly drops to zero when $\mathbf{\Delta}$ exceeds to the physical size of the antenna. As a result, the bandwidth of $\mathscr{R}_{EE}(\mathbf{\Delta})$, or in other words, the maximal spatial frequency component of the FFP, is determined purely by $\mathscr{R}_{aa}$[*2]. Therefore, a broad and flat $\mathrm{R}_{EE}(\mathbf{\Delta})$ is obtained if we could engineer the array layout to spread $\mathscr{R}_{aa}(\mathbf{\Delta})$ as broad as possible (Fig. 2.6). We should note that it is not effective to increase the unit spacing between the antennas; although it will allow for a sharper beam, the field of view (FOV), which is inversely proportional to the unit spacing of the array, will become narrower simultaneously. From the definition of $\mathscr{R}_{aa}(\mathbf{\Delta})$ in Eq. (2.13), such a condition is realized when every $\mathbf{\Delta}_{n,m}$ are mutually different. In other words, all the interference patterns represented by $C_n C_m^* \left|U(\mathbf{\Theta})\right|^2 \exp\left(\mathrm{i}\beta_0 \mathbf{\Delta}_{n,m}\cdot\mathbf{\Theta}\right)$ have different spatial frequencies. At the same time, $\mathbf{\Delta}_{n,m}$ should be distributed as uniformly as possible so that the beam shape would not degrade.

Therefore, we will focus on $\mathscr{R}_{aa}(\mathbf{\Delta})$ to clarify the impact of the array layout on the FFP. For simpliciy, we also assume $C_1 = C_2 = \ldots = C_N = 1$, which corresponds to the case of beam

[*2] Indeed, $\mathscr{R}_{uu}(\mathbf{\Delta})$corresponds to the term $|U(\mathbf{\Theta})|^2$ of Eq. (2.7), and thus it only influences the envelope function of the FFP.

steering to $\boldsymbol{\Theta}_0 = (0, 0)$[*3]. Under such a condition, $\mathscr{R}_{aa}(\boldsymbol{\Delta})$ reduces to

$$\mathscr{R}_{aa}(\boldsymbol{\Delta}) = \sum_{n=1}^{N}\sum_{m=1}^{N} \delta\left(\boldsymbol{\Delta} - \boldsymbol{\Delta}_{n,m}\right) \tag{2.14}$$

2. Concept of non-redundant optical phased array

From the theoretical discussion in the previous section, we have found that an array whose $\boldsymbol{\Delta}_{n,m}$ are mutually different and distribute uniformly is desirable to be used to define the antenna location so that $\mathscr{R}_{aa}(\boldsymbol{\Delta})$ will be broad and flat. The non-redundant array (NRA) is a class of array that is defined to satisfy such condition.

1D NRA based on integers are called Golomb rulers [164]. A Golomb ruler with N elements can be defined as a set of integers G_n ($n = 1, 2, ..., N$) whose difference between every pair of elements are mutually distinct, i.e,

$$\delta_{\Delta G_{m,n},\Delta G_{m',n'}} = \delta_{m,m'}\delta_{n,n'} + \delta_{m,n}\delta_{m',n'}\left(1 - \delta_{m,m'}\delta_{n,n'}\right), \tag{2.15}$$

where $\Delta G_{m,n} \equiv G_m - G_n$ and $\delta_{m,n}$ is the Kronecker delta. Without loss of generality, we assume $0 = G_1 < G_2 < \cdots < G_N$ throughout this dissertation. By using such a Golomb ruler, we can measure ${}_N\mathrm{C}_2 = N(N-1)/2$ distinct lengths using a ruler with only N marks. A perfect Golomb ruler, a Golomb ruler which can sample all the integers within its length G_N, is an optimal mean to sample integers within a certain range without losing element. It is known that for $N \leq 4$, a perfect Golomb ruler exists (Table 2.1). However, for $N > 4$, it

Table 2.1: Perfect Golomb rulers

N	G_N
1	{0}
1	{0, 1}
1	{0, 1, 3}
4	{0, 1, 4, 6}

has been proven that a perfect Golomb ruler does not exist. Instead, a class of Golomb rulers called optimal Golomb rulers [165], which is the shortest Golomb ruler possible for a given N, exists (Table 2.2), exists. Finding the optimal Golomb ruler for a given N is thought to be an NP-hard problem and becomes exponentially challenging as N increases. Despite the

[*3] Note that once we discuss based on this condition, the same discussion holds for all beam steering conditions by satisfying Eq. (2.8).

Table 2.2: Optimal Golomb rulers. Note that there are several for N = 5, 6, 7, 10, and 11.

N	G_N
5	{0, 1, 4, 9, 11}
	{0, 2, 7, 8, 11}
6	{0, 1, 4, 10, 12, 17}
	{0, 1, 4, 10, 15, 17}
	{0, 1, 8, 11, 13, 17}
	{0, 1, 8, 12, 14, 17}
7	{0, 1, 4, 10, 18, 23, 25}
	{0, 1, 7, 11, 20, 23, 25}
	{0, 1, 11, 16, 19, 23, 25}
	{0, 2, 3, 10, 16, 21, 25}
	{0, 2, 7, 13, 21, 22, 25}
8	{0, 1, 4, 9, 15, 22, 32, 34}
9	{0, 1, 5, 12, 25, 27, 35, 41, 44}
10	{0, 1, 6, 10, 23, 26, 34, 41, 53, 55}
11	{0, 1, 4, 13, 28, 33, 47, 54, 64, 70, 72}
	{0, 1, 9, 19, 24, 31, 52, 56, 58, 69, 72}
12	{0, 2, 6, 24, 29, 40, 43, 55, 68, 75, 76, 85}
13	{0, 2, 5, 25, 37, 43, 59, 70, 85, 89, 98, 99, 106}
14	{0, 4, 6, 20, 35, 52, 59, 77, 78, 86, 89, 99, 122, 127}
15	{0, 4, 20, 30, 57, 59, 62, 76, 100, 111, 123, 136, 144, 145, 151}
16	{0, 1, 4, 11, 26, 32, 56, 68, 76, 115, 117, 134, 150, 163, 168, 177}
17	{0, 5, 7, 17, 52, 56, 67, 80, 81, 100, 122, 138, 159, 165, 168, 191, 199}
18	{0, 2, 10, 22, 53, 56, 82, 83, 89, 98, 130, 148, 153, 167, 188, 192, 205, 216}
19	{0, 1, 6, 25, 32, 72, 100, 108, 120, 130, 153, 169, 187, 190, 204, 231, 233, 242, 246}
20	{0, 1, 8, 11, 68, 77, 94, 116, 121, 156, 158, 179, 194, 208, 212, 228, 240, 253, 259, 283}
21	{0, 2, 24, 56, 77, 82, 83, 95, 129, 144, 179, 186, 195, 255, 265, 285, 293, 296, 310, 329, 333}
22	{0, 1, 9, 14, 43, 70, 106, 122, 124, 128, 159, 179, 204, 223, 253, 263, 270, 291, 330, 341, 353, 356,}
23	{0, 3, 7, 17, 61, 66, 91, 99, 114, 159, 171, 199, 200, 226, 235, 246, 277, 316, 329, 348, 350, 366, 372}
24	{0, 9, 33, 37, 38, 97, 122, 129, 140, 142, 152, 191, 205, 208, 252, 278, 286, 326, 332, 353, 368, 384, 403, 425}
25	{0, 12, 29, 39, 72, 91, 146, 157, 160, 161, 166, 191, 207, 214, 258, 290, 316, 354, 372, 394, 396, 431, 459, 467, 480}
26	{0, 1, 33, 83, 104, 110, 124, 163, 185, 200, 203, 249, 251, 258, 314, 318, 343, 356, 386, 430, 440, 456, 464, 475, 487, 492}
27	{0, 3, 15, 41, 66, 95, 97, 106, 142, 152, 220, 221, 225, 242, 295, 330, 338, 354, 382, 388, 402, 415, 486, 504, 523, 546, 553}

massive effort paid to this problem, the optimal Golomb ruler is known only up to $N = 27$ to date [166–169]. Although it is NP-hard to find and prove that a Golomb ruler is optimal, there also has been massive work to find quasi-optimal Golomb rulers through heuristic algorisms, and it is still a hot field of research [170–176]. We also should note that by allowing some redundant elements, i.e., some duplication in the difference between pairs of elements, we can construct an array that can sample all the numbers within a certain range. Such an array is called the minimum redundancy array (MRA) [177], and it is empirically known that we can construct an MRA without changing the scaling rule, i.e., the number of the distinct distances between pairs of elements can be large as $O(N^2)$.

For the 2D case, the discussion becomes relatively complicated since the configuration of the array is not so obvious in contrast to the case of a 1D array. However, the basic definition is the same as that of the 1D case; it is a set of lattice points with N element, where the displacement vectors between any pair of elements are mutually distinct. The Costas array is one of the well-known examples of 2D NRA [178–180]. A N-element Costas array is defined as a set of N lattice points $\mathbf{\Gamma}_n \equiv (\gamma_{1,n}, \gamma_{2,n})$ $(n = 1, 2, ..., N)$ of a square lattice, which satisfies:

1. All elements are within a $N \times N$ lattice.
2. Only 1 element exists for each row, i.e., $\gamma_{1,n}$ contains all the integers $1, 2, ..., N$ and is a permutation of it.
3. Only 1 element exists for each column, i.e., $\gamma_{2,n}$ contains all the integers $1, 2, ..., N$ and is a permutation of it.
4. All $N(N-1)/2$ displacement vectors between each pair of elements are distinct.

It is not as difficult to construct a Costas array compared to the optimal Golomb ruler, and a Costas array to a large N has been found [181–183]. This is because the condition of the Costas array is not as strict. As a consequence, the Costas array configuration is not as optimal, i.e., the displacement vectors are not as densely (or uniformly) distributing. We should note that for the 2D case, the array does not necessarily have to be a square lattice; for example, it can be a hexagonal lattice [184, 185]. The optimal choice of lattice structure is, in fact, not obvious.

The use of NRA has been exploited in vast field. For example, Babcock, who found the concept of the Golomb ruler independently from Golomb, conceived the concept of 1D NRA for channel frequency selection of radio frequency communication so as to suppress the intermodulation interference between channels [164]. The Costas array was proposed in a relatively similar context of suppressing the crosstalk induced by beat signals, in particular for the sound navigation and ranging (SONAR) system. Another common field of research that has explored the use of NRAs is the direction of arrival (DOA) problem [186–189]. DOA is a problem where N antennas are used to sense the wavefront at the receiver end, and

the signals obtained from the antennas are used to estimate from which direction the signal arrived through signal processing. Such a signal could either be acoustic waves or radio frequency signals. DOA based on NRA or MRA, where higher resolution can be obtained with a minimal number of antennas, are highly desirable for applications where the cost of antennas is non-negligible. The field of radio astronomy, where the very-long-baseline interferometry technique is commonly employed, is a typical example of a situation where the cost of antennas is critical since each antenna has to be an enormous parabolic antenna [177]. The baseline interferometry technique has also been implemented in the optical domain using a SiN integrated photonics platform [190]. Another optical imaging technique, which utilized tiles of small-scale OPAs located based on NRA in order to sample the information in the spatial and temporal frequency domain by emitting light with different frequency from each tile of OPA, have also been proposed and demonstrated [85].

In this work, for the first time, we use the concept of NRA to *define the location of the antennas of a single OPA*, as depicted in Fig. 2.7, and define such a new class of OPA called *non-redundant optical phased array (NROPA)*. In contrast to most of the previous work using NRAs and MRAs, where an array of antennas were used to sample the wavefront emitted from the scene in order to specify the location of the sources through signal processing, in this work, the antennas that emit the wave are located based on the NRA in order to synthesize a specific wavefront by simultaneous contribution from all the N antennas.

First, we discuss a 1D OPA, where the optical antennas are located along the x axis (with constant y). As an example case, Fig. 2.8 compares the $a(\mathbf{r})$ of a 1D uniform array [Fig. 2.8(a)] ($N = 14$) with a 1D optima Golomb ruler [Fig. 2.8(b)] ($N = 14$). Both arrays are drawn with the same dimensionless unit length (i.e., minimal spacing) of 1 along the x direction. In Figs. 2.8(c) and (d), we compare the autocorrelation function $\mathscr{R}_{aa}(\mathbf{\Delta})$ for both cases. As shown in Fig. 2.8, in case of the uniform array, due to the redundancy (i.e., the duplication of $\mathbf{\Delta}_{n,m}$), $\mathscr{R}_{aa}(\mathbf{\Delta})$ exhibits a narrow triangular shape with the width of $\Delta x = 26 = 2N - 1$. In contrast, we see in Fig. 2.8(d) that the $\mathscr{R}_{aa}(\mathbf{\Delta})$ of the optimal Golomb ruler is distributed uniformly over a large range of $\Delta x = 254 (\simeq N^2)$. Here, the sharp spike at $\Delta x = 0$ corresponds to the inevitable zero-frequency component, which originates from the term

$$\sum_{n=1}^{N} \delta(\mathbf{\Delta} - \mathbf{\Delta}_{n,n}) = \sum_{n=1}^{N} \delta(\mathbf{\Delta}) = N\delta(\mathbf{\Delta}) \tag{2.16}$$

in Eq. (2.14).

Since the maximum number of mutually different $\mathbf{\Delta}_{n,m}$ in Eq. (2.14) is ${}_2N\mathrm{C}_2 + 1 = N^2 - N + 1$, which corresponds to the number of cases for choosing two from N elements while distinguishing their order (corresponding to the positive and negative spatial frequency) and

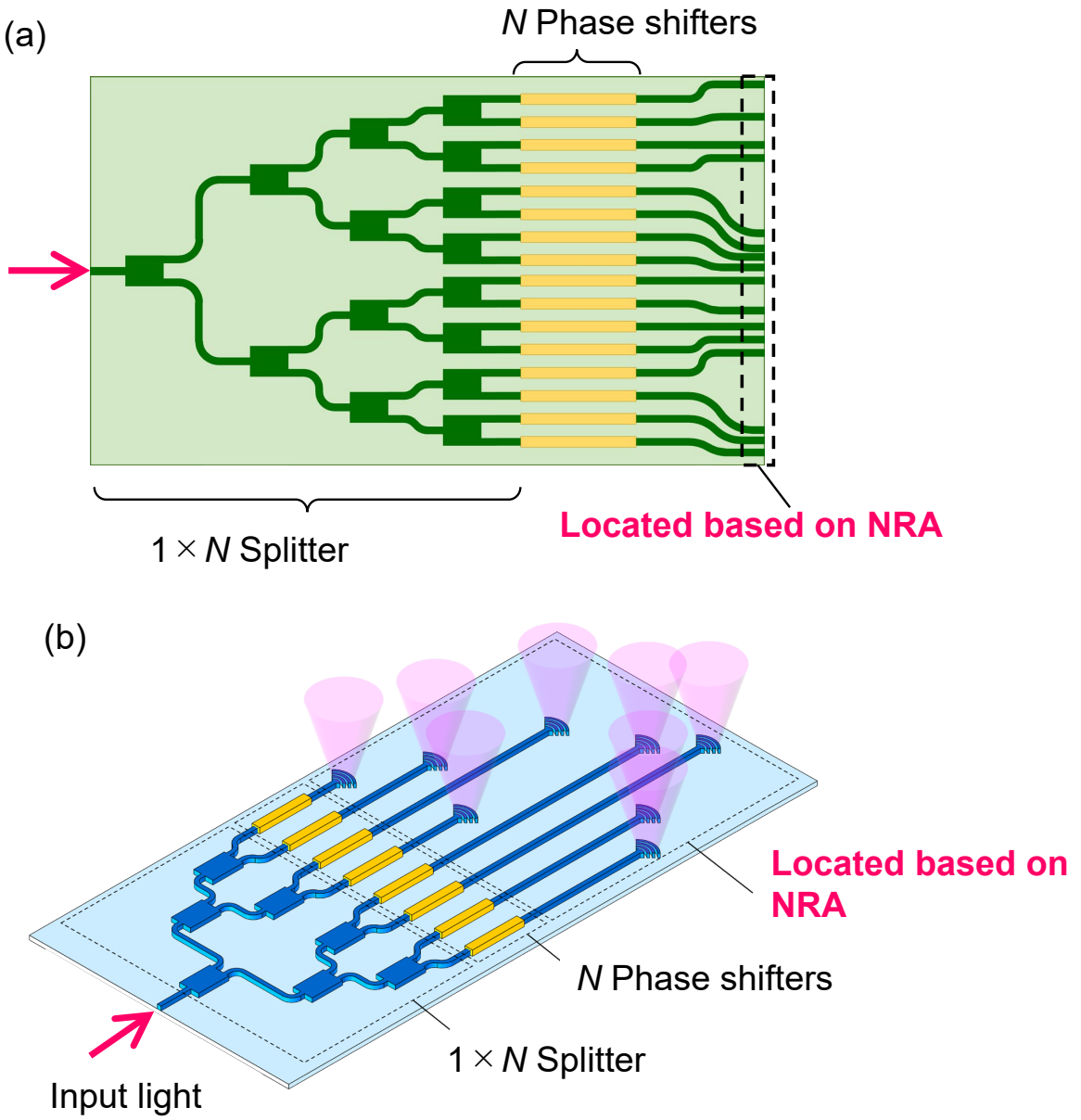

Fig. 2.7: Schematic of (a) 1D NROPA and (b) 2D NROPA. The optical antennas are located based on the NROPA.

an additional 1 for the zero-frequency component, $\mathscr{R}_{aa}(\mathbf{\Delta})$ can be broad as $N^2 - N + 1$ with a uniform density. However, at $N > 4$, $\mathscr{R}_{aa}(\mathbf{\Delta})$ distribute more broadly (i.e., its width will exceed $N^2 - N + 1$) with some missing peaks within its spectrum, corresponding to the fact that a perfect Golomb ruler does not exist[*4]. These missing peaks in $\mathscr{R}_{aa}(\mathbf{\Delta})$ could induce some penalty in the beam quality. Since the beam width should scale inversely proportional

[*4] However, we should note a perfect Golomb ruler is proved not to exist only when we focus our discussion on integers. If we extend our discussion to the whole real number including irrational numbers, there is a possibility that an array whose $\mathscr{R}_{aa}(\mathbf{\Delta})$ distributes almost perfectly uniform exists.

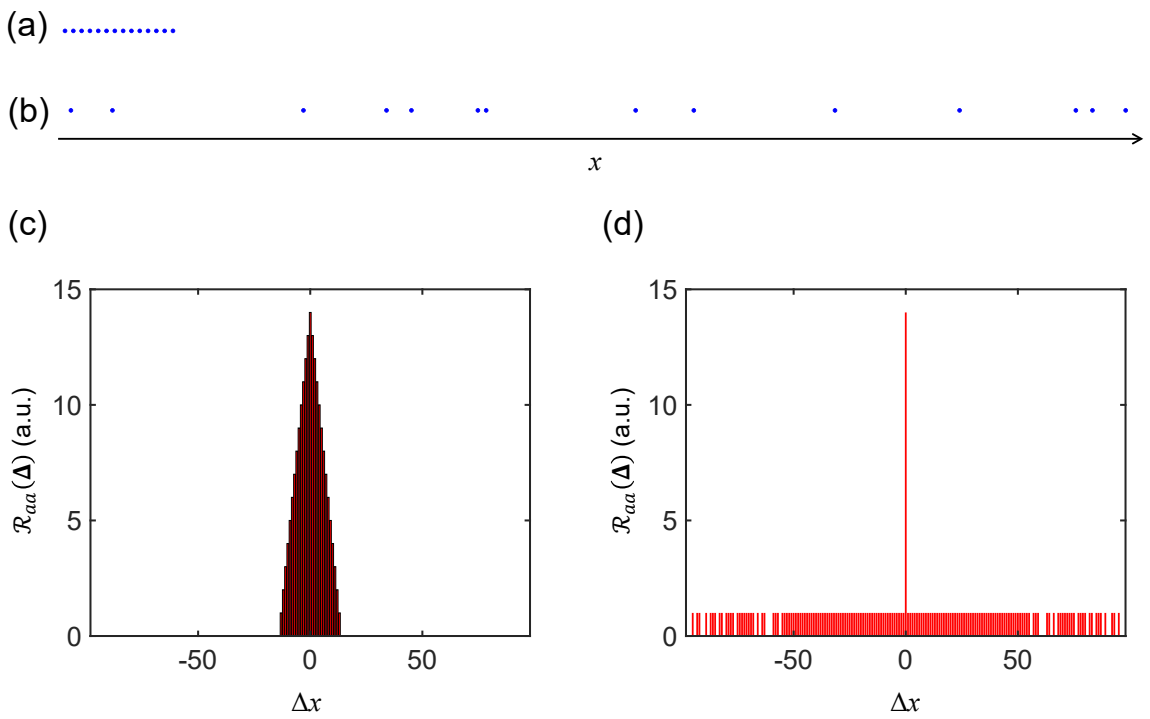

Fig. 2.8: Comparison of a 1D uniform array and a 1D NRA ($N = 14$). (a) $a(\mathbf{r})$ of a 1D uniform array. (b) $a(\mathbf{r})$ of a 1D NRA (Golomb ruler). (c) $\mathscr{R}_{aa}(\mathbf{\Delta})$ of a 1D uniform array. (d) $\mathscr{R}_{aa}(\mathbf{\Delta})$ of a 1D NRA.

to its spatial frequency bandwidth determined by $\mathscr{R}_{aa}(\mathbf{\Delta})$, whose width scales with N^2, and the field-of-view (FOV) determined by the minimum spacing between the antenna pairs d can be kept constant, the number of resolvable points determined by the ratio of the FOV and the full-width-at-half-maximum (FWHM) of the beam FOV/FWHM will scale with $O(N^2)$. This feature is in clear contrast with the case of uniformly spaced OPA (UOPA), where the number of resolvable points scales only by $O(N)$.

We then consider a 2D OPA. For a 2D NRA, we consider the use of Costas array as a representative example and for its compatibility with OPA due to its array structure. In Fig. 2.9, we compare a 2D uniform array ($\sqrt{N} \times \sqrt{N}, N = 36$) and a Costas array $N = 36$. In the case of the 2D uniform array, the antennas are densely located in a 6×6 uniform grid [Fig. 2.9(a)] In contrast, we can see in Fig. 2.9(b) that the antennas in the Costas array are located sparsely in a 36×36 uniform grid. Again, in the case of a uniform array, $\mathscr{R}_{aa}(\mathbf{\Delta})$ is narrow and pyramid-like-shaped as shown in Fig. 2.9(c), which fits within the range of $|\Delta x| \leq 5, |\Delta y| \leq 5$ [corresponding to a $\left(2\sqrt{N} - 2\right) \times \left(2\sqrt{N} - 2\right)$ grid]. On the other hand, Costas array has a broad and flat $\mathscr{R}_{aa}(\mathbf{\Delta})$, which distributes over a large range of $|\Delta x| \leq 35$ and $|\Delta y| \leq 35$ [corresponding to a $(2N - 2) \times (2N - 2)$ grid].

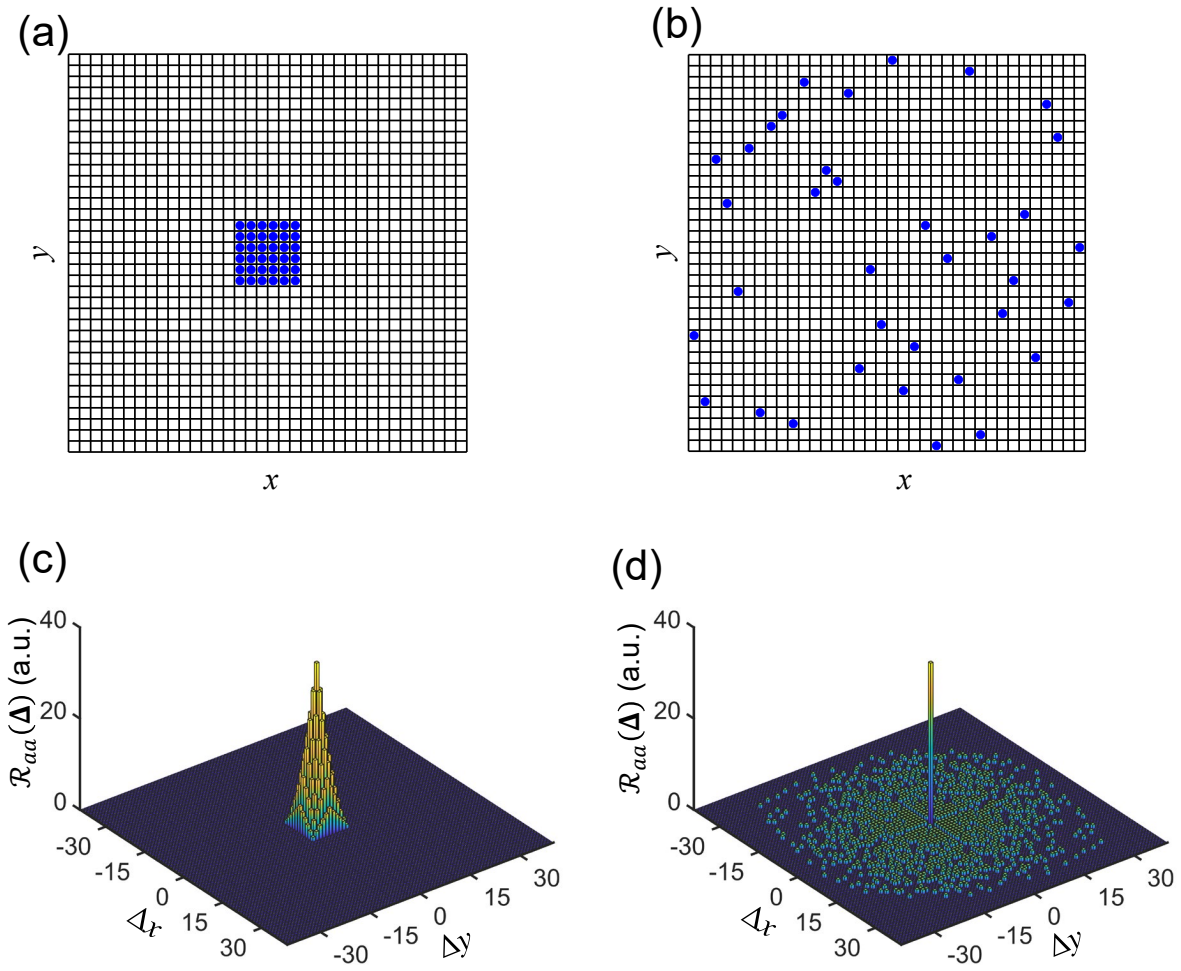

Fig. 2.9: Comparison of a 2D uniform array and a 2D NRA ($N = 14$). (a) $a(\mathbf{r})$ of a 2D uniform array. (b) $a(\mathbf{r})$ of a 2D NRA (Costas array). (c) $\mathscr{R}_{aa}(\mathbf{\Delta})$ of a 2D uniform array. (d) $\mathscr{R}_{aa}(\mathbf{\Delta})$ of a 2D NRA.

3. Numerical analysis

Next, we numerically derive the FFP of the OPA to directly investigate the impact of employing the NRA. In Fig. 2.10(a), we compare the FFPs of 1D OPAs with $N = 14$ based on the uniform array (blue) and the NRA (red) under a condition when all phase shifters are aligned. We can clearly observe that the FFP of the NRA-based OPA can be much narrower compared to that of the uniform OPA. Quantitatively, the number of the resolvable points (defined by FOV/FWHM) is derived to be 16 points ($\simeq N$) for the case of UOPA, while it is enhanced to 161 points ($\simeq N^2$) for the NROPA. Similarly, we show the FFPs of 2D OPAs based on the uniform array [Fig. 2.10(b)] and the Costas array [Fig. 2.10(c)] with $N = 36$. Again, we can see that a larger number of resolvable points [here, defined by the ratio of the area of the steering range and the FOV, i.e., (area of full FOV)/(area of FWHM), and the beam

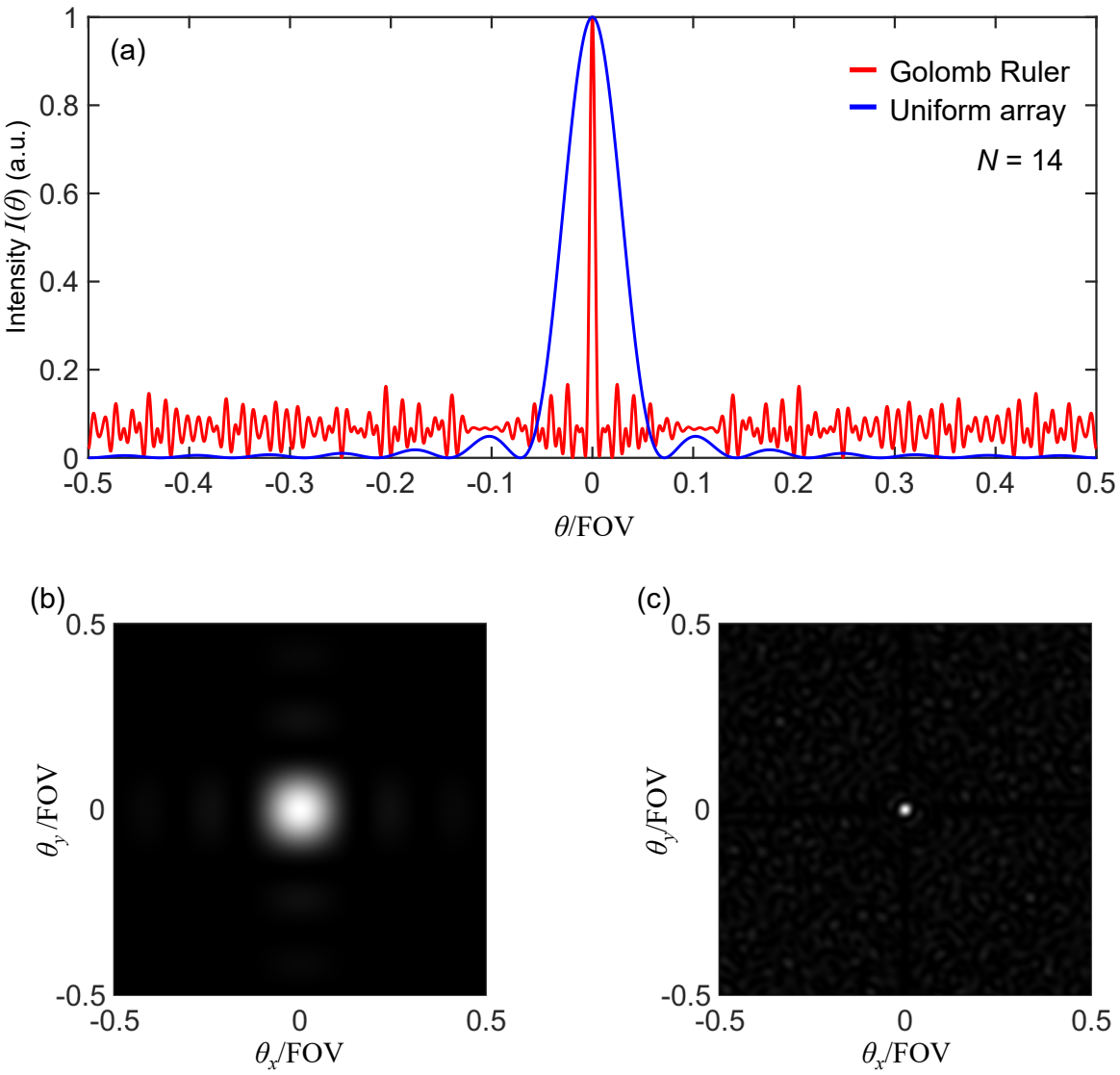

Fig. 2.10: Numerically derived FFPs of various OPAs: (a) 1D OPAs ($N = 14$) based on Golomb ruler (red) and uniform array (blue), (b) 2D UOPA ($N = 36$), and (c) 2D Costas-array-based OPA ($N = 36$).

size is derived as the area with the intensity stronger than the half of the peak intensity] can be obtained by employing the NROPA [2063 points ($\simeq N^2$)] compared to the UOPA [56 points ($\simeq N$)].

We then investigate the scalability of the NROPA compared with UOPA by systematically analyzing the N dependency of the FFP. Figure 2.11(a) shows how the number of resolvable points scales with N. While the number of resolvable points scales with $O(N)$ for the UOPAs (1D: blue, 2D: green, N is plotted together by black-dotted line as a reference), those of the NROPAs (Golomb ruler: red, Costas array: Pink) scale with $O(N^2)$ [N^2 is plotted together in the figure by black-broken line as a reference]. Figure 2.11(b) shows how the sidelobe

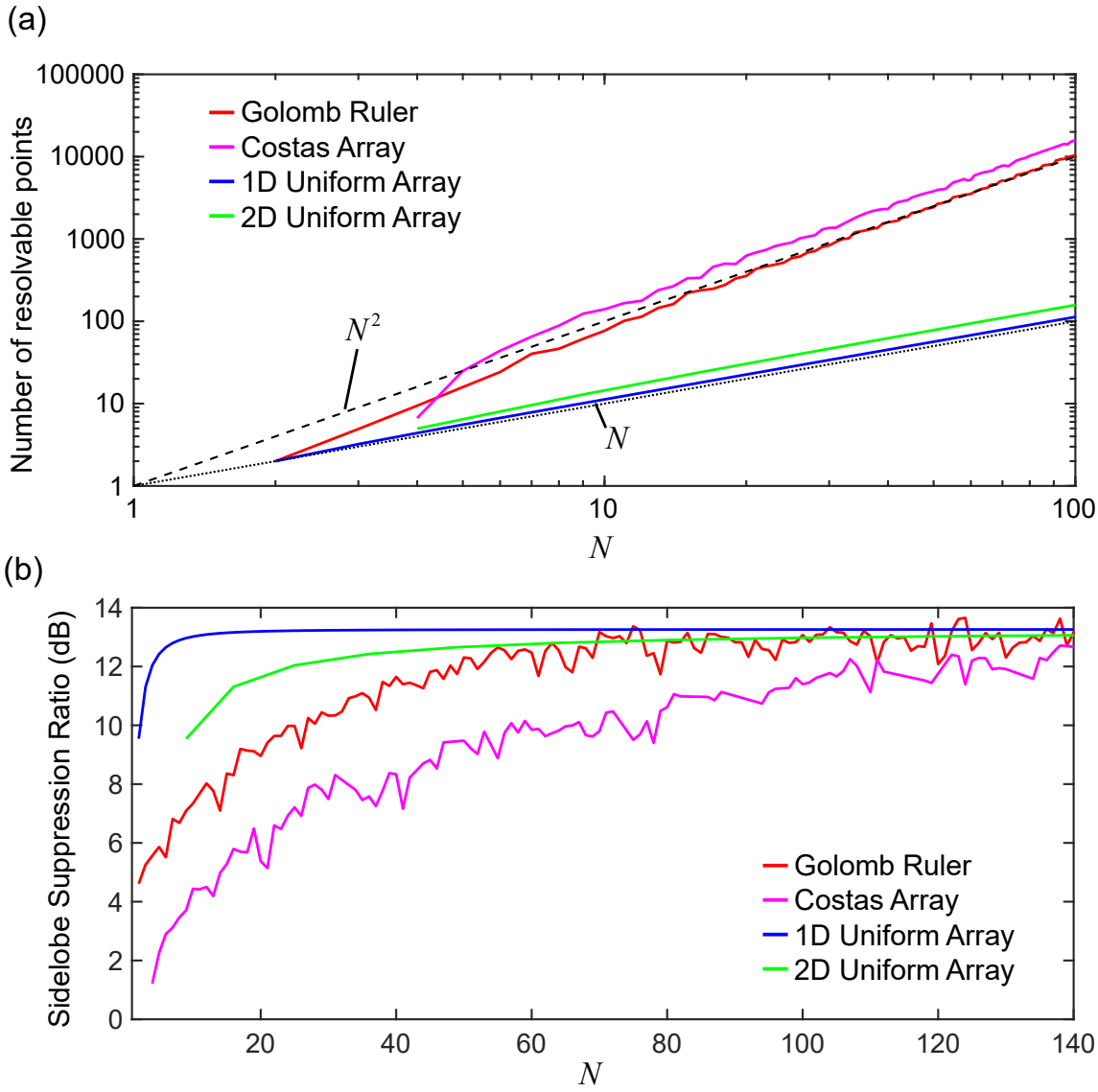

Fig. 2.11: Scalabilities of Golomb-ruler-based OPA (red), Costas-array-based OPA (pink), 1D UOPA (blue), and 2D UOPA (green). (a) N dependency of the number of resolvable points defined by FOV/FWHM. As a reference, N (black dotted) and N^2 (black broken) are also plotted. (b) N dependency of the sidelobe suppresion ratio.

suppression ratio varies with N. Although the sidelobe suppression is degraded for the NRA-based OPA at small N, it soon exceeds 10 dB and approaches that of UOPAs at moderate N of around 80[*5]. In contrast to the localized sidelobe of the UOPA induced by the sinc-function

[*5] We should note that this relatively poor sidelobe suppression ratio of the UOPA is induced by the rect-function-shaped envelope function of the NFP, i.e., the uniform power distribution among all the antennas. This will induce a relatively strong sidelobe corresponding to the second peak of the sinc-function, which is a Fourier transform pair of the rect-function. When the envelope function is Gaussian-like, for example (which could be realized by simply for example by using a star coupler [48]), the sidelobe suppression ratio can be significantly

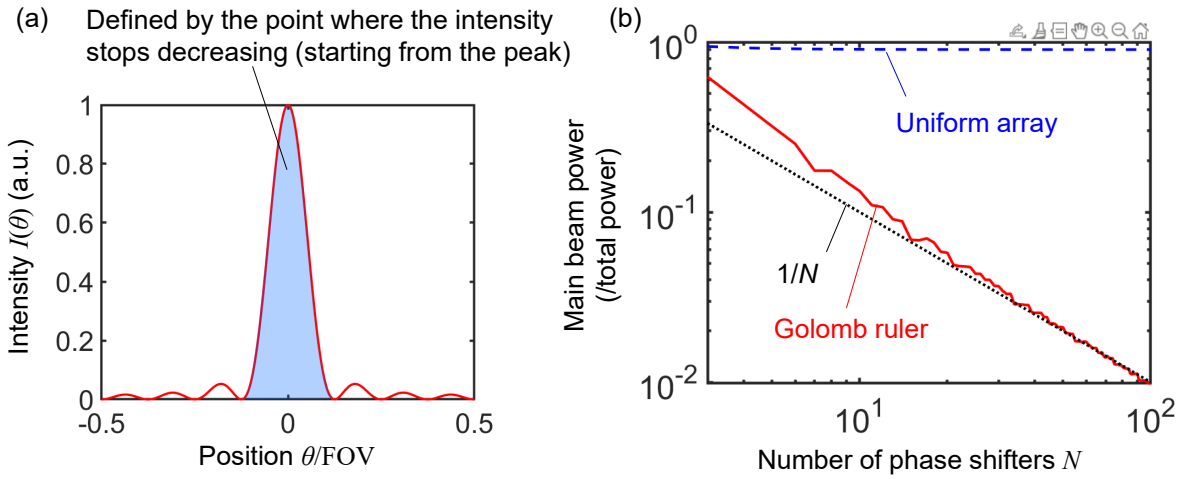

Fig. 2.12: (a) Definition of the power in the main lobe. (b) N dependency of the power in the main lobe.

beam shape, the sidelobe of the NROPA distributes widely over the entire FOV. This noise will indeed induce a power penalty, but since it is deterministic and not stochastic, it can be compensated for a situation with sufficient signal-to-noise-ration (SNR).

Finally, we discuss the power in the main beam of the FFP. For simplicity, here, we limit our discussion to the 1D case, but a similar discussion holds for the 2D case. The relative optical power in the main beam is defined as the portion of the optical power in the main beam (defined by the region starting from the peak of the beam and defined until the point where the optical intensity stops decreasing and starts to increase) with respect to the total optical power [see Fig. 2.12(a)]. Fig. 2.12(b) shows the N dependency of the optical power in the main beam. In the case of UOPA, the optical power is almost constant, and most of the optical power ($\simeq 90\%$) is within the main beam. In contrast, unfortunately, for the NROPA, the optical power in the main beam decreases with $1/N$. This could be understood through Fig. 2.13, which depicts $\mathscr{R}_{aa}(\mathbf{\Delta})$ [Fig. 2.13(a,c)] and $I(\mathbf{\Theta})$ [Fig. 2.13(b,d)] of a UOPA [$N = 12$, Fig. 2.13(a,c)] and an NROPA [$N = 12$, Fig. 2.13(b,d)], when the total optical power is normalized to 1 and the beam is steered to $\theta = 0$, i.e., $C_n = 1/\sqrt{N}$ ($N = 1, 2, ..., N$) (from which we can confirm that the total optical power $\sum_{n=1}^{N} |C_n|^2 = 1$ is correctly normalized). For the case of UOPA, $\mathscr{R}_{aa}(\mathbf{\Delta})$ is wide as $2N$, and therefore, the width of the main beam of $I(\theta)$ scales with $1/N$. Since the peak optical intensity can be derived from Eq. (2.4) and Eq. (2.7) as

$$I(0) = \left| \sum_{n=1}^{N} C_n \right|^2 = \left| N \cdot \frac{1}{\sqrt{N}} \right|^2 = N, \tag{2.17}$$

improved.

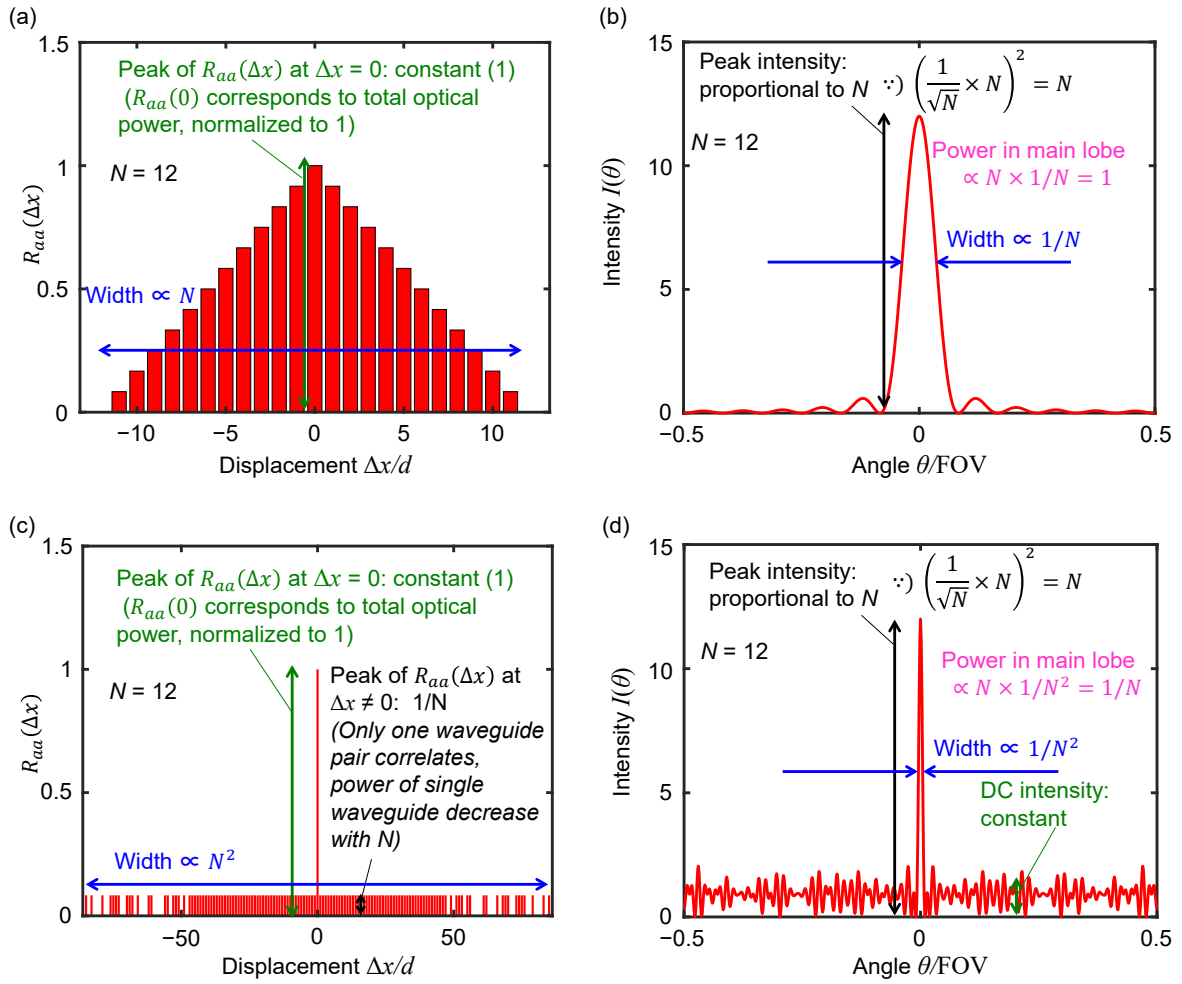

Fig. 2.13: Schematic diagram describing the origin of the scaling rule of the UOPA and NROPA (an example case of 1D OPA with $N = 12$ is depicted). (a,c) $\mathscr{R}(\mathbf{\Delta})$ of (a) UOPA and (c) NROPA. (b,d) $I(\mathbf{\Theta})$ of (b) UOPA and (d) NROPA.

the total power can be estimated as $N \times 1/N = 1$, meaning that the power in the main beam is constant regardless of N. In contrast, for the case of NROPA, $\mathscr{R}_{aa}(\mathbf{\Delta})$ is wide as N^2, and therefore, the width of the main beam of $I(\theta)$ scales with $1/N^2$. However, since Eq. (2.17) holds irrespective of the array configuration, the peak optical intensity remains the same, i.e., the peak intensity scales with N. As a result, the optical power in the main beam should scale with $N \times 1/N^2 = 1/N$. Therefore, we can conclude that NROPA is not suitable for power-sensitive applications. However, in cases where the optical power is not significantly important, NROPA could be a nice choice, as it could provide a drastic improvement in the scalability of the number of resolvable points. Moreover, for applications where the intensity is important, such as non-linear optics, NROPA could provide a high-resolution beam steering without sacrificing the peak intensity.

4. Summary

In this chapter, we have proposed the concept of the NROPA and numerical analysis to support the effectiveness of it. First we theoretically derived and studied $I(\theta)$ of an OPA in depth, and thorugh it, we have pointed out the importance of optimizing $\mathscr{R}_{aa}(\mathbf{\Delta})$ of the array layout. We then have introduced the NRA as a class of array that satisfies the requirement to optimize $\mathscr{R}_{aa}(\mathbf{\Delta})$. We have qualitatively and quantitatively discussed the scalability of NROPA and compared it with UOPA. The extraordinary scalability of the number of resolvable points is demonstrated. On the other hand, the drawback of the NROPA, i.e., the small optical power in the main beam, has been clarified.

2.A The impact of the mode field size of the antenna.

In order to clarify the impact of the mode field diamter of the optical antenna mode $u(\mathbf{r})$, we have calculated $I(\theta)$ and $\mathscr{R}_{EE}(\mathbf{\Delta})$ with various mode field size with respect to the unit spacing d of the array. For simplicity, here, we have assumed a 1D NROPA, and the antennas to have a Gaussian mode profile

$$u(x) = \exp\left(-\frac{x^2}{2w^2}\right), \tag{2.18}$$

where w denotes the width of the Gaussian profile. Note that in such a case, the envelope function $U(\mathbf{\Theta})$ defined by the antenna mode becomes

$$U(\theta_x) = \exp\left(-\frac{w^2\,(\beta_0\theta_x)^2}{2}\right) = \exp\left(-\frac{(w/d)^2\,(2\pi)^2\,(\theta_x/\theta_{\mathrm{FOV}})^2}{2}\right) \tag{2.19}$$

and the autocorrelation function $\mathscr{R}_{uu}(\theta)$ of the antenna mode becomes

$$\mathscr{R}(\Delta x) = \exp\left(-\frac{\Delta x^2}{w^2}\right). \tag{2.20}$$

In Fig. 2.14(a-d) and Fig. 2.14(e-g), we depict $I(\theta)$ and $\mathscr{R}_{EE}(\Delta x)$ of a 1D NROPA ($N = 14$) under various d/w, respectively. When $d/w \geq 10$ [Fig. 2.14(a,b,g,h)], the envelope function of the FFP is much larger than the FOV. As a result, the higher order diffractions are apparent, which corresponds to the peaks in $\mathscr{R}_{EE}(\Delta x)$ being close to a discrete peak isolated from each other. As d/w decreases, the envelope function of the FFP becomes narrower, and the spikes in $\mathscr{R}_{EE}(\Delta x)$ broaden and start to overlap with each other. When $3 \leq d/w \leq 5$ [Fig. 2.14(c,d,i,j)], the $\pm$1st order diffraction peaks are significantly smaller than the main peak, and

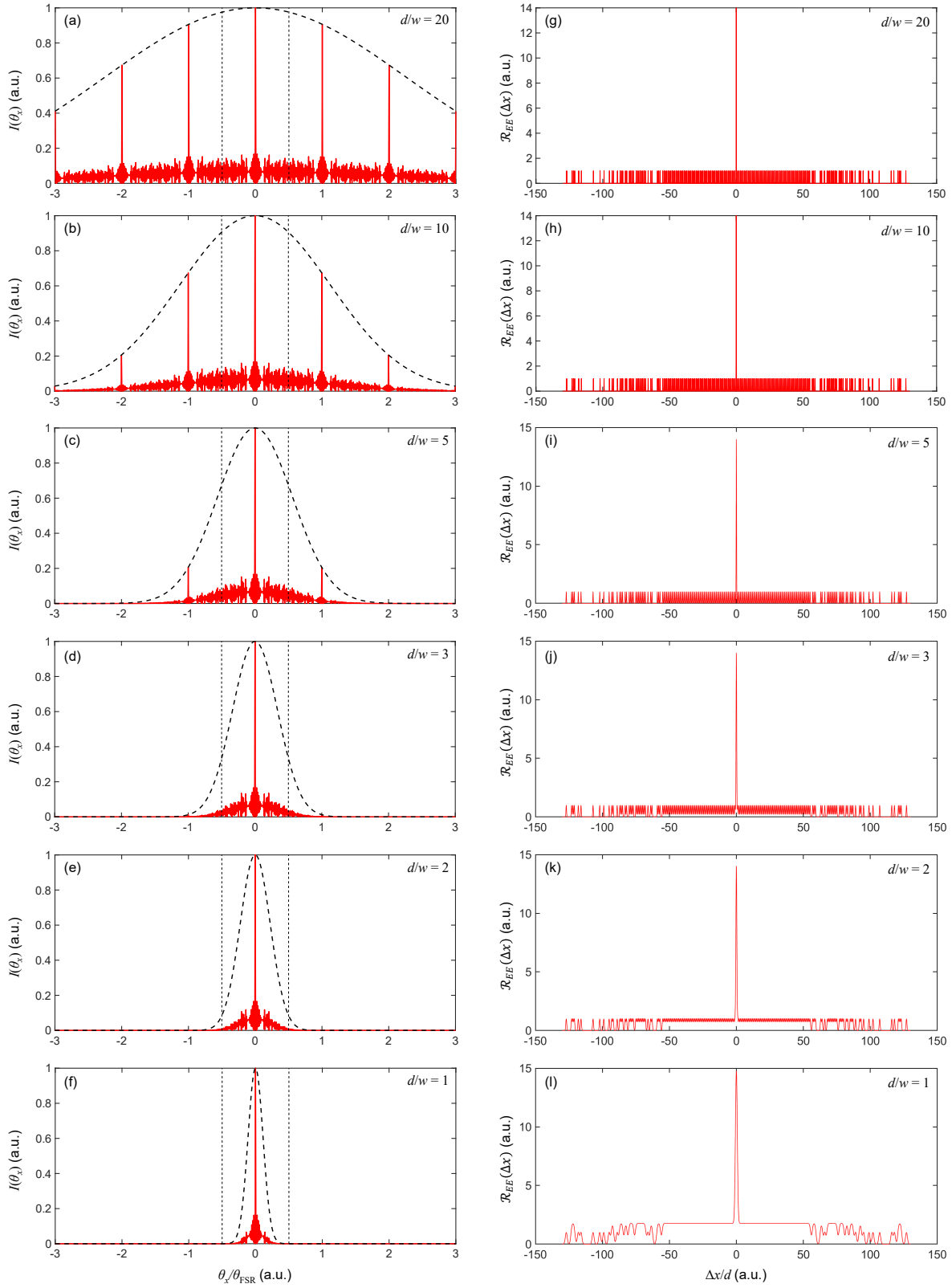

Fig. 2.14: The impact of mode field diameter w with respect to array unit spacing d on the FFP of the OPA (a-f) and the autocorrelation function of the NFP $\mathscr{R}_{EE}(\mathbf{\Lambda})$ (g-l). (a,g) $d/w = 20$. (b,h) $d/w = 10$. (c,i) $d/w = 5$. (d,j) $d/w = 3$. (e,k) $d/w = 2$. (f,l) $d/w = 1$.

when $d/w \leq 2$ [Fig. 2.14(e,f,k,l)], the diffraction peak disappears. We can see that $\mathscr{R}_{EE}(\Delta x)$, in this case, is continuous, corresponding to the disappearance of the periodicity in the FFP.

2.B Impact of antenna position error on the side lobe suppression ratio

Here, we discuss how the sidelobe suppression ratio of the beam changes when there is a fabrication-induced error in the antenna location[*6]. In Fig. 2.15, we show how the sidelobe suppression ratio changes when there is error δx_n in the position of the antennas x_n, for the case of 1D UOPA and 1D NROPA. We assume that δx_n follows a Gaussian distribution with a standard deviation of $\mathcal{S}(\delta x)$ and plot the mean value for 100 cases. We assume that $\phi_1 = \phi_2 = \cdots = \phi_N$, i.e., the phase shifters are optimized to steer the beam to $\theta_x = 0$ taking into account the fabrication error. We also assume that the optical power from each antenna is equal and that each antenna is a point light source. In order to derive the sidelobe suppression ratio, we discuss only within the range of the original FOV, although there is no longer any periodicity in the FOV after random fabrication variation. This is because it is difficult to distinguish the peak originating from diffraction peaks and pure sidelobes. We can see that UOPA is much more immune to antenna position error. Moreover, for UOPA, the tolerance to antenna position error improves as N increases. This tolerance possibly originates from the redundancy of the array. In UOPA, several pairs of antennas are responsible for the same spatial frequency component. Therefore, even if there is an antenna location error leading to the change in distance between pairs of antennas that directly leads to a deviation in the spatial frequency, such an effect would be averaged and suppressed. In contrast, NROPA is relatively sensitive to antenna location error since every spatial frequency component is generated from a single pair of antennas. Nevertheless, the fabrication accuracy of the antenna location is quite accurate if a stepper could be used (possibly at the range of ~10 nm). Since the unit spacing d of the array is never smaller than half the wavelength (775 nm for 1550 nm wavelength), we can see from Fig. 2.15 that such a small fabrication error of the antenna location is negligible.

2.C Comparison with other array configurations

Here, we discuss other configurations in terms of $\mathscr{R}_{EE}(\mathbf{\Delta})$ and $I(\mathbf{\Theta})$ for clarity.

In Fig. 2.16, we show $\mathscr{R}_{EE}(\Delta x)$ and $I(\theta_x)$ of 1D pseudorandom-array-based non-uniform OPA. Here, we assume that perturbation δx_n is applied to uniform antenna location x_n of 1D uniform OPA, and that all δx_n independently follow Gaussian distribution with a standard deviation of $\mathcal{S}(\delta x)$. We also assume that NFP of each antenna is a Gaussian function with width $w = d/20$ as in the previous section. We can see that when $\mathcal{S}(\delta x) > 0.2$, the

[*6] Note that the peak intensity is insensitive to the antenna location error.

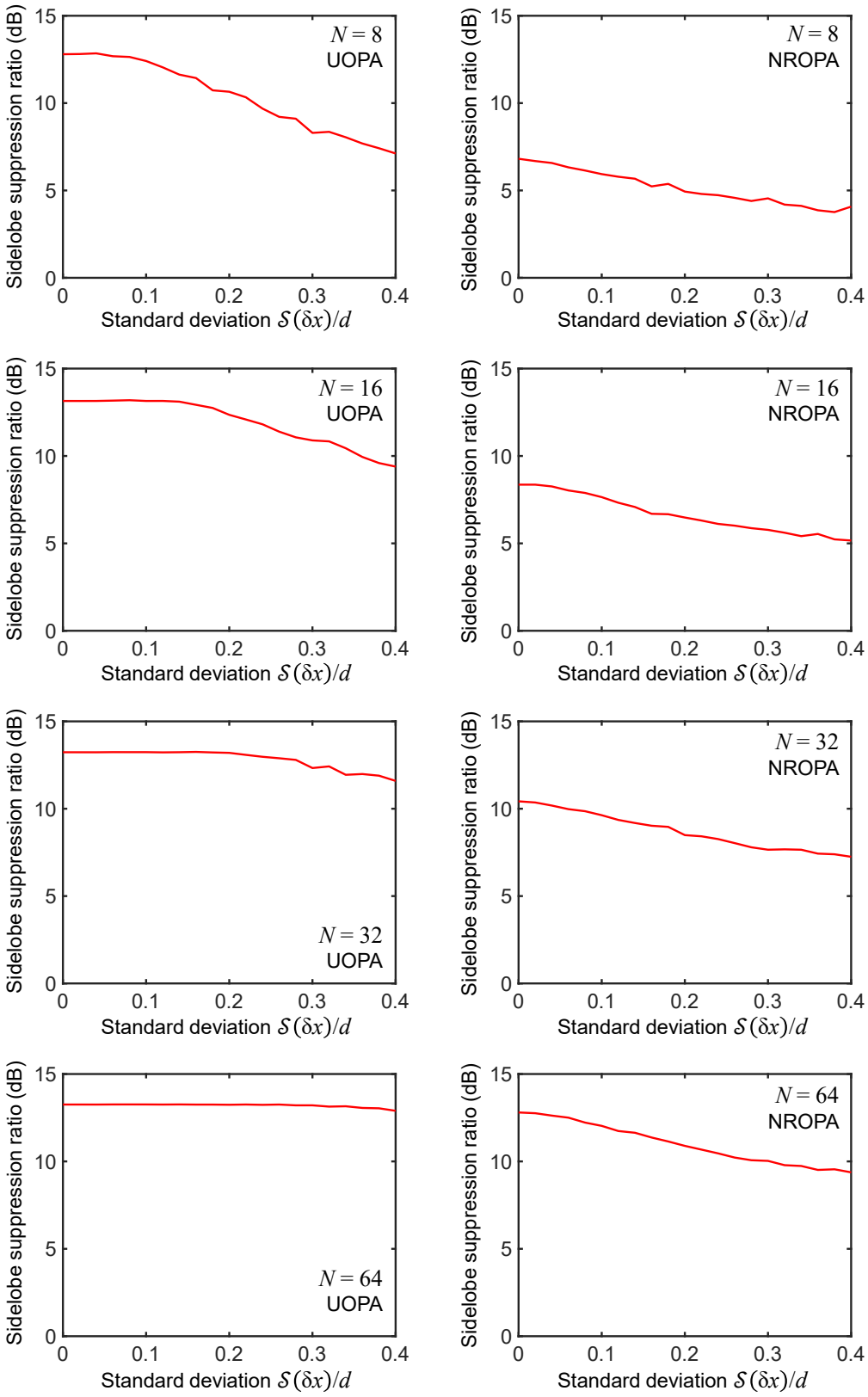

Fig. 2.15: The impact of antenna position error δx on the sidelobe suppression ratio (the impact of δx is normalized by the unit spacing d of the array).

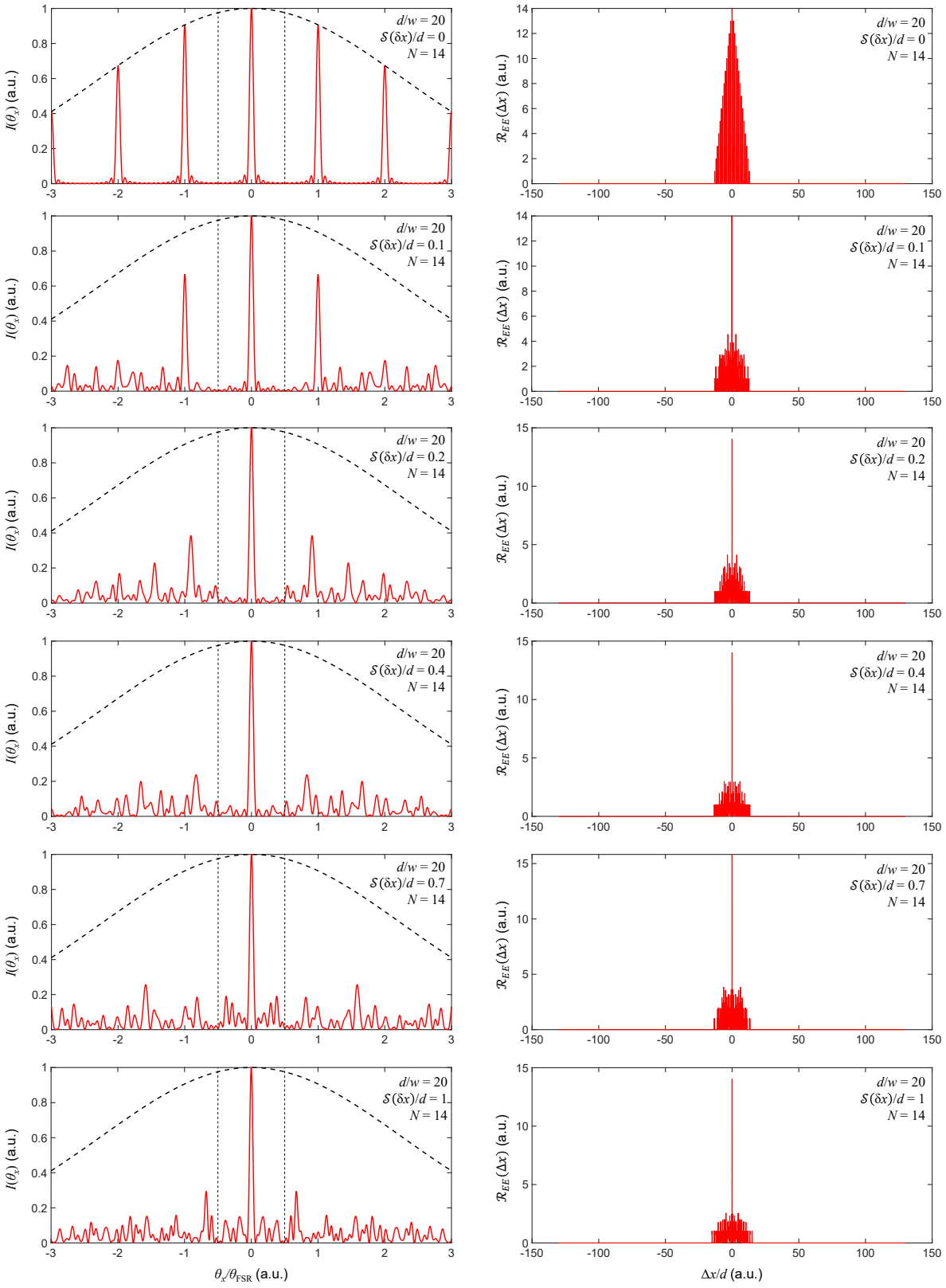

Fig. 2.16: $I(\theta_x)$ and $\mathcal{R}_{EE}(\Delta x)$ of a 1D pseudorandom-array-based non-uniform OPA under various $\mathcal{S}(\delta x)$.

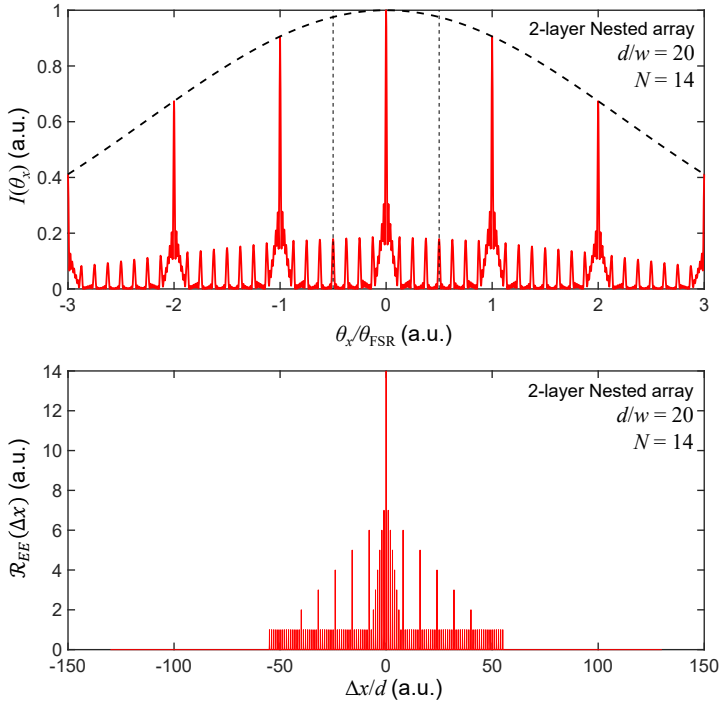

Fig. 2.17: $I(\theta_x)$ and $\mathcal{R}_{EE}(\Delta x)$ of a 1D 2-layer-nested-array-based non-uniform OPA under various $\mathcal{S}(\delta x)$.

periodicity-induced diffraction peak disappears and a wide steering angle can be obtained. On the otherhand, the width of the main beam is realtively insensitive to $\mathcal{S}(\delta x)$ as the average distance between antennas (and therefore the total aperture size) are kept almost the same. This disappearance of the periodicity can be seen from $\mathscr{R}_{EE}(\Delta x)$ as the disappearance of the discrete nature of $\mathscr{R}_{EE}(\Delta x)$. We should note that the sidelobe level is a little bit higher compared to the case of NROPA. This is because of the poor flatness of $\mathscr{R}_{EE}(\Delta x)$. Although this flatness can be improved by choosing the best case out of many test cases, such a design is not deterministic and is rather heuristic.

In Fig 2.17, we show $\mathscr{R}_{EE}(\Delta x)$ and $I(\theta_x)$ of 1D 2-layer-nested-array-based non-uniform OPA [186]. Here, 2-layer-nested array is a class of reduced redundancy array that could be realized deterministically by combinig two uniform arrays with different pitch. In this case, $x_n = d, 2d, ..., 7d, 8d, 16d, ..., 56d$. We can see that a sharp intensity peak (whose width scales with $O(N^2)$) is obtained, but at the same time, with a rather wide skirt (originating from the smaller-pitch uniform array) and periodic sidelobe (originating from the larger-pitch uniform array). This kind of array can be an alternative to NRA or MRA as it can be found easily and deterministically. It also is attractive for SSPI using NROPA (which we discuss later) as there is no missing spatial frequency component within the given range of array.

CHAPTER 3

EXPERIMENTAL DEMONSTRATION OF HIGH-RESOLUTION BEAM STEERING USING NON-REDUNDANT OPTICAL PHASED ARRAY

In Chapter 2, we have proposed and investigated the concept of NROPA. From theory and numerical analysis, we have shown that a large number of resolvable scaling with N^2 can be realized by locating the optical antennas based on the NRA concept. As a natural second step, we proceeded to the experimental demonstration of the concept. We designed and fabricated a silicon photonic OPA chip and experimentally demonstrated a 2D NROPA based on the Costas array. We built an experimental setup to evaluate the fabricated silicon OPA. We experimentally demonstrated ultra-high-resolution beam steering with 19,000 resolvable points, which is the largest number achieved for an OPA operating at a single wavelength. In this chapter, we describe the design and fabrication of the silicon photonic chip, the experiment setup, and the experiment results.

1. Design and fabrication of silicon OPA

First, we describe the design of silicon OPA. The silicon OPA ($N = 127$) was fabricated using the 200 mm silicon-on-insulator (SOI) multi-project wafer foundry service. The SOI wafer comprised a 220-nm-thick silicon layer and a 2 μm buried oxide layer. The optical microscope image of the device is shown in Fig. 3.2. The device is a 2D NROPA whose antennas are located based on a Costas array.

At the input of the OPA, a spot size converter (SSC) based on the 200-μm-long inversely-tapered waveguide, combined with the deep trenches, is employed to minimize the coupling loss from the input fiber to the silicon waveguides. At the tip of the SSC, the waveguide width is thinned down to 200 nm. The silicon waveguides were designed to be 400 nm wide so that they guide only the fundamental transverse-electric (TE) and transverse-magnetic (TM)

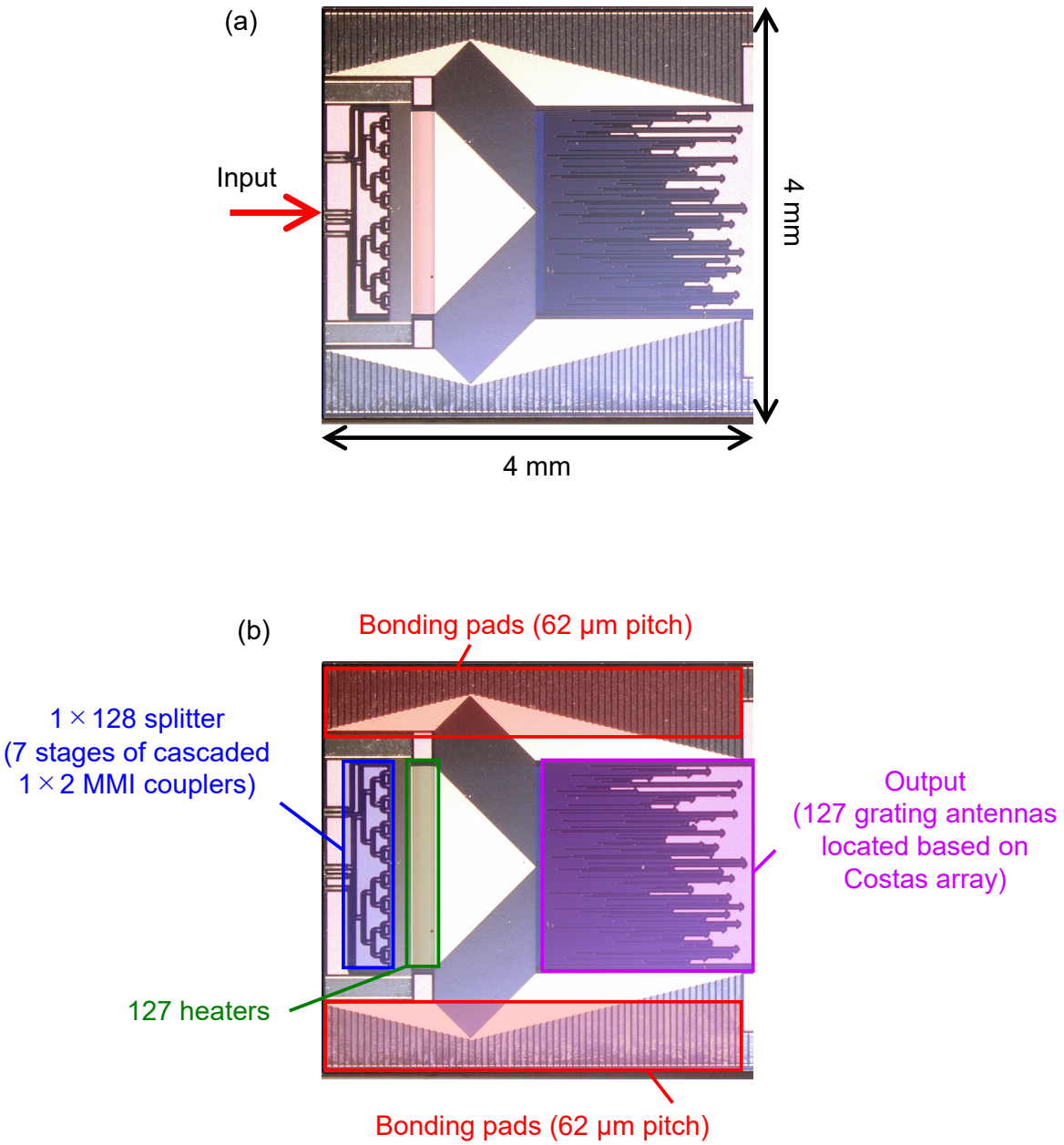

Fig. 3.1: Microscope image of the fabricated 2D OPA. (a) Overview of the chip. (b) Explanation of the location of each building blocks.

modes*1. The input light is then distributed to 128 waveguides via a 1 × 128 coupler, which

*1 I should note, however, that this design strategy to design the silicon photonic waveguides at single mode region is becoming out of date. By making the waveguides wider, up to the range of multi-micron, the silicon waveguides can become very low loss [191]. Generally speaking, the main cause of optical loss in silicon waveguides are due to the optical scattering induced by the sidewall roughness. By making the optical waveguides wider, most of the light will be confined in the silicon layer, and the portion of light that couples to radiative mode through perturabtion induced by the waveguide width deviation will be reduced. One of the reason that the waveguides were tend to be designed at the single-mode region is because there was a

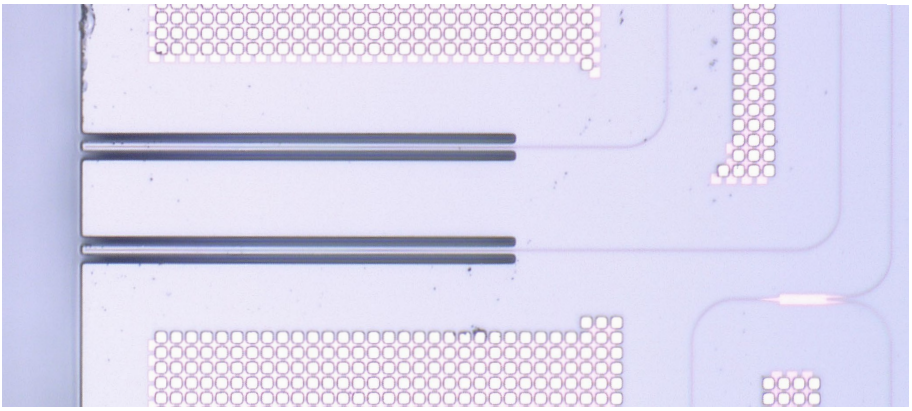

Fig. 3.2: Microscope photograph of the SSC.

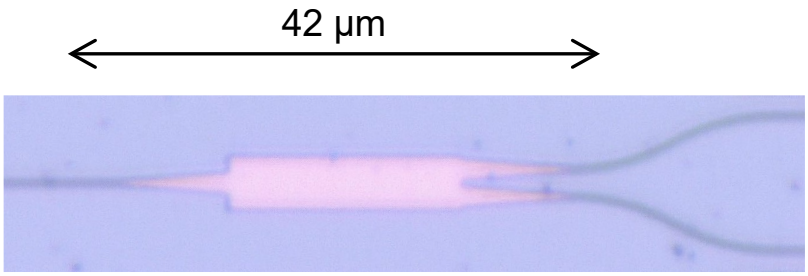

Fig. 3.3: Microscope photograph of the 1×2 MMI coupler.

we realized by employing 7 stages of cascaded 1×2 MMI couplers (Fig. 3.3). Here, one of the waveguides was used as an alignment port to monitor the fiber-to-chip coupling efficiency, emitting the light from the facet of the chip. The remaining 127 waveguides were used to emit the output light. Each of the 127 waveguides was equipped with a 220-μm-long TiN thermo-optic phase shifter (Fig. 3.4). The TiN layer was formed more than 1.2 μm above the silicon layer to minimize the optical loss. Deep trenches were formed in the vicinity of the TiN heaters (4 μm away from the heater) so as to minimize the thermal crosstalk and to

concern that the fundamental mode will couple to the higher-order mode through perturbation such as bending. However, it is recently becoming clear that by carefully designing the bending waveguides so that the mode transition is adiabatic, the coupling to higher mode through bending waveguides can be minimized even for a multi-micron wide waveguides supporting multiple transverse modes [133]. Moreover, it is also becoming clear that by designing the optical waveguides to be multi-micron wide, the deviation in refractive index can be minimized, and as a result, the accumulation of optical phase error can be minimized [134]. This reduction in optical phase error can be attributed to the fact that at multi-micron-wide waveguides, most of the light is confined in silicon and will not be effected by deviataion of the waveguide width; this mechanism is totally same with the reason of reduction in optical loss. On the other hand, for modulators and other active components, it is critical to make the electric field intensity per photon as large as possible to enhance the light-matter interactions. In such components, single mode waveguides can be highly useful since they maximize the electric field intensity and ensure very strong light-matter interaction.

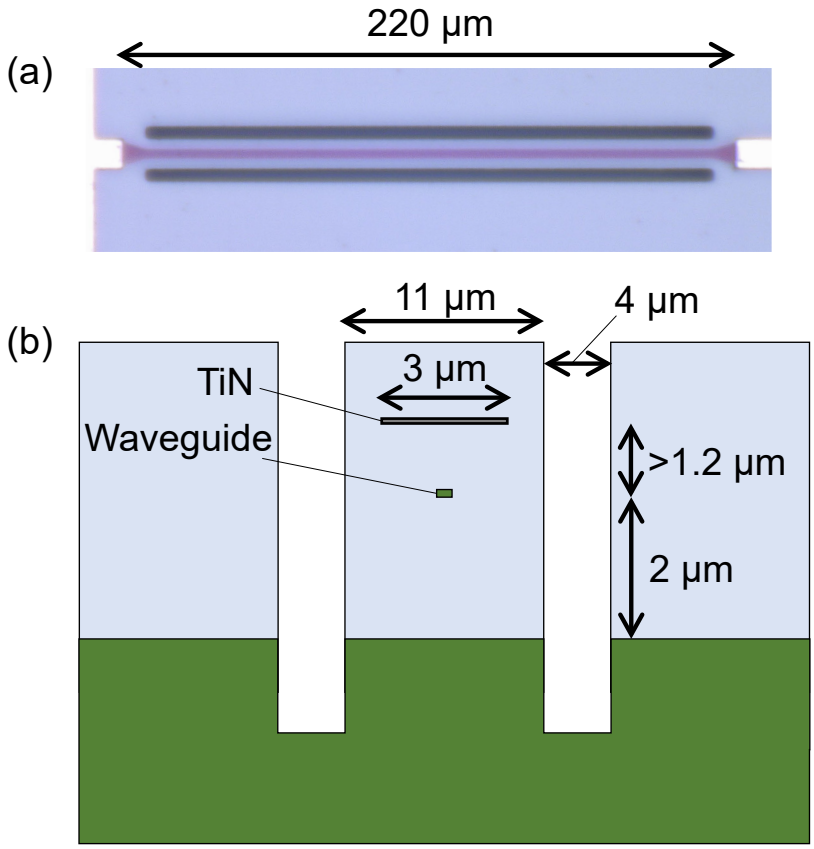

Fig. 3.4: (a) Microscope photograph of the thermo-optic phase shifter. (b) Cross-sectional schematic of the thermo-optic phase shifter.

maximize the efficiency of the phase shifters*[2]. The electrical power consumption of the phase shifters was 10 mW/π, which we evaluated using a Mach-Zehnder interferometer (MZI) test pattern (Fig. 3.5). The resistance of the TiN heaters was approximately 1 kΩ, with some small variation. After being phase controlled by the phase shifters, the light experiences a short delay line consisting of bent waveguides and a straight waveguide to minimize the optical path length difference between each waveguide so as to minimize the wavelength dependency of the output optical wavefront*[3]. Finally, the output light is emitted to free space via micron-scale

*[2] I should note that the design presented here is not optimal (due to the lack of experience as this was my first time to design a silicon photonic chip). According to the design rule, the isolation trenches could have been closer to the heater. Moreover, the isolation trenches does not cover the entire heater; it does not cover near the vias from the heater layer to the wiring layer. It is desirable to design so that the trenches perfectly thermally isolate the heaters from each other. Further isolation should be possible by separating the heaters by a larger distance, which could be easily enabled for example by a interleaved design.

*[3] Again, this design is not optimal. This design leads to unnecessarily longer waveguide. The longer waveguide will lead to larger optical loss and larger accumulated optical phase error. It is desirable to minimize the waveguide length while equalizing the optical path length. Here, however, we employed relatively long waveguides to equalize the optical path length, due to simplicity of the design. Nevertheless, the design presented here is sufficient to suppress the wavelength dependency of the output wavefront.

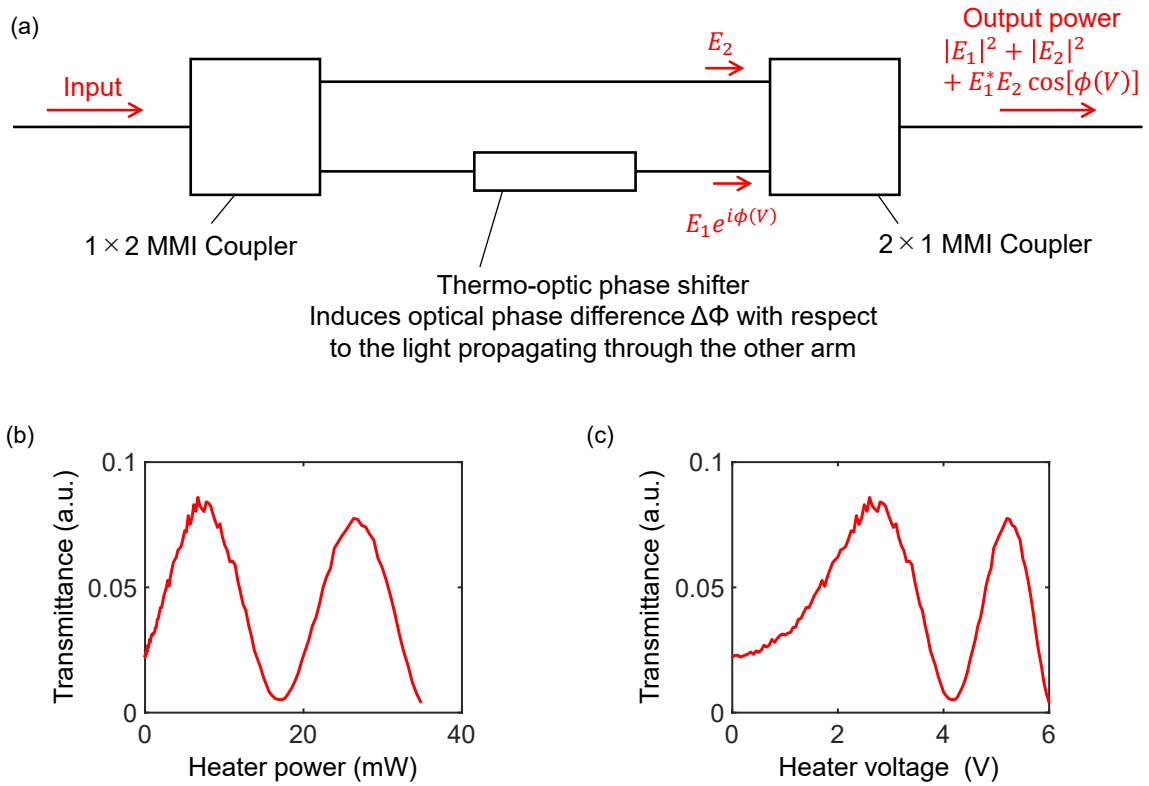

Fig. 3.5: (a) Schematic of the MZI for evaluating the efficiency of the themo-optic phase shifters. (b,c) The trasnmittance of the MZI while varying the electrical power applied to the heater (b) or the voltage applied to the heater (c).

grating-coupler-based optical antennas, which are located at the tip of each waveguide (Fig. 3.6). The radiation pattern from a single optical antenna simulated using finite-difference time-domain (FDTD) method is depicted in Fig. 3.7. The simulated FWHM of the FFP was 14° for θ_x direction and 18.4° for the θ_y direction. The antennas are located based on a Costas array ($N = 127$) with a unit grid length of $d = 15\,\mu\text{m}$. From this unit grid length, we can derive the FOV to be $5.92° \times 5.92°$ from the equation

$$\theta_{\text{FOV}} = \frac{\lambda}{d}. \tag{3.1}$$

The FOV is, therefore, within the simulated range of radiation from a single antenna.

The electrical wiring on the chip was realized by an Al layer. SiO_2 was used to embed and protect the waveguides, the heaters, and the wires, but it was removed at the bonding pads. The fabricated chip was mounted on an AlN chip carrier, which consists of Au wiring, using silver paste (Fig. 3.8). [*4] The OPA chip was wire-bonded using Au wires to the printed circuit

[*4] Here, AlN was chosen as the material for the chip carrier in order to ensure high thermal conductivity, so that

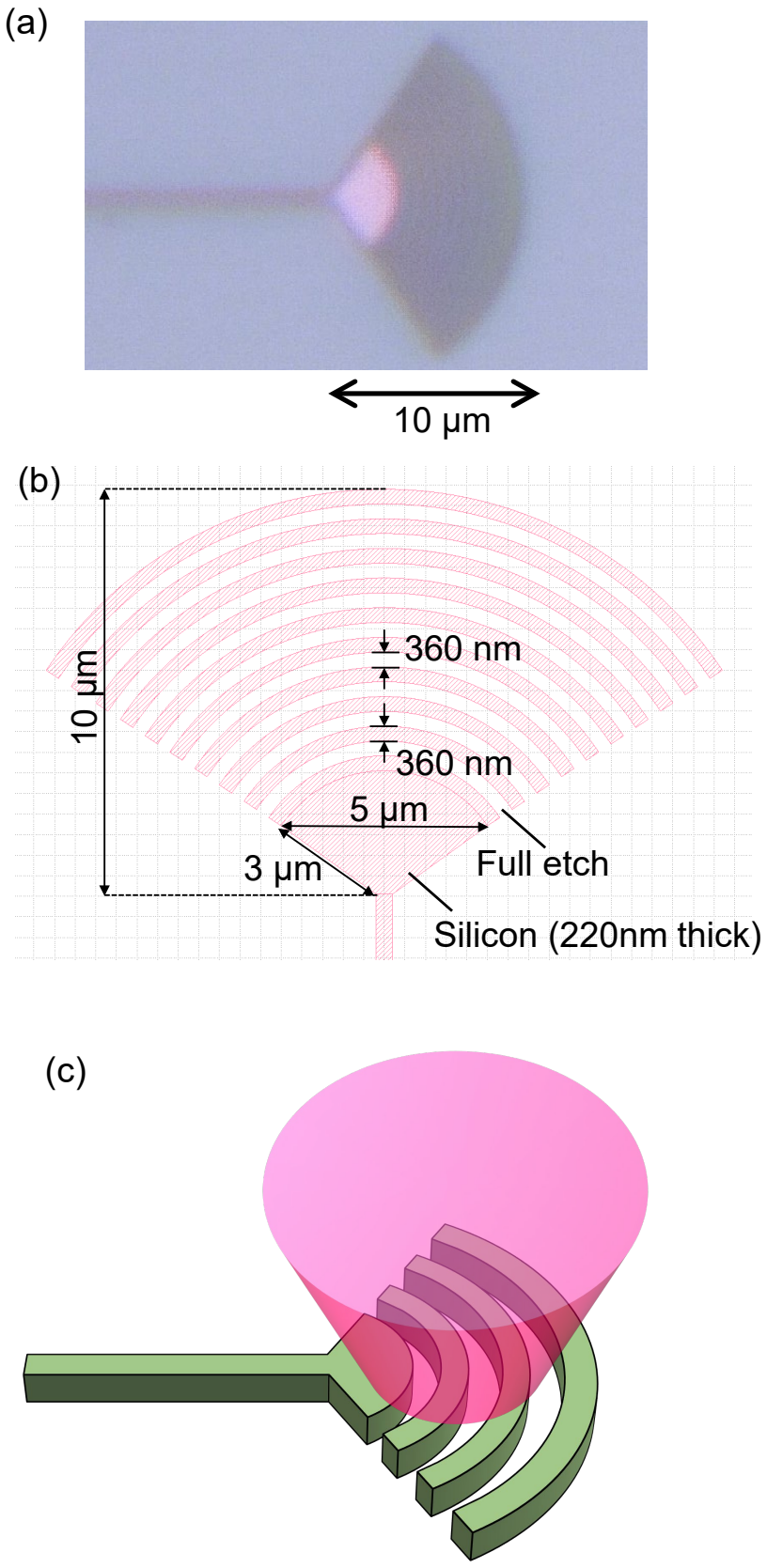

Fig. 3.6: (a) Microscope photograph of the grating antennas. (b) 2D schematic of the grating antennas. (b) 3D schematic of the grating antennas.

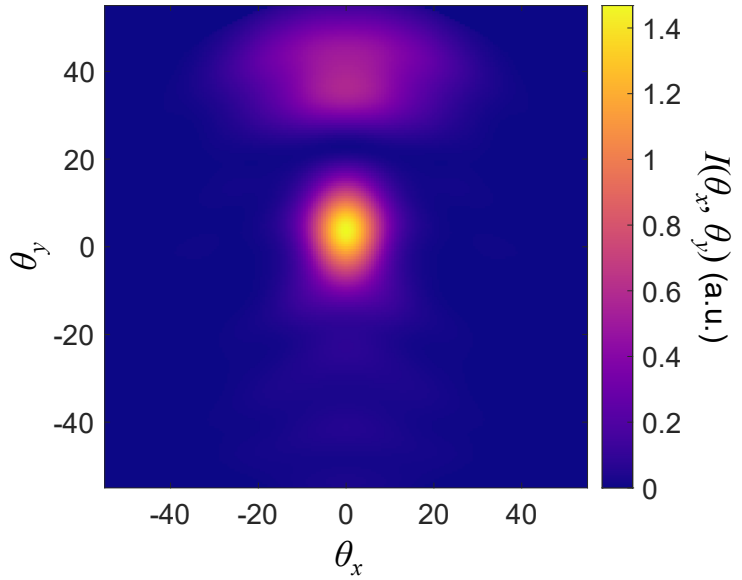

Fig. 3.7: Radiation intensity profile of a single optical antenna.

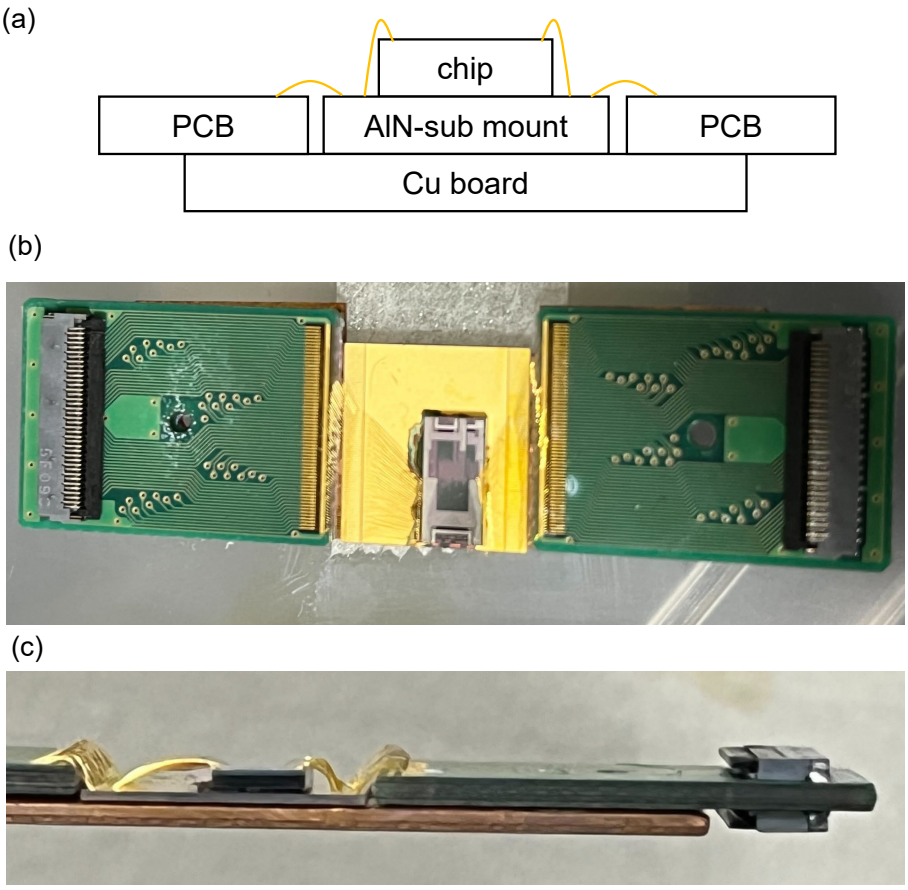

Fig. 3.8: (a) Cross-sectional schematic diagram of the mounted chip. (b) Top-view photograph of the mounted chip. (c) Side-view photograph of the mounted chip.

boards (PCBs) via the AlN chip carrier*5. The AlN chip carrier and PCBs were bonded on a copper board*6. The mounted chip was fixed on a chip stage with a thermo-electric cooler (TEC). The TEC operated so that the chip temperature was 20 °C*7. This temperature control helps to ensure the reproducibility of the measurement, especially the driving condition. Furthermore, it helps to reduce the thermal crosstalk between thermo-optic phase shifters so that the optimization of the phase shifters will converge faster.

2. Experiment setup

Next, we describe the experiment setup. The schematic and the photograph of the experiment setup are depicted in Fig. 3.9 and Fig. 3.10, respectively. A continuous-wave 1550-nm-wavelength laser light source was launched and power-controlled by a variable optical attenuator so that the optical power was appropriate for the dynamic range of the InGaAs camera, which is used to observe the FFP of the OPA. The light was then polarization controlled by a polarization controller (PC) so that the light would couple to the TE mode of the silicon waveguide*8. The light was coupled to the chip via a lensed fiber, which allowed for a coupling loss of approximately 4.5 dB per facet. The lensed fiber was aligned to the input of the chip using a 6-axis electrical stage. The output light of OPA was emitted above the chip and collimated by a plano-convex lens (Focal length: $f_1 = 100$ mm, Diameter: $D_1 = 2$-inch). A mirror was then used to change the direction of light so that the light propagates approximately parallel to the optical table*9. The light was then focused by another plano-convex lens (Focal length: $f_2 = 100$ mm, Diameter: $D_2 = 2$-inch) to image the NFP of the OPA output. The NFP formed here was used for two purposes: to align the lensed fiber to the chip, and to filter out undesired light. For the alignment, first, the optical fiber was roughly aligned to the input waveguide position using the visible NFP observed using a zoom lens and a visible camera. Here, a movable mirror was inserted to observe the NFP so that the optical path could be switched to the FFP at any time. The infrared NFP was then observed using an InGaAs camera. The fiber was aligned to the chip input waveguide so that the output light from the grating couplers was maximized. Using the NFP observed here, undesired light, including the

the OPA chip can be efficiently temperature-controlled using an external thermo-electric cooler. The reason that silver paste was selected as an glue is also to improve the thermal conductivity.

*5 A company called Micromodule conducted the wire bonding process [192].

*6 Again, the reason of choosing copper board was to maximize the thermal conductivity.

*7 However, after further experiences, we have noticed that it is better to set the temperature at a higher temperature, such as 50 °C. One possible reason of this is that when the heating on the chip is significant, the TEC is no longer capable to cool the chip down to 20 °C under room temperature ambient.

*8 In that sense, the fibers to deliver the light from laser to chip were well fixed so that the polarization state will not change over time.

*9 This kind of configuration was chosen because it allows for keeping the system for aligning the fiber to the chip relatively similar to previous system in our laboratory for evaluating waveguide based devices.

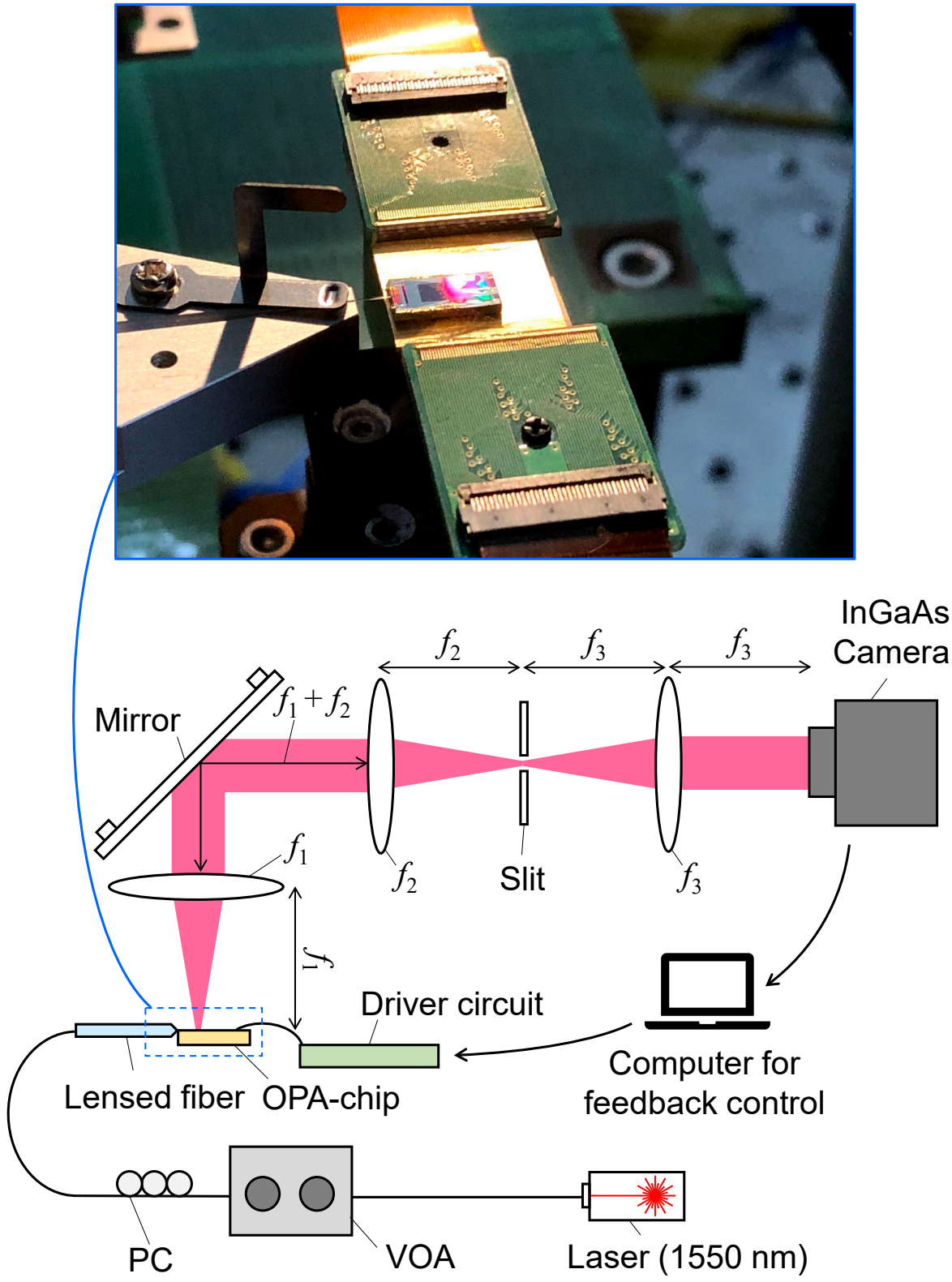

Fig. 3.9: Schematic of the experiment setup.

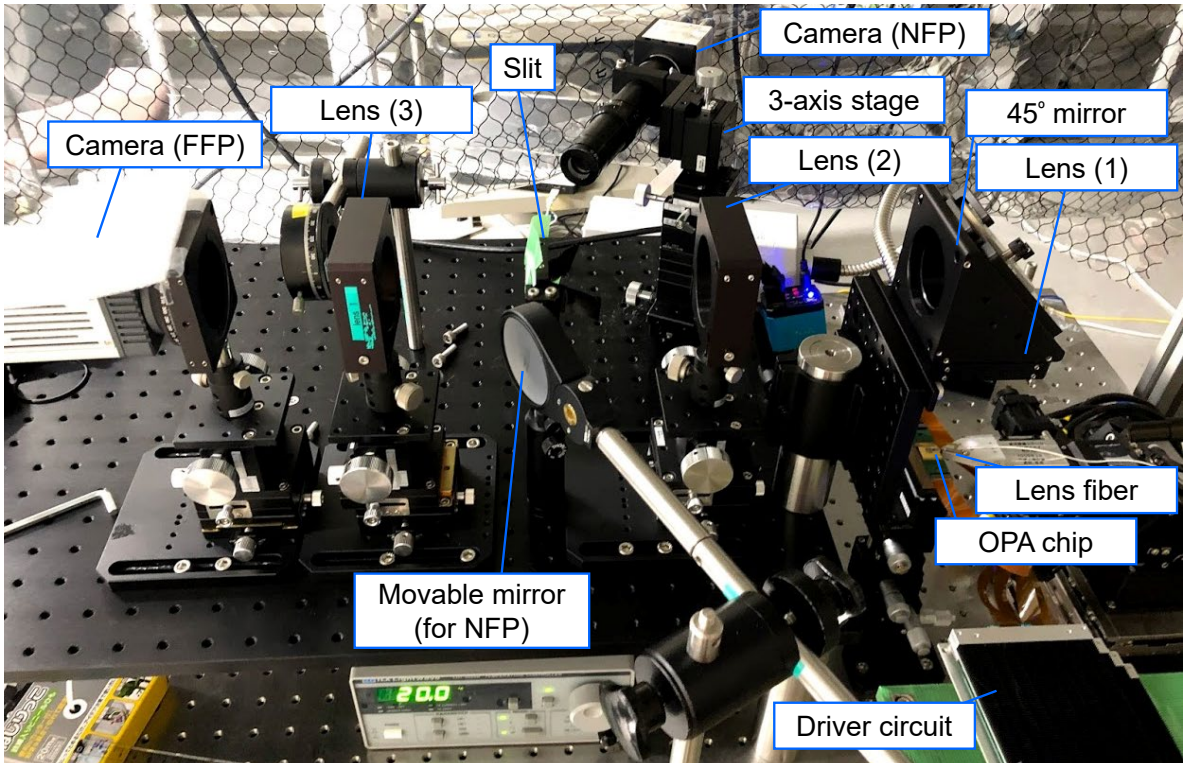

Fig. 3.10: Photograph of the experiment setup.

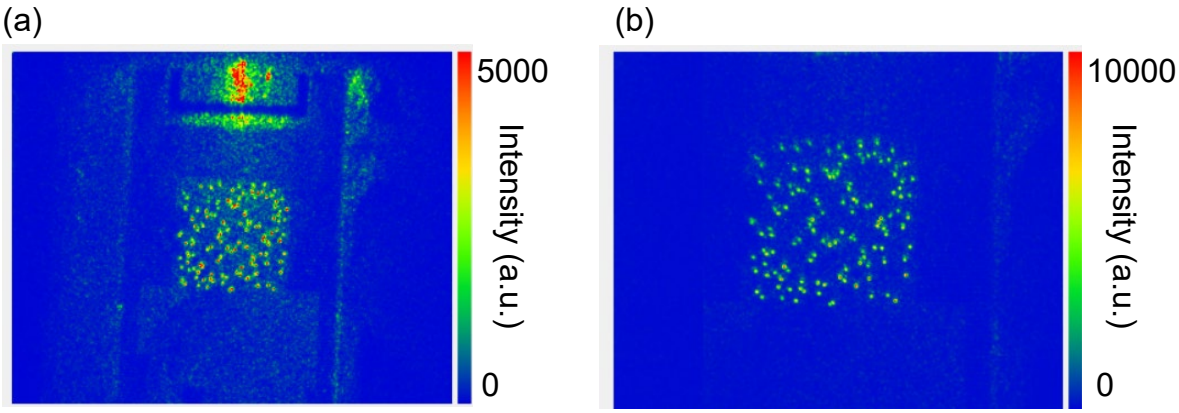

Fig. 3.11: The infrared NFP observed using an InGaAs camera. (a) Without a mechanical slit. Undesired light, mainly the light scattered at the input of the chip, is observed. (b) With a mechanical slit for filtering. Undesired light is eliminated.

light scattered at the OPA input due to mode mismatch was filtered out using a hand-made mechanical slit (Fig. 3.11). Another plano-convex lens (Focal length: f_3 = 100 mm, Diameter: D_3 = 2-inch) was then used to re-collimate the light and to form the FFP. Finally, an InGaAs camera (Hamamatsu Photonics, C12741-03) was used to observe the FFP.

The phase shifters were driven by an FPGA-based driver circuit with 12-bit DACs and 6 V_{pp}

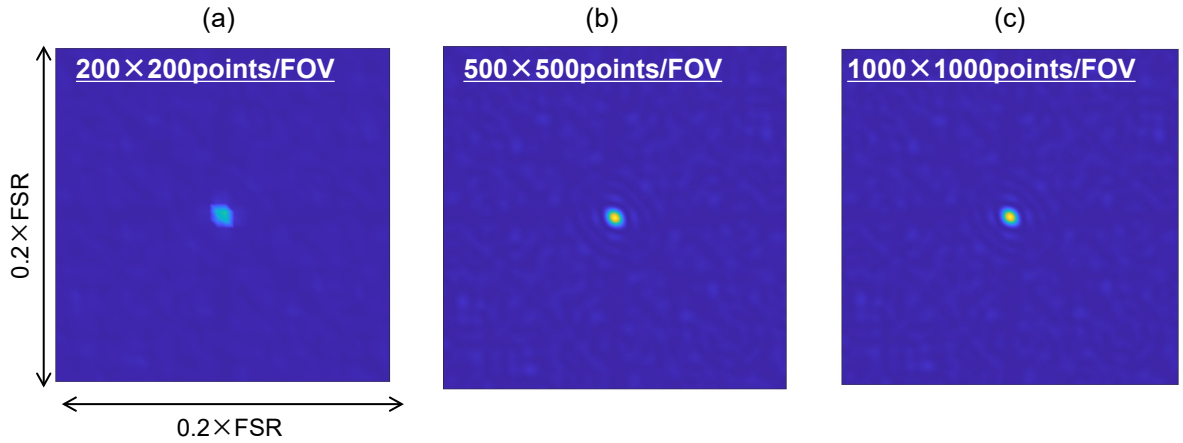

Fig. 3.12: Numerically simulated FFP of a Costas-array-based NROPA ($N = 127$) considered to be observed using camera with limited number of pixels. (a) A camera with 200×200 points per FOV. (b) A camera with 500×500 points per FOV. (c) A camera with 1000×1000 points per FOV.

voltage range*[10]. The driver circuits were cooled by external fans so that the output voltage signal was stabilized with high accuracy. The driver circuit was controlled by a computer, which is also connected to the InGaAs camera, through a USB interface. Flexible flat cables were used to connect the driver circuit to the PCBs, which the OPA was wire-bonded to.

Regarding the lens system design, we should note that the design of the lens system is not as trivial due to the high spatial resolution of the OPA. The number of pixels per FOV must be sufficiently large so that the accurate profile of the FFP can be observed. Fig. 3.12 depicts the impact of the limited number of pixels when observing the FFP for the case of Costas-array-based NROPA ($N = 127$). We can see that with 500×500 pixels per FOV, the FFP can be accurately observed. The InGaAs camera had 640×512 pixels, while the size of each pixel was $20\,\mu\text{m} \times 20\,\mu\text{m}$. Therefore, the FFP could be finely observed if the size of the FOV is approximately 10 mm × 10 mm. The FOV for each axis in terms of radiation angle is $\theta_{\text{FOV}} = 5.92°$, and the length corresponding to the FOV on the camera plane l_{FOV} is

$$l_{\text{FOV}} = \frac{f_1 f_3}{f_2}\theta_{\text{FOV}}. \tag{3.2}$$

Therefore, for the experiment setup presented here, $l_{\text{FOV}} \simeq 10.3\,\text{mm}$, which is suitable for the observation of the entire FOV with a single shot. The other thing that must be considered is the numerical aperture (NA) and the of entrance pupil size (i.e., the diameter) of the lens. The NA of the lens defines the range of radiation angle of light that could be collimated. Therefore,

*[10] The driver circuit was developed by Keiichi Iguchi of Electrodesign.

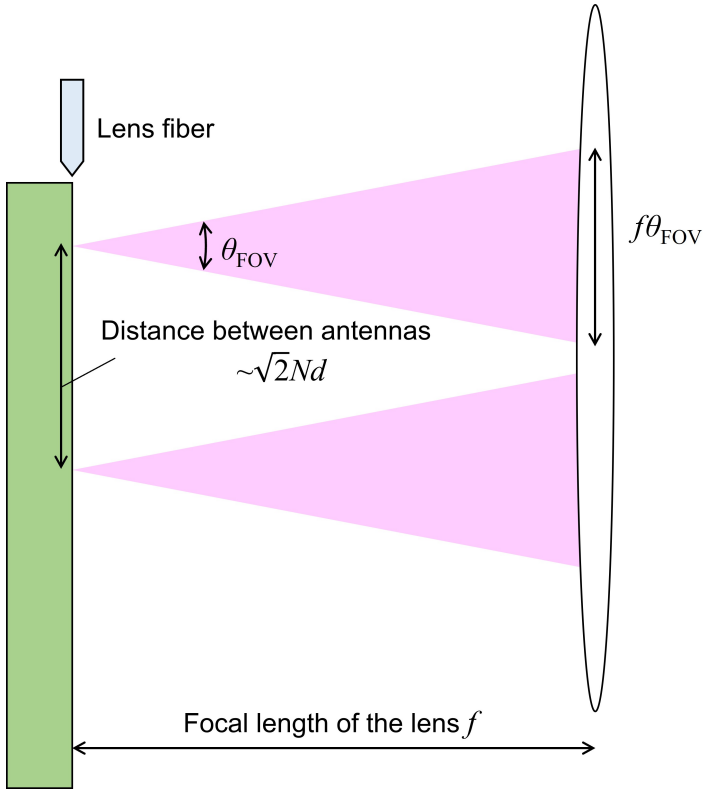

Fig. 3.13: Schematic diagram depicting the required pupil size and NA of the lens.

the NA must be sufficiently larger than θ_{FOV}. On the other hand, the entrance pupil defines the area of the target plane that could be observed. Therefore, the lens must be relatively large. Especially in this particular case, $d = 15\,\mu\mathrm{m}$ and $N = 127$ will require the pupil size to be bigger than $\sqrt{2}Nd \simeq 2.7\,\mathrm{mm}$. Moreover, for the full range of θ_{FOV} of light from every antenna to be collimated, the pupil must be larger than $f\theta_{\mathrm{FOV}} + \sqrt{2}Nd$, which sometimes will require a careful selection of the lens (Fig. 3.13). Furthermore, another issue that made the situation problematic for this specific case was that it was desirable to observe the lens fiber with the same lens system for the observation of FFP. This is because we had to align the lens fiber to the chip first using a 6-axis stage, and the measurement of the beam profile had to be performed subsequently. As a result, the required pupil size becomes relatively large. Therefore, we chose a large lens with a diameter of 2 inches and a sufficiently large NA of 0.25 so as to simultaneously ensure accurate evaluation of the FFP and the observation of lens fiber.

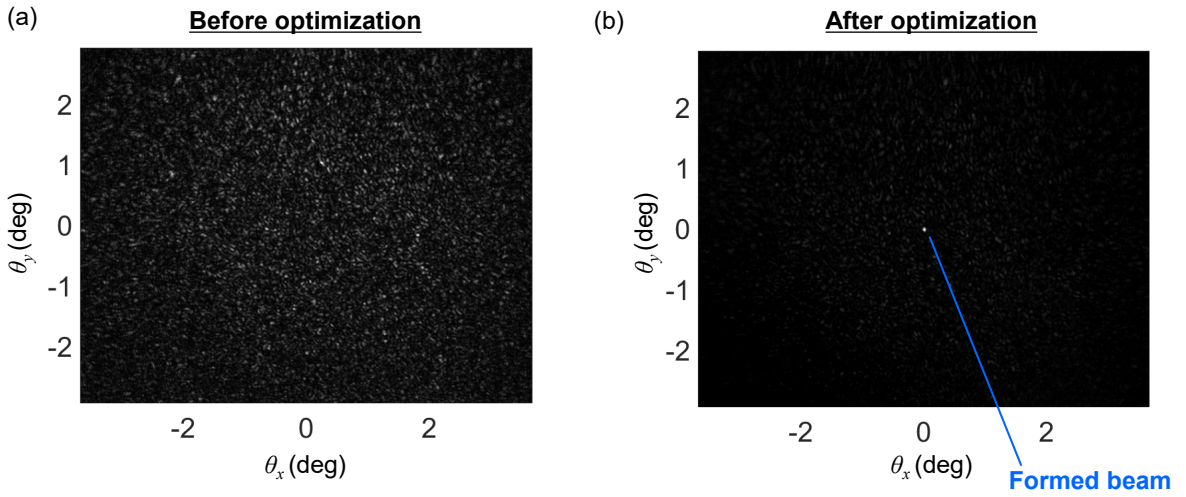

Fig. 3.14: The experiumentally obtained 2D beam steering to different angles defined by (θ, ψ)

3. Experiment result

Without optimizing the driving condition of the phase shifters, the FFP of the OPA becomes a pseudorandom speckle [Fig. 3.14(a)], although the waveguides are designed so that the optical path length of each port is identical.

This is due to the accumulated optical phase error at the optical waveguides induced by the deviation of waveguide width and height. Therefore, in order to obtain a fine beam, we ran an optimization based on the modified rotating element field vector method [146, 147] (see algorithm 1) for each steering angle so that the driving condition of the phase shifters is optimized (Fig. 3.14). After the optimization, a nice beam is obtained at the steering angle [Fig. 3.14(b)]. The pseudo-code depicted below describes the optimization algorithm (Algorithm 1, see Fig. 3.15 for the help of your understanding). Here, j and $j_{\max}$ denote the count of loops and the number of loops, I_0 denotes the intensity of the beam at the pixel of interest, which is obtained from the camera, I_{temp} is a variable to store the temporary information of the intensity, V_h $(h = 1, 2, ..., h_{\max})$ denotes the values of voltages that could be applied to the phase shifters through the FPGA board (determined by the voltage range and bit resolution of the DAC), v_n $(n = 1, 2, ..., N)$ denotes the voltage applied to the phase shifters through the FPGA board, and v_{temp} is a variable to store the temporary value of the voltage. This algorithm is known to converge quickly at an ideal condition with a very small number of repetition $j_{\max}$, but in our case, due to some non-ideal conditions such as the thermal crosstalk between phase shifters and the deviation of the input power due to the fluctuation of the position of the lens fiber, a relatively large number of repetition of $j_{\max} \geq 5$ was required to obtain a fine beam. We should note that if the phase shifters are crosstalk-free, the algorithm can converge much faster [142]. Moreover, if the on-chip phase monitors can be integrated,

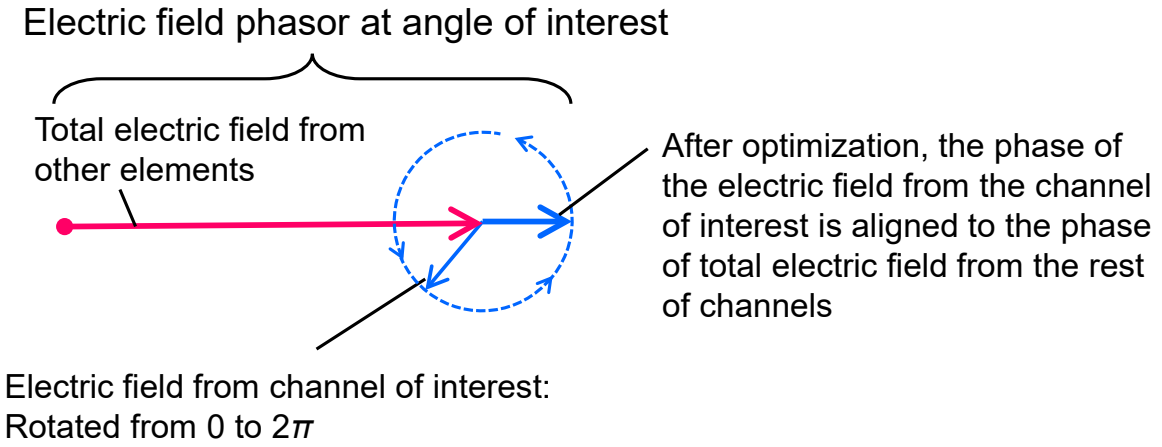

Fig. 3.15: Phasor picture of the rotating element field vector method.

the phase shifters should be able to be calibrated deterministically [65, 148].

Algorithm 1 Modified Rotating Element Field Vector Method

$j \leftarrow 1$
initialize v_n {Set initial votage to all phase shifters $(n = 1, 2, ..., N)$}
while $j < j_{\max} + 1$ **do**
  $n \leftarrow 1$
  while $n < N + 1$ **do**
    renew I_0 {Get the intensity from camera}
    $I_{\text{temp}} \leftarrow I_0$
    $v_{\text{temp}} \leftarrow v_n$
    $h \leftarrow 1$
    while $h < h_{\max} + 1$ **do**
      $v_n \leftarrow V_h$ {Renew the voltage that is applied to the n-th phase shifter}
      renew I_0
      if $I_{\text{temp}} < I_0$ **then**
        $I_{\text{temp}} \leftarrow I_0$ {Renew the champion-data for the intensity.}
        $v_{\text{temp}} \leftarrow V_h$ {Remember the voltage value that gave the champion-data.}
      end if
      $h \leftarrow h + 1$
    end while
    $v_n \leftarrow v_{\text{temp}}$ {Finalize the voltage to the condition of champion-data.}
    $n \leftarrow n + 1$
  end while
  $j \leftarrow j + 1$
end while

Finally, we evaluated the beam after optimization. We should note that in order to purely evaluate the impact of the array layout, we have pre-acquired the envelope function of the FFP and have compensated for its impact. An example of the measured beam profile $I(\boldsymbol{\Theta})$ is depicted in Fig. 3.16. A fine beam shape with a sharp intensity peak at $(\theta_x, \theta_y) = (0°, 0°)$ is obtained. The FWHM (defined by the average of the FWHM in θ_x, θ_y direction, which should be reasonable since the main lobe was almost homogeneous) of the beam is 0.0428°. The cross-section of the beam at the center ($\theta_y = 0$) is depicted in Fig. 3.16(b), where the experimental result (red) is compared with the theoretically obtained profile (black). Excellent agreement between the experiment and the theory is obtained. Figure 3.16(c) shows the maximum intensity along θ_y as a function of θ_x, from which the sidelobe suppression ratio is derived to be 6.3 dB. Theoretically, this can be further reduced to 12.3 dB. The possible reasons for this discrepancy are the failure of the optimization process to reach the global optimum and the unequal optical power emitted from each antenna due to fabrication errors.

Figure 3.17 shows the results of 2D beam steering over the $5.92° \times 5.92°$ FOV. The FWHM of the beam is roughly constant over the entire FOV, in agreement with the theory. The residual deviation is attributed to the non-zero aberrations at the edges of the lens system. For clarity, we illustrate in Fig. 3.18 the measured beam steering result in the θ_x [Fig. 3.18(a)] and the θ_y [Fig. 3.18(b)] direction at $\theta_y = 0°$ and $\theta_x = 0°$, respectively. Beam steering across the entire FOV is successfully demonstrated in both axes[*11].

From these results, we can derive the number of resolvable points as $(\mathrm{FOV}/\mathrm{FWHM})^2 \simeq 19,000$ points, corresponding to the theoretical limit of $\simeq N^2$. To the best of our knowledge, this is the largest number of resolvable points achieved by an OPA without sweeping the wavelength. Compared with previous representative work of high-resolution OPA, this improvement is drastic. For example, in [34] and [86], the authors demonstrate a device with $\simeq 500$ resolvable points using an OPA with $N = 128$, based on a pseudorandomly-generated array or array generated using genetic algorithm, respectively. Compared to these work, our NROPA far exceed them in spatial resolution with almost the same N. Moreover, NROPA is based on a theoretical concept whose optimality is justified, while the previous work was a rather brute-force approach. In [75], the authors demonstrate an ultra-large-scale uniformly-spaced OPA ($N = 8192$), whose number of resolvable points should be approximately 8000 points. Despite the extremely smaller N of our NROPA, our OPA can outperform such OPA in terms of spatial resolution.

[*11] While the steering range for θ_x in Fig. 3.18(a) slightly exceeds the FOV, we could not confirm the grating lobes that we expected to observe. The possible reasons for this are the slightly degraded periodicity of the Costas array spacings due to the fabrication non-uniformity of the antennas distributed in a large area and the aberration at the edges of the lens system, which may have blurred the higher-order diffraction.

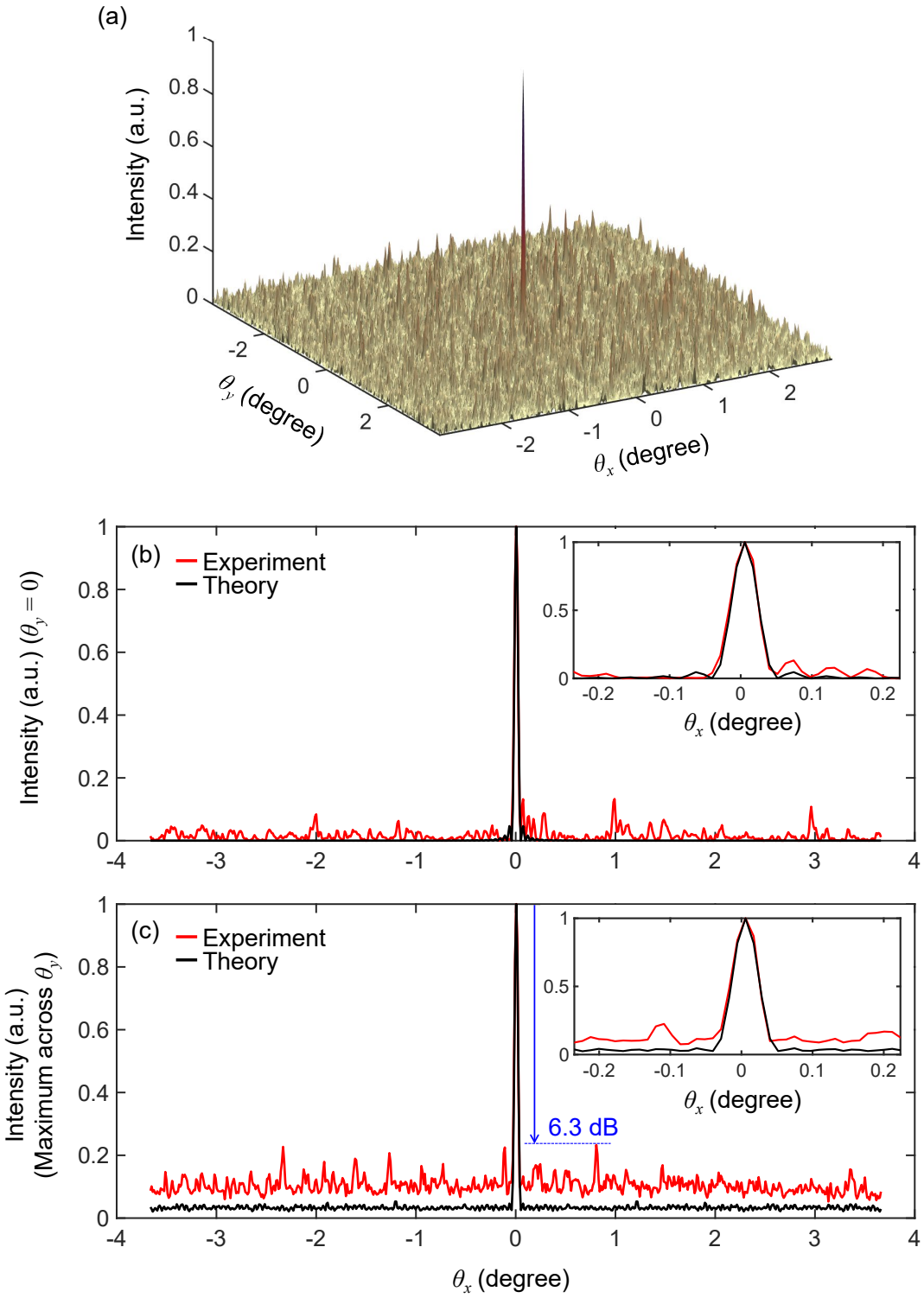

Fig. 3.16: The measured beam intensity profile $I(\boldsymbol{\Theta})$ after optimization. (a) Measured overall beam profile, emitted from the OPA chip. (b) The cross section of the beam at $\theta_y = 0$ [i.e., $I(\theta_x, \theta_y = 0)$]. (c) The maximum value of the beam intensity along the θ_y direction $\left\{f(\theta) = \max\left[I(\theta_x, \theta_y); \theta_y \text{in FOV}\right]\right\}$. In (b) and (c), the magnified views are shown in the insets. The experimental results (red) are compared with the theoretical profiles (black)

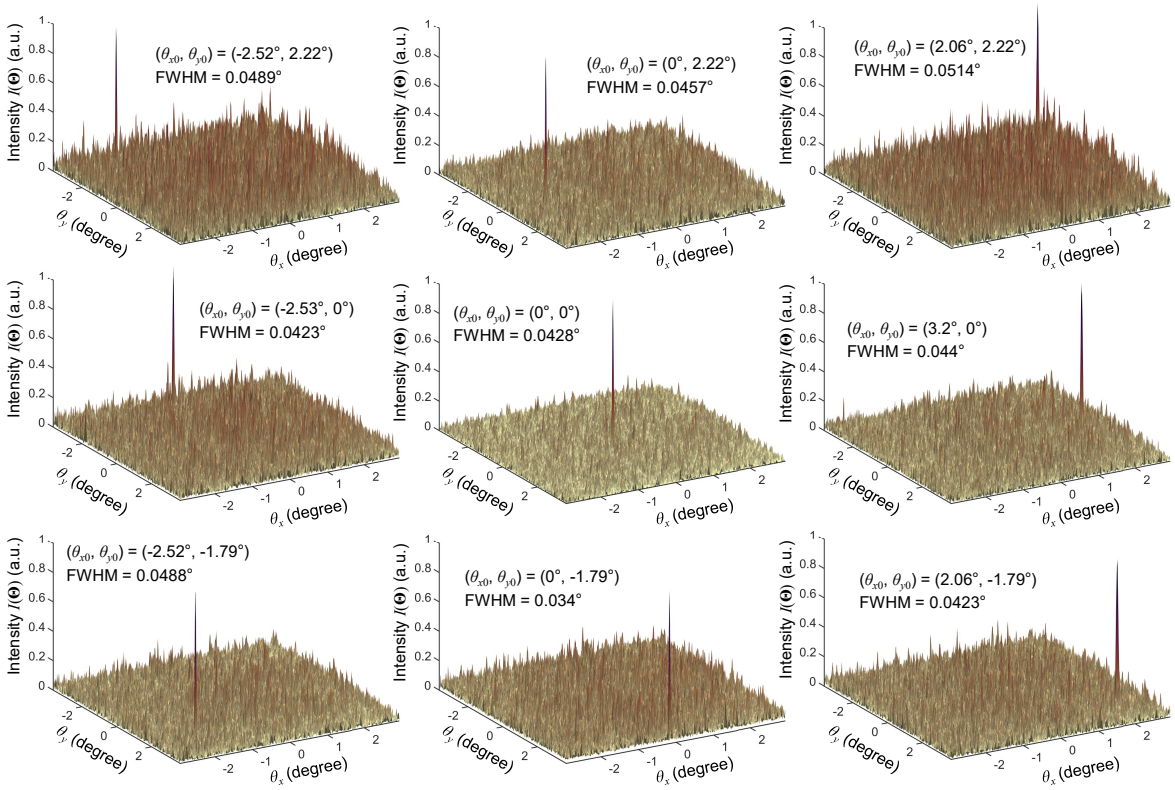

Fig. 3.17: The experiumentally obtained 2D beam steering to different angles defined by $\mathbf{\Theta}_0 = (\theta_{x0}, \theta_{y0})$

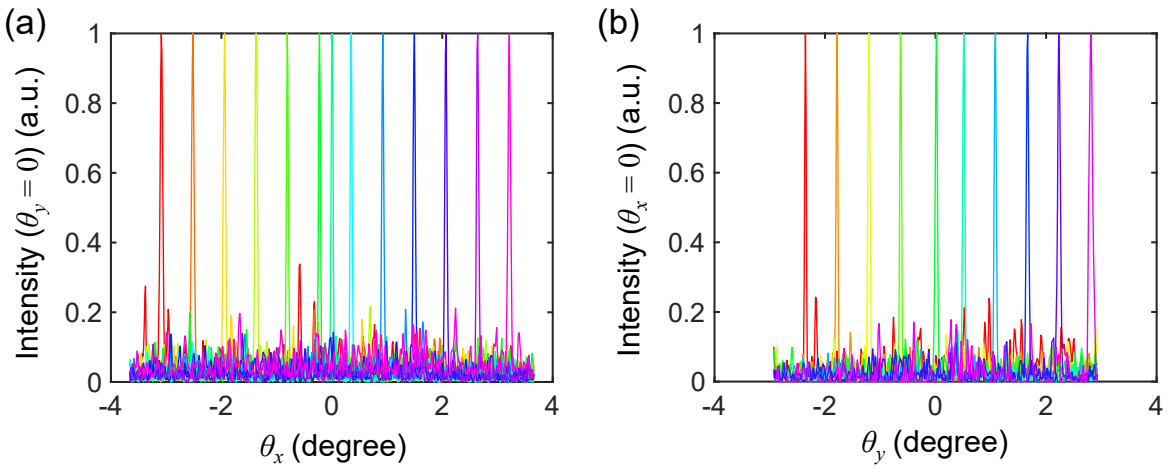

Fig. 3.18: The experiumentally obtained 2D beam steering to different angles defined by (θ, ψ)

4. Summary

In this chapter, we have presented the experimental demonstration of the NROPA concept. We have designed and fabricated a silicon photonic OPA chip. An experiment system consisting of the OPA chip, lens system, and the electrical circuit was built to evaluate the fabricated chip. Using the silicon photonic NROPA, we have experimentally demonstrated a state-of-the-art number of resolvable points of $\simeq 19,000$.

3.A Beam profile without compensating the envelope function.

For clarity, we illustrate the raw beam profile without compensating for the impact of the envelope function in Fig. 3.19 In Fig. 3.19(b, c), the raw data without compensating for the envelope function (blue) is displayed together with the envelope function (black-dotted) and the beam profile after removing the envelope function (red).

The envelope function was acquired by 3 steps. First, we obtained the FFP of OPA when we drove the phase shifters with 1000 sets of different random signals. Then, we averaged the FFP for 1000 patterns. Finally, the averaged FFP was fit to a gaussian beam profile.

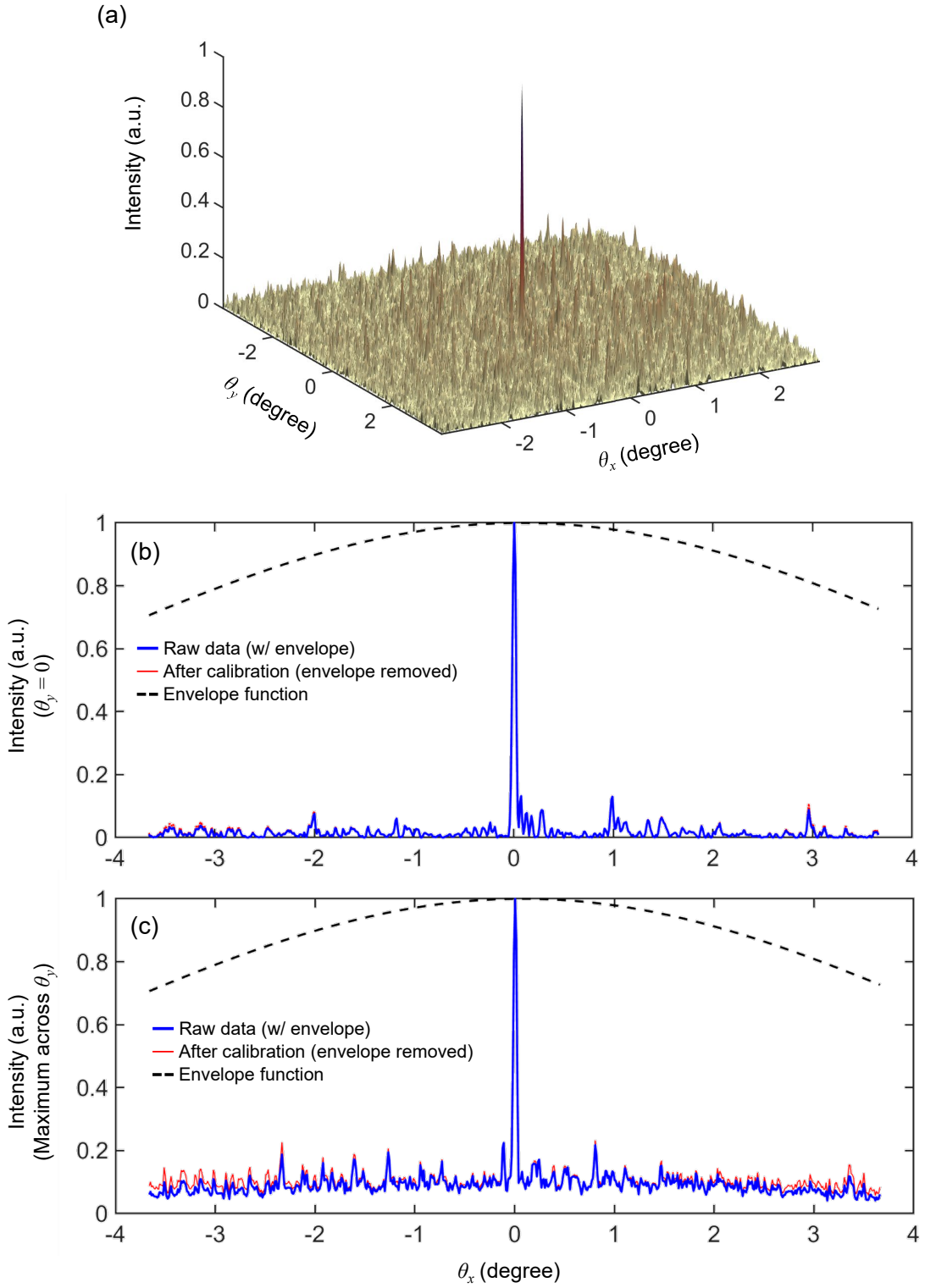

Fig. 3.19: The measured beam intensity profile $I(\boldsymbol{\Theta})$ after optimization, without compensating for the envelope function. (a) Measured overall beam profile, emitted from the OPA chip. (b) The cross section of the beam at $\theta_y = 0$ [i.e., $I(\theta_x, \theta_y = 0)$]. (c) The maximum value of the beam intensity along the θ_y direction $\left\{f(\theta) = \max\left[I(\theta_x, \theta_y); \theta_y \text{in FOV}\right]\right\}$.

CHAPTER 4

ANALYSIS OF SPECKLE-BASED SINGLE-PIXEL IMAGING USING UNIFORM AND NON-REDUNDANT OPTICAL PHASED ARRAY

In Chapter 2 and Chapter 3, we studied the NROPA for beam steering application. By the use of NROPA, drastic reduction of N for a given number of resolvable points, leading to a significant reduction of the driving complexity of the OPA. However, precise tuning of the optical phase shifters are still mandatory in the beam steering scheme. As a result, some degree of complexity will remain. The speckle-based single-pixel imaging (SSPI) scheme can open the pathway towards an ultimately simplified imaging scheme, as it does not require precise tuning of phase shifters, and instead, the phase shifters can just be driven by pseudorandom signals. Although there are several previous reports of OPA-based SSPI (OPA-SSPI), the number of resolvable points was limited for the case of SSPI using UOPA. Moreover, a quantitative or theoretical understanding of the resolution in such an imaging scheme was not clear. In this Chapter, we present a comprehensive theoretical and numerical analysis of OPA-SSPI using UOPA and NROPA. A quantitative and theoretical understanding of the number of resolvable points is presented, and the effectiveness of NROPA-based SSPI is clearly verified.

1. Imaging scheme

Figure 4.1 shows the schematic of OPA-SSPI. The input light to the OPA is distributed to N waveguides by a $1 \times N$ splitter, phase controlled by N phase shifters, and finally emitted to free space via N optical antennas. For the sake of simplicity, a one-dimensional (1D) OPA is considered in this chapter, and assume that the optical antennas are simply edge-emitting waveguides as shown in Fig. 1. By driving the phase shifters with pseudo-random signals, K different speckle-like intensity patterns $I_k(\theta)$ $(k = 1, 2, .., K)$ are sequentially generated (θ denotes the angle at the far field), which are used to illuminate the target. The optical power transmitted through the target S_k $(k = 1, 2, .., K)$ is then detected by a single-pixel

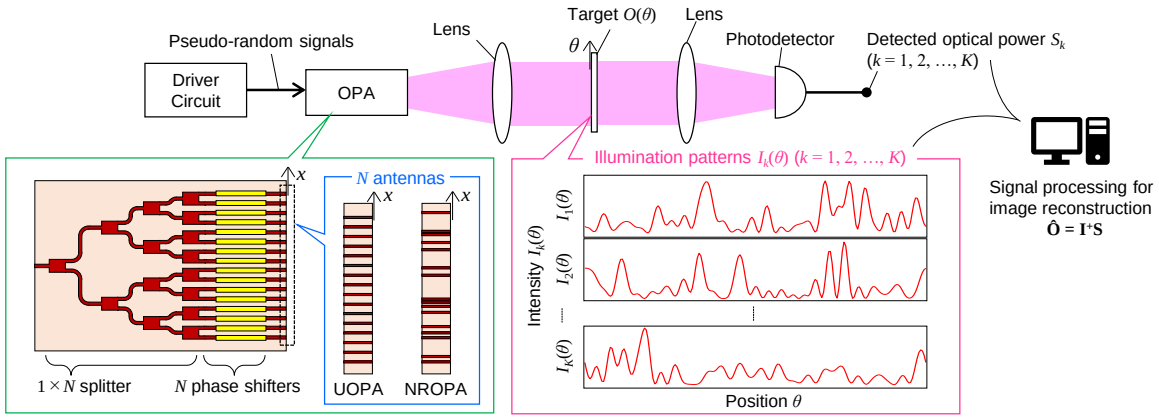

Fig. 4.1: Schematic of SSPI system using OPA.

photodetector. Note that

$$S_k = \int I_k(\theta) O(\theta) \mathrm{d}\theta, \tag{4.1}$$

where $O(\theta)$ is the target transmittance distribution*[1]. If we discretize the 1D space along θ by P pixels, Eq. (4.1) is written as

$$S_k = \mathbf{i}_k^{\mathrm{T}} \mathbf{O}, \tag{4.2}$$

where $\mathbf{i}_k$ and $\mathbf{O}$ are $P \times 1$ vectors describing the discretized forms of $I_k(\theta)$ and $O(\theta)$, respectively.

After switching the illumination K times, we obtain the simultaneous linear equation

$$\mathbf{S} = \mathbf{I}\mathbf{O}, \tag{4.3}$$

where $\mathbf{I} \equiv [\mathbf{i}_1, \mathbf{i}_2, ..., \mathbf{i}_K]^{\mathrm{T}}$ is a $K \times P$ matrix, which we refer to as the illumination matrix, and $\mathbf{S} \equiv [S_1, S_2, ..., S_K]^{\mathrm{T}}$ is a $K \times 1$ vector, which we refer to as the signal vector. Finally, we can retrieve the image by calculating

$$\hat{\mathbf{O}} = \mathbf{I}^+ \mathbf{S}, \tag{4.4}$$

where $\hat{\mathbf{O}}$ is the reconstructed image of the target $\mathbf{O}$, and $\mathbf{I}^+$ denotes the Moore-Penrose inverse of $\mathbf{I}$.

*[1] Here, for the sake of simplicity, we limit our discussion to the case of using the transmitted light. However, this method can be performed similarly using the reflection light or the fluorescence light, which allows for the realization of practical system.

2. Theoretical analysis

First we derive the general form of **I** without assuming any particular array layout. Compared to the analysis presented in Chapter 2, here we modify the treatment of the equation so as to interpret the case of randomly driving the phase shifters, focus on the case when the intensity patterns are discretized, and pay much attention to the "degree of freedom" or the "dimensionality" of the intensity patterns. Since the image is retrieved by calculating Eq. (4.4), illumination matrix **I** has a critical impact on the imaging performance. In particular, rank (**I**) represents the number of independent information of the target **O** that can be retrieved through Eq. (4.4). For convenience, therefore, we employ rank(**I**) to quantitatively evaluate the number of resolvable points.

2.1 General description of the FFP from an OPA

Assuming that the optical modes at all antennas are identical and the phase shifters are lossless, the electric field distribution of the NFP emitted from an OPA can be written as

$$E(x) = \sum_{n=1}^{N} u(x - x_n) \exp\left(\mathrm{i}\phi_n\right) = u(x) * \sum_{n=1}^{N} \delta(x - x_n) \exp\left(\mathrm{i}\phi_n\right), \tag{4.5}$$

where x is defined along the antenna array as shown in Fig. 1, $u(x)$ is the electric field distribution of the light emitted from a single antenna, ϕ_n $(n = 1, 2, ..., N)$ is the optical phase of light from the n-th antenna, $\delta(x)$ is the Dirac's delta function, $*$ denotes the convolution operation, and x_n represents the position of the n-th antenna.

The far-field pattern (FFP) $F(\theta)$ is described as the Fourier transform of the NFP, so that

$$F(\theta) = \sum_{n=1}^{N} U(\theta) \exp\left[\mathrm{i}\left(\beta_0 x_n \theta + \phi_n\right)\right]. \tag{4.6}$$

Here, $U(\theta)$ is the Fourier transform of $u(x)$, and β_0 is the wavenumber of light in free space. The intensity distribution of the FFP $I(\theta)$ is the absolute square of $F(\theta)$, i.e.,

$$\begin{aligned} I(\theta) = |F(\theta)|^2 &= \sum_{n'=1}^{N} U^*(\theta) \exp\left[-\mathrm{i}\left(\beta_0 x_{n'} \theta + \phi_{n'}\right)\right] \sum_{n=1}^{N} U(\theta) \exp\left[\mathrm{i}\left(\beta_0 x_n \theta + \phi_n\right)\right] \\ &= |U(\theta)|^2 \sum_{n'=1}^{N} \sum_{n=1}^{N} \exp\left(\mathrm{i}\beta_0 \Delta x_{n,n'} \theta\right) \exp\left(\mathrm{i}\Delta\phi_{n,n'}\right), \\ &= |U(\theta)|^2 \left[N + \sum_{n \neq n'} \exp\left(\mathrm{i}\beta_0 \Delta x_{n,n'} \theta\right) \exp\left(\mathrm{i}\Delta\phi_{n,n'}\right)\right] \end{aligned} \tag{4.7}$$

where $\Delta x_{n,n'} \equiv x_n - x_{n'}$ and $\Delta\phi_{n,n'} \equiv \phi_n - \phi_{n'}$. The first term N corresponds to the summation for the cases of $n = n'$, which resembles the FFP of light from a single antenna and is independent on the driving condition. The second term describes the interference fringes of the light from the n-th and the n'-th optical antennas, whose spatial frequency is determined by the displacement $\Delta x_{n,n'}$ between the n-th and the n'-th optical antennas. The amplitudes of the interference fringes $\exp\left(\mathrm{i}\Delta\phi_{n,n'}\right)$ vary depending on the phase difference $\Delta\phi_{n,n'}$ between the n-th and the n'-th antennas. Note that Eq. (4.7) can be reduced to

$$\begin{aligned} I(\theta) = |U(\theta)|^2 \left\{ N + \sum_{n<n'} \left[\exp\left(\mathrm{i}\beta_0 \Delta x_{n,n'}\theta\right) \exp\left(\mathrm{i}\Delta\phi_{n,n'}\right) + \exp\left(\mathrm{i}\beta_0 \Delta x_{n',n}\theta\right) \exp\left(\mathrm{i}\Delta\phi_{n',n}\right) \right] \right\} \\ = |U(\theta)|^2 \left[N + 2 \sum_{n<n'} \cos\left(\beta_0 \Delta x_{n,n'}\theta + \Delta\phi_{n,n'}\right) \right], \end{aligned} \tag{4.8}$$

from which we can easily confirm that Eq. (4.7) describes a real-valued function. As we can see from Eq. (4.7), $|U(\theta)|^2 \exp\left(\mathrm{i}\beta_0 \Delta x_{n,n'}\theta\right)$ constitute the set of the functional space spanning the illumination patterns $I_k(\theta)$ $(k = 1, 2, ..., K)$. Since $|U(\theta)|^2$ has relatively weak dependence on θ, the orthogonality of the vectors constituting this spanning set is almost solely determined by the relative position $\Delta x_{n,n'}$ between the n-th and the n'-th optical antennas.

For convenience of explanation and numerical analysis, we discretize the illuminated space by P pixels, similar to the previous section. We define $P \times 1$ vectors $\mathbf{a}_{n,n'}$, $\mathbf{c}$, and $\mathbf{i}$ as

$$|U(\theta)|^2 \exp\left(\mathrm{i}\beta_0 \Delta x_{n,n'}\theta\right) \overset{\text{discretize}}{\longrightarrow} \mathbf{a}_{n,n'}, \tag{4.9}$$

$$|U(\theta)|^2 \overset{\text{discretize}}{\longrightarrow} \mathbf{c}, \tag{4.10}$$

and

$$I(\theta) \overset{\text{discretize}}{\longrightarrow} \mathbf{i}, \tag{4.11}$$

respectively, where $\overset{\text{discretize}}{\longrightarrow}$ denotes the discretization with respect to θ. Equation (4.7) is then discretized as

$$\mathbf{i} = N\mathbf{c} + \sum_{n \neq n'}^{N} \exp\left(\mathrm{i}\Delta\phi_{n,n'}\right) \mathbf{a}_{n,n'}. \tag{4.12}$$

We can further reduce this equation as

$$\mathbf{i} = \mathbf{A}\mathbf{q}, \tag{4.13}$$

where

$$\mathbf{A} \equiv \begin{bmatrix} \mathbf{c} & \mathbf{a}_{1,2} & \mathbf{a}_{1,3} & \dots & \mathbf{a}_{N,N-2} & \mathbf{a}_{N,N-1} \end{bmatrix} \tag{4.14}$$

is a $P \times \left(N^2 - N + 1\right)$ matrix and

$$\mathbf{q} \equiv \begin{bmatrix} N \\ \exp\left(\mathrm{i}\Delta\phi_{1,2}\right) \\ \exp\left(\mathrm{i}\Delta\phi_{1,3}\right) \\ \vdots \\ \exp\left(\mathrm{i}\Delta\phi_{N,N-2}\right) \\ \exp\left(\mathrm{i}\Delta\phi_{N,N-1}\right) \end{bmatrix} \tag{4.15}$$

is a $\left(N^2 - N + 1\right) \times 1$ vector. Here, $\mathbf{A}$ is a matrix that describes the spanning set of the intensity patterns; each column vector that composes $\mathbf{A}$ corresponds to the interference fringe of light from two distinct antennas (except for the exceptional case of $\mathbf{c}$ which corresponds to the intensity pattern of light from a single antenna). It is noteworthy that $\mathbf{A}$ is determined solely by the mode of a single antenna $u(x)$ and the position of the antennas x_n ($n = 1, 2, \ldots, N$). On the other hand, $\mathbf{q}$ is a vector that describes the complex amplitude of each interference fringes, which varies depending on the relative phase $\Delta\phi_{n,n'}$ between each antennas.

When the OPA is driven sequentially by K different sets of phase conditions $(\phi_1, \phi_2, \ldots, \phi_N)_k$ ($k = 1, 2, \ldots, K$), $\mathbf{q}$ defined by Eq. (4.15) changes, which we write as $\mathbf{q}_k$. Therefore, if we define an $(N^2 - N + 1) \times K$ matrix $\mathbf{Q} \equiv [\mathbf{q}_1, \mathbf{q}_2, \ldots, \mathbf{q}_K]$, the illumination matrix $\mathbf{I}$ is expressed as

$$\mathbf{I} = \mathbf{Q}^{\mathrm{T}}\mathbf{A}^{\mathrm{T}}. \tag{4.16}$$

We should stress again that $\mathbf{Q}$ is a matrix that describes the complex amplitudes of the vectors constituting the spanning set, i.e., the interference fringes, and depends only on the driving conditions of the phase shifters. On the other hand, $\mathbf{A}$ is a matrix that describes the spanning set and is determined by the antenna locations x_n ($n = 1, 2, \ldots, N$). If we set K and P to be sufficiently large, $\mathrm{rank}(\mathbf{I})$ would be limited to $N^2 - N + 1$ by the matrix sizes of $\mathbf{A}$ and $\mathbf{Q}$. Since we have not assumed any specific array layout, we can conclude that $N^2 - N + 1$ is the theoretical upper limit of $\mathrm{rank}(\mathbf{I})$ for SSPI using an OPA with N antennas in general.

2.2 Case 1: UOPA

We first consider the case of using an UOPA, where N antennas are located on a uniformly pitched array. The location x_n of the antennas can be defined to be

$$x_n \equiv nd \quad (n = 1, 2, ..., N), \tag{4.17}$$

where d is the spacing between adjacent antennas. In such a case, we easily notice that $\mathbf{a}_{n,n'}$ are no longer mutually distinct; since $x_{n+\eta} - x_n = \eta d$ (η is a positive integer), we can derive from Eqs. (4.9) and (4.17) that $\mathbf{a}_{1,1+\eta} = \mathbf{a}_{2,2+\eta} = ... = \mathbf{a}_{N-\eta,N}$ and $\mathbf{a}_{1+\eta,1} = \mathbf{a}_{2+\eta,2} = ... = \mathbf{a}_{N,N-\eta}$. Therefore, matrix $\mathbf{A}$ is obviously not full rank. Out of $N^2 - N + 1$ column vectors that construct $\mathbf{A}$, only the following $2N - 1$ are distinct (and at the same time, independent): $\mathbf{c}$, $\mathbf{a}_{1,2}$, $\mathbf{a}_{1,3}$, ..., $\mathbf{a}_{1,N}$, $\mathbf{a}_{2,1}$, $\mathbf{a}_{3,1}$, ..., and $\mathbf{a}_{N,1}$.

Therefore, Eq. (4.13) can be described using reduced-size matrices as

$$\mathbf{i} = \mathbf{B}\mathbf{r}, \tag{4.18}$$

where

$$\mathbf{B} \equiv \begin{bmatrix} \mathbf{c} & \mathbf{a}_{1,2} & \mathbf{a}_{1,3} & \dots & \mathbf{a}_{1,N} & \mathbf{a}_{2,1} & \mathbf{a}_{3,1} & \dots & \mathbf{a}_{N,1} \end{bmatrix} \tag{4.19}$$

is a $P \times (2N - 1)$ matrix and

$$\mathbf{r} \equiv \begin{bmatrix} N \\ \sum_{n=1}^{N-1} \exp\left(\mathrm{i}\Delta\phi_{n,n+1}\right) \\ \sum_{n=1}^{N-2} \exp\left(\mathrm{i}\Delta\phi_{n,n+2}\right) \\ \vdots \\ \exp\left(\mathrm{i}\Delta\phi_{1,N}\right) \\ \sum_{n=1}^{N-1} \exp\left(\mathrm{i}\Delta\phi_{n+1,n}\right) \\ \sum_{n=1}^{N-2} \exp\left(\mathrm{i}\Delta\phi_{n+2,n}\right) \\ \vdots \\ \exp\left(\mathrm{i}\Delta\phi_{N,1}\right) \end{bmatrix} \tag{4.20}$$

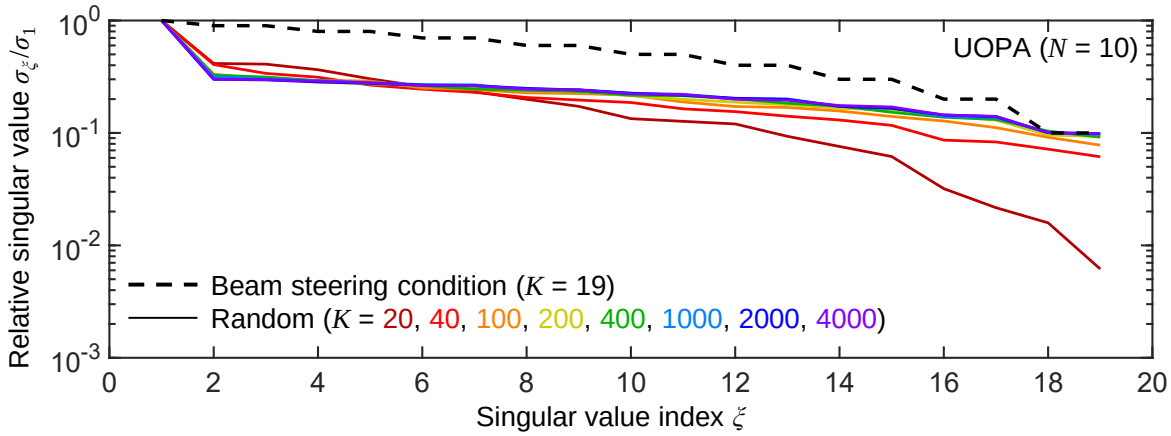

Fig. 4.2: Relative singular value distribution of $\mathbf{R}$ calculated for UOPA with $N = 10$. Solid lines show the cases when the phase shifters are randomly driven, while K is varied from 20 to 4000. The dashed line shows the case when the phase shifters are driven in a beam-steering condition.

is a $(2N-1)\times 1$ vector. Instead of Eq. (4.16), $\mathbf{I}$ can then be written as

$$\mathbf{I} = \mathbf{R}^{\mathrm{T}}\mathbf{B}^{\mathrm{T}}. \tag{4.21}$$

Here, we define $\mathbf{R} \equiv [\mathbf{r}_1, \mathbf{r}_2, ..., \mathbf{r}_K]$, where $\mathbf{r}_k$ denotes $\mathbf{r}$ in the k-th measurement.

For the sake of simplicity, we assume that each antenna can be approximated as a point light source, i.e., $u(x) = \delta(x)$. In such a case, $\mathbf{c}$, $\mathbf{a}_{1,1+\eta}$, and $\mathbf{a}_{1+\eta,1}$ $(\eta = 1, 2, ..., N-1)$ are orthogonal. Thus, $\mathrm{rank}(\mathbf{B}) = 2N-1$, limited by the matrix size. Moreover, their Euclidean norm are equal, such that

$$\mathbf{c}^\dagger\mathbf{c} = \mathbf{a}^\dagger_{1,1+\eta}\mathbf{a}_{1,1+\eta} = \mathbf{a}^\dagger_{1+\eta,1}\mathbf{a}_{1+\eta,1} \quad (\eta = 1, 2, ..., N-1). \tag{4.22}$$

As a result, $\mathbf{B}$ has identical $2N-1$ singular values, so that the singular value distribution of $\mathbf{I}$ is determined solely by that of $\mathbf{R}$.

Figure 4.2 shows the relative singular value distribution of $\mathbf{R}$ for a test case of UOPA with $N = 10$. Here, σ_ξ denotes the ξ-th singular value. The solid lines show the result when the phase shifters are driven randomly for various values of K. We can observe that by increasing K, the singular value distribution converges to a single smooth curve. As a comparison, the dashed line shows the case for beam steering, where the phase shifters are driven to form an equal phase plane at the OPA output. Here, $\mathrm{rank}(\mathbf{R}) = 2N-1 = 19$ is obtained for all cases, which means that the matrix-size-limited number of resolvable points is obtained. This

property is numerically confirmed at larger N. Moreover, we can analytically derive

$$\frac{\sigma_\xi}{\sigma_1} = \begin{cases} \dfrac{N - \frac{\xi-1}{2}}{N} & (\text{when } \xi = 2\zeta - 1, \text{where } \zeta = 1, 2, ..., N) \\ \dfrac{N - \frac{\xi}{2}}{N} & (\text{when } \xi = 2\zeta, \text{where } \zeta = 1, 2, ..., N-1) \end{cases} \tag{4.23}$$

for the beam-steering condition (derivation of Eq. (4.23) is given in Appendix A), and thus $\mathrm{rank}(\mathbf{R}) = 2N - 1$[*2]. For the randomly driven cases, we can understand that $\mathrm{rank}(\mathbf{R})$ cannot exceed $2N-1$ since this is the upper limit determined by the size of $\mathbf{R}$, and converges to $2N-1$ if K is sufficiently large[*3].

From Fig. 4.2, we can observe that the relative singular values σ_ξ/σ_1 at $1 < \xi < 2N-2$ are smaller for the randomly driven case compared with those of the beam steering conditions. This property can be understood from Eq. (4.20). In the case of beam steering, the phases are set such that

$$\Delta\phi_{n,n+\eta} = \eta\beta_0 d\theta_0 \quad (\eta = 1, 2, ..., N-1), \tag{4.24}$$

where θ_0 is the steered angle. Therefore, the summation terms in Eq. (4.20) add up constructively in phase on the complex plane, so that

$$\sum_{n=1}^{N-\eta} \exp\left(\mathrm{i}\Delta\phi_{n,n+\eta}\right) = (N-\eta)\exp\left(\mathrm{i}\Delta\phi_{1,1+\eta}\right) \quad (\eta = 1, 2, ..., N-1). \tag{4.25}$$

As a result, amplitudes of each interference fringes given by Eq. (4.9) can be maximized. Since the singular values of the matrix describe the magnitudes of the respective basis vectors, σ_ξ of $\mathbf{I}$ can be maximized by driving the phase shifters under the beam-steering condition. In contrast, when the phase shifters are randomly driven, the summation terms do not necessarily add up in phase but may cancel out destructively, depending on the phase conditions. As a result, the amplitudes of each interference fringes becomes smaller, and thus the singular values at $1 < \xi < 2N-2$ become smaller compared to the beam-steering case. We should note that the largest singular value σ_1 of $\mathbf{I}$ corresponds to the zero-spatial-frequency component of the intensity profile, that is, $N\mathbf{c}$. Its magnitude describes the average optical intensity inside the field-of-view (FOV) and is independent on the driving condition. Therefore, the

[*2] One important message here is that as long as we want to resolve N points, $\kappa(\mathbf{I}) \simeq 1/2$ (it does not get worse when N vary). This is in contrast to the case of NROPA, where $\kappa(\mathbf{I}) = 1/N$ (getting worse with N) regardless of the number of resolvable points we set.

[*3] This conclusion that $2N-1$ resolvable poitns can be obtained for a N-element totally agrees with that of the number of resolvable angles for the DOA problem [193]. This corresponds to the fact that the mathematical structure of the DOA problem and SSPI problem is very similar.

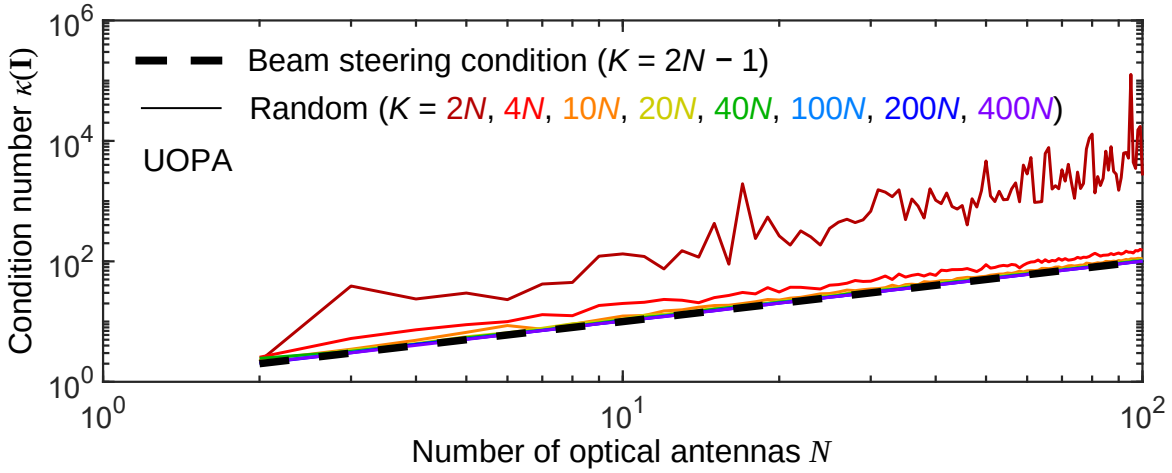

Fig. 4.3: N dependency of $\kappa(\mathbf{I})$ when UOPA is employed under different driving conditions: when the phase shifters are driven randomly with different values of K (solid) and when they are driven under a beam-steering condition (broken).

relative singular values σ_ξ/σ_1 for the randomly driven cases are smaller compared to the beam-steering condition.

On the other hand, the condition number of the matrix $\mathbf{I}$ [194], which is described as

$$\kappa(\mathbf{I}) = \kappa(\mathbf{R}) \equiv \frac{\sigma_1}{\sigma_{\mathrm{rank}(\mathbf{R})}} = \frac{\sigma_1}{\sigma_{2N-1}}, \tag{4.26}$$

reduces and converges to that of the beam-steering case as K increases (here, we assume truncating the singular values that are equal to zero to define $\kappa(\mathbf{I})$ [195]). This can be understood as the following. When K is sufficiently large, $\mathbf{r}_k$ $(k = 1, 2, ..., K)$ distributes almost uniformly within its range. As a result, the smallest singular value $\sigma_{\mathrm{rank}(\mathbf{R})} = \sigma_{2N-1}$ is determined by the magnitude of the interference fringe that has the smallest amplitude among all the interference fringes. Such interference fringes are $\mathbf{a}_{1,N}$ and $\mathbf{a}_{N,1}$ in Eq. (4.19), whose amplitudes are $\exp\left(\mathrm{i}\Delta\phi_{1,N}\right)$ and $\exp\left(\mathrm{i}\Delta\phi_{N,1}\right)$, respectively, as shown in Eq. (4.20). Since these terms do not contain summations unlike the other interference fringes, their magnitudes are constant regardless of the driving condition. As a result, $\kappa(\mathbf{I})$ for the beam-steering and the randomly driven cases are identical. Generally speaking, smaller $\kappa(\mathbf{I})$ implies that the matrix $\mathbf{I}$ is well-conditioned, so that the image can be retrieved at a higher accuracy through Eq. (4.4) even at the presence of receiver noise. We should also note that the required K to reach the convergence can be minimized by carefully selecting the driving conditions of OPA [84].

We then investigate how the condition number $\kappa(\mathbf{I})$ depends on N and K. The solid lines in Fig. 4.3 shows $\kappa(\mathbf{I})$ as a function of N, while K is varied from $2N$ to $400N$. The dashed line shows the case of beam steering. We see that when K is large enough, $\kappa(\mathbf{I})$ for the

randomly driven case converges to that of the beam-steering case. In these converged cases, $\kappa(\mathbf{I}) = N$, which is in agreement with Eq. (4.23). However, as we have shown in Fig. 4.2, the relative singular values σ_ξ/σ_1 $(1 < \xi < 2N-1)$ are smaller in the randomly driven cases than those under the beam-steering condition. Therefore, although $\kappa(\mathbf{I})$ is identical in both cases, the performance of the randomly driving condition would be inferior to the beam-steering condition in a noisy system, where the singular values need to be truncated at $\xi < 2N-1$ [195].

We should also note that Eq. (4.23) resembles the distribution of the autocorrelation function of the array layout function, which we have defined as

$$\mathscr{R}_{aa}(\Delta x) \equiv \sum_{n=1}^{N}\sum_{n'=1}^{N} \delta(\Delta x - \Delta x_{n,n'}). \tag{4.27}$$

Here, Δx denotes the displacement of antenna array along the x axis. Figure 4.4(a) shows $\mathscr{R}(\Delta x)$ of UOPA with $N = 10$. When a uniformly spaced array is displaced by $\pm\eta d$ ($\eta = 0, 1, 2, ..., N-1$), $N-\eta$ elements out of N overlap with the array before the displacement. Thus, $\mathscr{R}(\Delta x)$ exhibits a triangular distribution. By normalizing and rearranging the autocorrelation peaks in the order of magnitude, we obtain Fig. 4.4(b), which agrees with the relative singular value distribution of $\mathbf{R}$ for the case of beam steering, given by Eq. (4.23). This agreement can be interpreted as the following. The magnitude of $\mathscr{R}_{aa}(\Delta x)$ corresponds to the number of pairs of antennas that are separated by Δx. Since the displacement Δx between a pair of antennas determines the spatial frequency of the interference fringe generated from the pair of antennas, all the pairs that are separated by Δx generate interference fringes, having the same spatial frequency. In a beam-steering condition, these interference fringes from respective pairs add up constructively in phase. Therefore, the magnitude of each interference fringe becomes proportional to the number of pairs of antennas that are separated by the corresponding distance. As a result, the magnitudes of autocorrelation peaks correspond to those of the interference fringes, which are directly related to the singular values.

2.3 Case 2: NROPA

Next, we consider the case of using an NROPA, where N antennas are located on a 1D NRA, i.e., the Golomb ruler [164]. The location x_n of the antennas can then be written as

$$x_n \equiv G_n d \quad (n = 1, 2, ..., N), \tag{4.28}$$

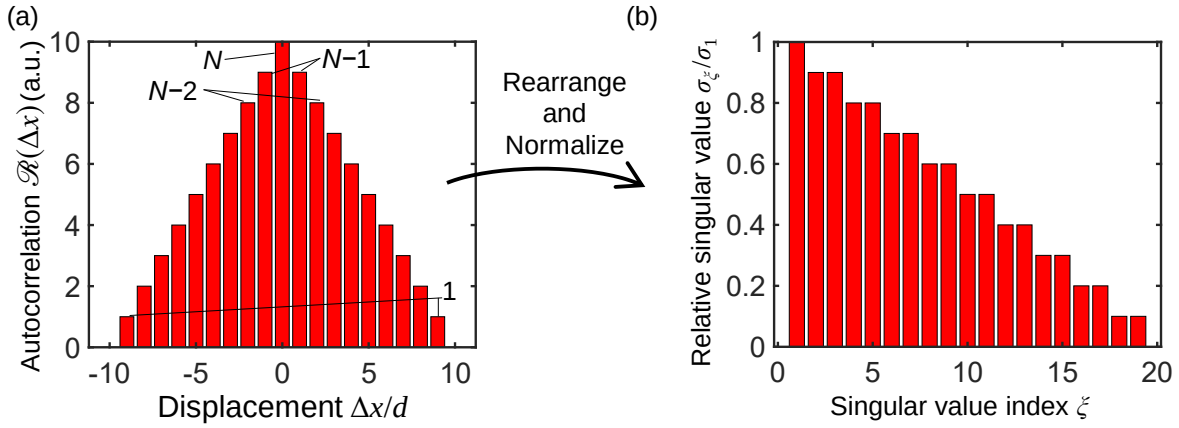

Fig. 4.4: (a) $\mathscr{R}(\Delta x)$ of a uniformly spaced array ($N = 10$). (b) Singular value distribution of $\mathbf{R}$ for the case of beam steering ($N = 10$), which can be obtained by normalizing and rearranging (a).

where d is the unit spacing and G_n $(n = 1, 2, ..., N)$ are the integer marks of the N-th-order Golomb ruler. From the definition of the Golomb ruler, G_n satisfy

$$\delta_{\Delta G_{m,n},\Delta G_{m',n'}} = \delta_{m,m'}\delta_{n,n'} + \delta_{m,n}\delta_{m',n'}\left(1 - \delta_{m,m'}\delta_{n,n'}\right) \tag{4.29}$$

where $\Delta G_{m,n} \equiv G_m - G_n$ and $\delta_{m,n}$ is the Kronecker delta. Without loss of generality, we assume $0 = G_1 < G_2 < \cdots < G_N$. Therefore, $\mathbf{c}$ and $\mathbf{a}_{n,n'}$ $(n, n' = 1, 2, ..., N, n \neq n')$ defined in Eqs. (4.9) and (4.10) are linearly independent. If we assume the optical antennas to be point light sources, $\mathbf{c}$ and $\mathbf{a}_{n,n'}$ are mutually orthogonal. In addition, the Eucledian norm of $\mathbf{c}$ and $\mathbf{a}_{n,n'}$ are identical so that Eq. (4.22) is satisfied as for the case of UOPA. In such a case, $\mathbf{A}$ defined by Eq. (4.14) has identical $N^2 - N + 1$ singular values, and the singular value distribution of $\mathbf{I}$ will be determined by that of $\mathbf{Q}$, according to Eq. (4.16).

Figure 4.5 shows the relative singular value distribution of $\mathbf{Q}$ calculated for an NROPA with $N = 10$. Once again, we compare the cases where the phase shifters are randomly driven for different K (solid lines) with the case of beam-steering condition (dashed line). In the latter case, the phase shifters are set to satisfy

$$\Delta\phi_{n,n'} = \Delta G_{n,n'}\beta_0 d\theta_0, \tag{4.30}$$

where θ_0 is the steering angle. We can see that for all cases, $\mathrm{rank}(\mathbf{I}) = \mathrm{rank}(\mathbf{Q}) = N^2 - N + 1 = 91$, limited only by the matrix sizes of $\mathbf{A}$ and $\mathbf{Q}$. This quadratic scaling is in clear contrast to the case of UOPA, shown in Fig. 4.2. Moreover, we should recall that $N^2 - N + 1$ is the theoretical upper limit of $\mathrm{rank}(\mathbf{I})$ for any OPA configuration, as discussed previously. Figure

4.5 clearly shows that the theoretically maximum spatial resolution can be achieved by using an NROPA.

From Fig. 4.5, we can confirm that the condition number $\kappa(\mathbf{I})(=\kappa(\mathbf{Q}))$ decreases as we increase K for the randomly driven cases. Moreover, the singular values become more and more uniform and converge to the beam-steering case, where the relative singular values are written as

$$\frac{\sigma_\xi}{\sigma_1} = \begin{cases} 1 & (\xi = 1) \\ \dfrac{1}{N} & (\xi > 1) \end{cases}. \tag{4.31}$$

The analytical derivation of Eq. (4.31) is given in Appendix B. Note that such convergence of the relative singular value distribution to the case of beam steering is not observed in Fig. 4.2 for the UOPA case, where the relative singular value distribution for the randomly driving cases are always incongruous with that of the beam steering case. This can be understood as the following. Unlike the UOPA case where the summations expressed by Eq. (4.25) are included in $\mathbf{R}$, all $N^2 - N + 1$ interference fringes in $\mathbf{A}$ described by Eq. (4.14) are orthogonal for the case of NROPA, so that the complex amplitudes $\exp\left(\mathrm{i}\Delta\phi_{n,n'}\right)$ of the respective intensity fringes in $\mathbf{Q}$ do not add up or cancel out. As a result, the magnitudes of the interference fringes are constant regardless of the driving condition. Thus, the relative singular values for the randomly driving case can be as large as that for the case of the beam steering. On the other hand, we notice that the relative singular values are smaller compared to the case of UOPA. In NROPA, each interference fringe is generated only from a single pair of antennas, whereas several pairs of antennas generate interference fringes with the same spatial frequency for the case of UOPA, which may add up constructively in phase depending on the driving condition. As a result, the magnitude of each interference fringe is generally smaller for the case of NROPA, while the number of different-frequency interference fringes increases drastically at $O(N^2)$ owing to its non-redundancy.

The N dependency of $\kappa(\mathbf{I})$ $(=\kappa(\mathbf{Q}))$ for NROPA is shown in Fig. 4.6. Once again, $\kappa(\mathbf{I})$ converges to the case of beam steering (dashed line) at large K. In such a case, $\kappa(\mathbf{I}) = N$, which is identical to the case of UOPA, and is in agreement with Eq. (4.31). It is noteworthy that although the number of resolvable points is enhanced drastically from $\mathrm{rank}(\mathbf{I}) = \mathrm{rank}(\mathbf{R}) = 2N - 1$ for the case of UOPA to $\mathrm{rank}(\mathbf{I}) = \mathrm{rank}(\mathbf{Q}) = N^2 - N + 1$ in case of NROPA, $\kappa(\mathbf{I})$ is unchanged. In other words, significantly higher spatial resolution can be obtained by using the NROPA, as long as the noise level is sufficiently low so that the required truncation level [195] is not strict.

We should note again that similar to the case of UOPA, the singular value distribution described by Eq. (4.31) is consistent with $\mathscr{R}(\Delta x)$, defined by Eq. (4.27). Figure 4.7(a) shows $\mathscr{R}(\Delta x)$ for the NRA (Golomb ruler) with $N = 10$. When a NRA with the positions defined by

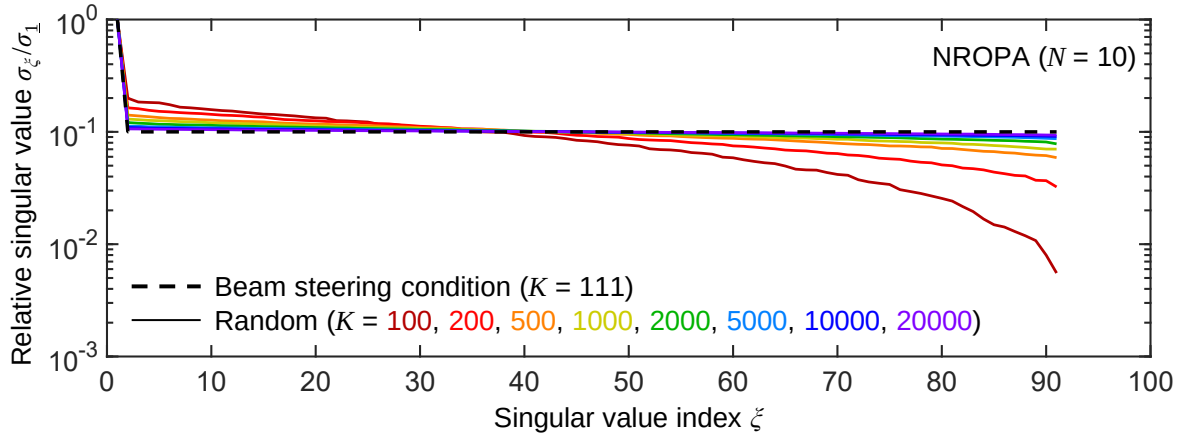

Fig. 4.5: Relative singular value distribution of $\mathbf{Q}$ calculated for NROPA with $N = 10$. Solid lines show the cases when the phase shifters are randomly driven, while K is varied from 100 to 20000. The dashed line shows the case when the phase shifters are driven under a beam-steering condition.

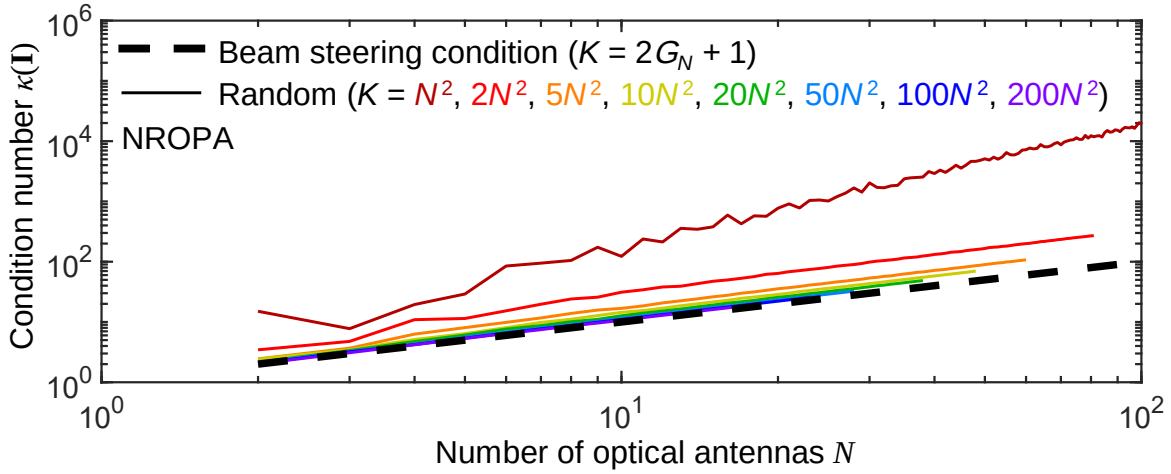

Fig. 4.6: N dependency of $\kappa(\mathbf{I})$ when NROPA is employed under different conditions: when the phase shifters are driven randomly with different values of K (solid) and when they are driven to satisfy the beam-steering condition (broken).

Eq. (4.28) is displaced by $\Delta G_{n,n'} d$, only one out of $N(N-1)/2$ pairs of marks overlaps due to the property of the Golomb ruler. The only exception is the case of $n = n'$ (i.e, when we do not displace the array at all), where all N marks overlap with themselves. As a result, $\mathscr{R}(\Delta x)$ becomes a flat and broadly distributed function with a sharp peak at the center as shown in Fig. 4.7(a). By normalizing the largest value to 1 and rearranging all nonzero components in the order of their magnitudes, we obtain Fig. 4.7(b), which is in agreement with the singular value distribution shown in Fig. 4.5.

Note that there are some missing components in $\mathscr{R}(\Delta x)$, i.e., $\mathscr{R}(\Delta x) = 0$ at some integer

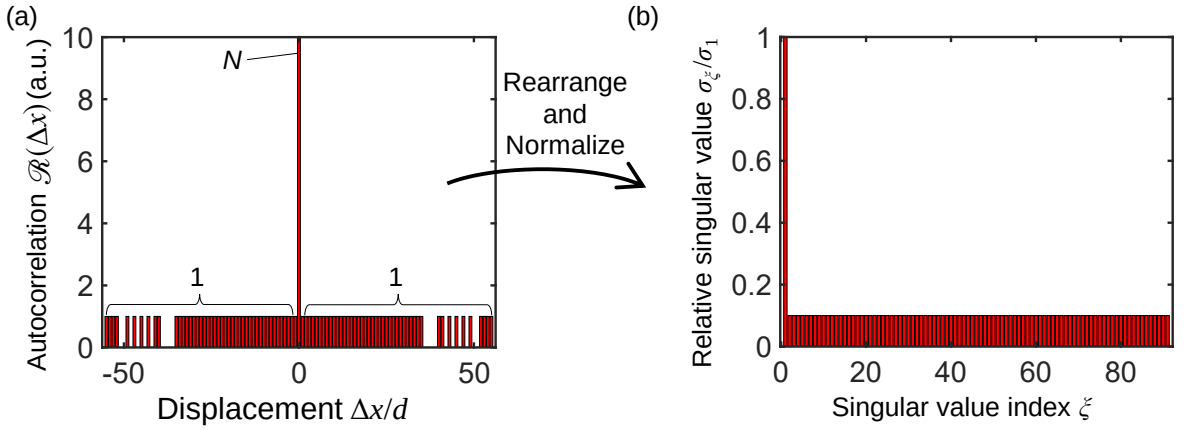

Fig. 4.7: (a) $\mathscr{R}(\Delta x)$ of a Golomb ruler ($N = 10$). (b) Singular value distribution of $\mathbf{Q}$ for the beam steering condition, which can be obtained by normalizing and rearranging $\mathscr{R}(\Delta x)$.

values of $\Delta x/d$ in Fig. 4.7(a). This reflects the fact that no perfect Golomb ruler exists when $N > 4$. Although all $\Delta G_{n,n'}$ are distinct, we cannot sample all integers m within $|m| \leq G_N$. As a result, there are some missing spatial frequency components in $\mathbf{A}$ described by Eq. (4.14) to generate $\mathbf{I}$. Again, here, we use the optimal Golomb ruler (for $N < 28$) or the quasi-optimal Golomb ruler (for $N > 27$), which are the shortest Golomb ruler for a given N (while the optimal Golomb rulers are proven to be shortest, quasi-optimal Golomb rulers have not yet been proven to be truly optimal). Such optimal or quasi-optimal Golomb rulers minimizes the number of missing spatial frequency component within the range of $|\Delta x/d| \leq G_N$. If necessary, we could add a few additional redundant elements to the array to enable sampling of all the spatial frequency components within the range of $|\Delta x/d| \leq G_N$ [177], which is known not to significantly degrade the scaling rule.

3. Imaging results

Finally, we numerically perform SSPI using UOPA and NROPA and compare the qualities of reconstructed images. We consider a test case of $N = 16$ and assume, for simplicity, the optical antennas to be point light sources.

Figure 4.8 shows examples of intensity profile of speckle patterns generated from UOPA (blue dashed) and NROPA (red solid). Note that we only plot the FFP within the FOV, which is expressed as FOV $\equiv 2\pi/\beta_0 d$. We can clearly observe in Fig. 4.8 that the speckles generated by NROPA has much narrower features compared to that generated by UOPA, although $N = 16$ for both cases. This directly allows finer features of the target to be retrieved through SSPI by using NROPA, since only the spatial frequency components included in the speckles can be sampled from the target through Eq. (4.3). To quantitatively examine this difference, we plot

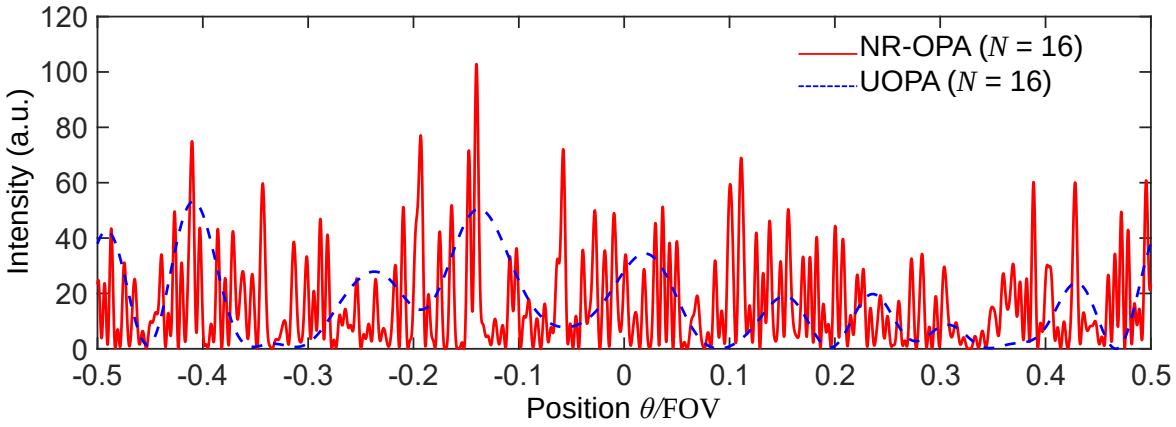

Fig. 4.8: Examples of speckle intensity patterns generated from a UOPA (blue dashed) and an NROPA (red solid) with $N = 16$.

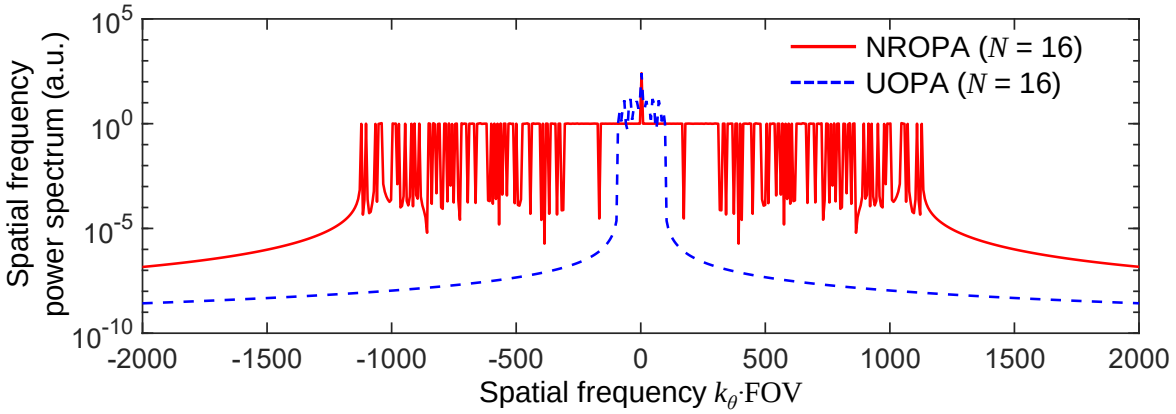

Fig. 4.9: Spatial frequency power spectra of the speckles (shown in Fig. 4.8), generated from UOPA (blue dashed) and NROPA (red solid) with $N = 16$.

in Fig. 4.9 the spatial frequency spectra of the intensity patterns shown in Fig. 4.8. Indeed, we can see that it covers a much broader spatial frequency range for the case of NROPA (red-solid), compared to the case of UOPA (blue-dashed).

Figure 4.10 shows the singular values of $\mathbf{I}$ generated from NROPA (red solid) and UOPA (blue dashed) for $N = 16$ and $K = 1000$. In agreement with the discussions in Section 3, the singular value drops rapidly to 0 at $\xi > 2N - 1 = 31$ for the case of UOPA and at $\xi > N^2 - N + 1 = 241$ for the case of NROPA. Thus, far larger number of resolvable points should be attained by using NROPA instead of UOPA.

We then demonstrate SSPI assuming a 1D slit pattern as a target. The smallest feature size of the target is set to be $\mathrm{FOV}/200 \simeq 1/N^2$. Figure 4.11 shows the results when we use UOPA [Fig. 4.11(a)] and NROPA [Fig. 4.11(b)] with $N = 16$. The target is shown by black broken

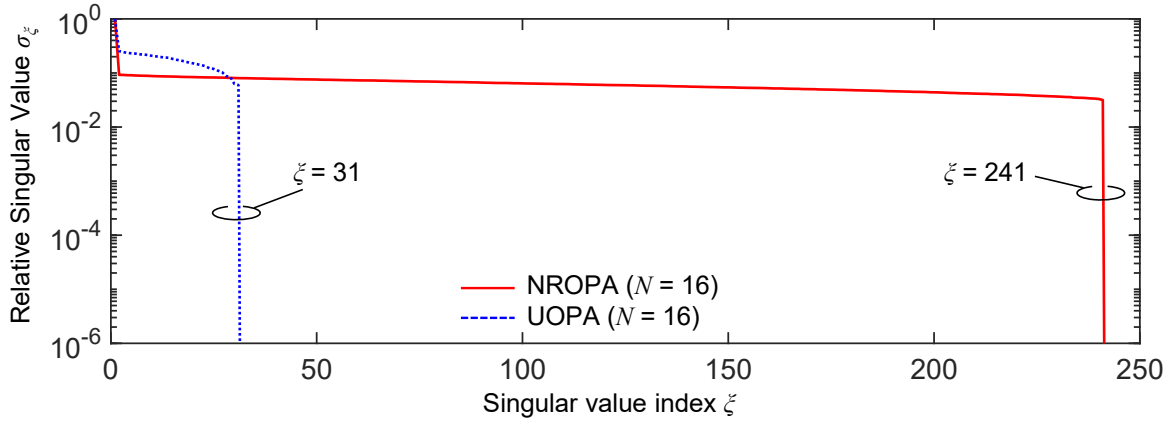

Fig. 4.10: Singular value distribution of $\mathbf{I}$ for NROPA (red solid) and UOPA (blue dashed). We assume $N = 16$ and $K = 1000$.

lines. We set $K = 1000$. and assume two cases with (blue dotted) and without (red solid) the receiver noise $\Delta\mathbf{S}$. The receiver signal-to-noise ratio (SNR) $|\mathbf{S}|/|\Delta\mathbf{S}|$ is set to be 20 dB. In the case of UOPA, while large features are successfully retrieved, smaller features are not reconstructed. This is because the feature size is much smaller than the feature size of the speckles. In contrast, when we use NROPA, even the smallest features of the target can be retrieved. This can be attributed to the high-spatial frequency components included in the speckles generated from NROPA, as shown in Fig. 4.8 and Fig. 4.9.

Figure 4.12 shows the spatial frequency power spectra of the actual target (black broken) and the reconstructed images for NROPA (red solid) and UOPA (blue dotted) without the receiver noise. We can confirm that only a limited range of the spatial frequency is reconstructed for the case of UOPA, whereas broader range of spatial frequency spectrum is retrieved by using NROPA. The noisy spectrum at the higher frequency range for the NROPA case is due to the missing spatial frequency component of the Golomb ruler as discussed in Section 3.3. We should note again that such missing components in the spatial frequency spectrum can be eliminated by adding a few redundant elements to the NRA to form a minimum redundancy array (MRA) [177].

Finally, Fig. 4.13 shows the dependence of the image qualities on K. We plot the peak signal-to-noise ratio (PSNR) of the reconstructed image for the cases of UOPA and NROPA with and without the receiver noise (SNR = 20 dB). We can see that when there is no noise, the PSNR is constant when $K \geq 2N$ for UOPA and $K \geq N^2 - N + 1$ for NROPA. This is because when K is large enough, the number of independent information included in $\mathbf{I}$ is constant. On the other hand, when the receiver noise exists, PSNR is no longer constant but gradually converges to the noiseless case as K increases. This is a natural trend since the statistical noise reduces as the number of measurement K increases. In addition, $\kappa(\mathbf{I})$ decreases as K increases

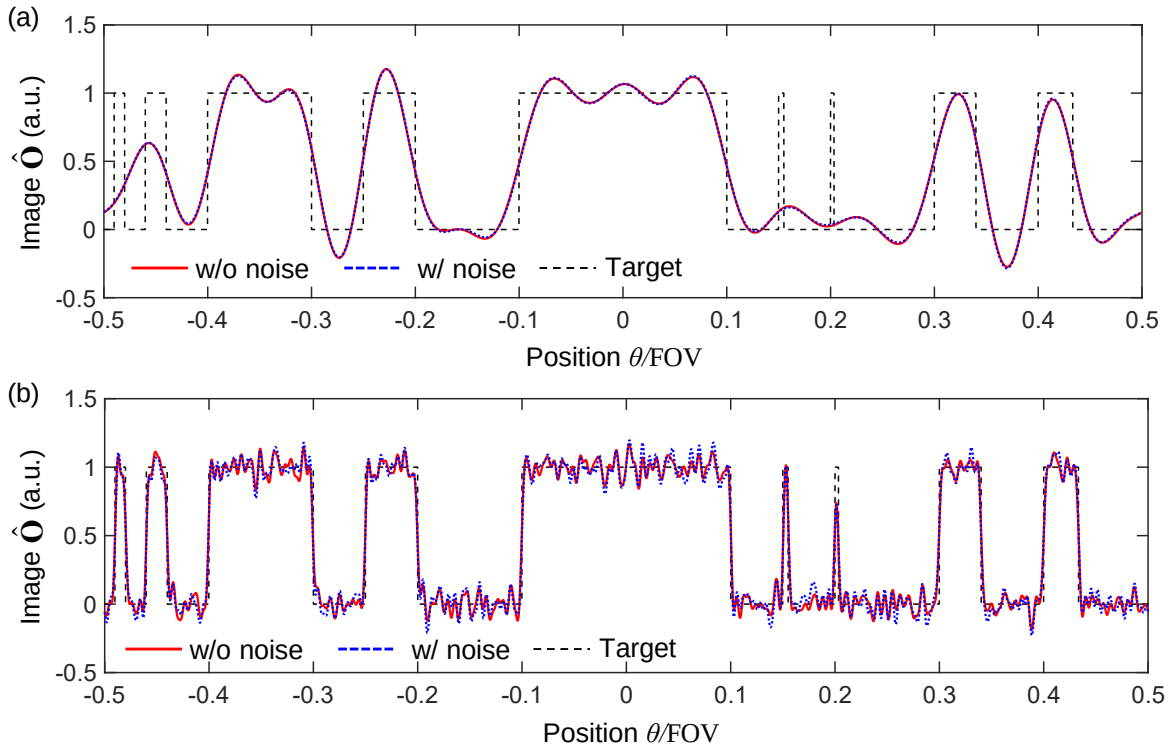

Fig. 4.11: Reconstructed images of a 1D slit pattern (black broken) for the cases without noise (red solid) and with noise (blue dotted, SNR = 20 dB) using (a) UOPA and (b) NROPA. We assume $N = 16$ and $K = 1000$.

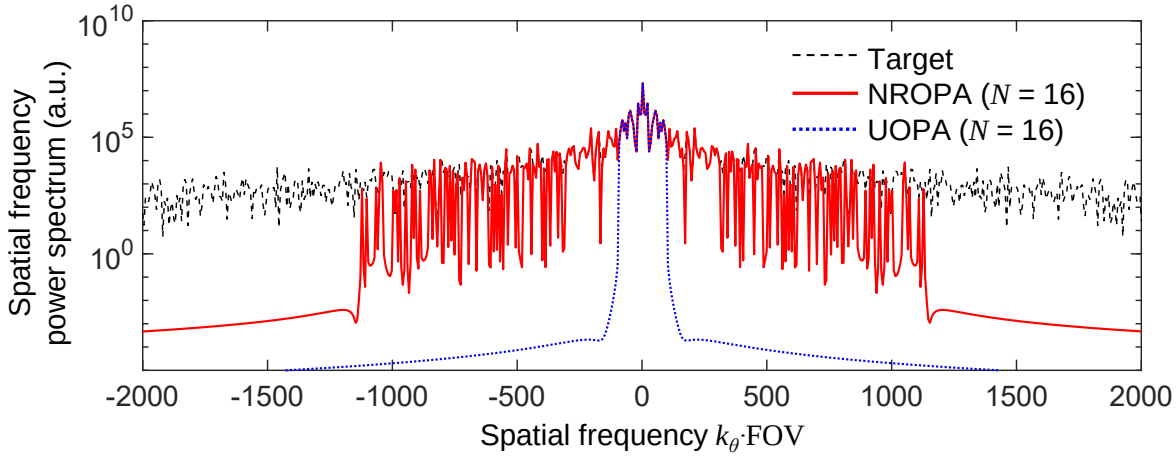

Fig. 4.12: Spatial frequency power spectra of the target (black dotted) and the reconstructed images obtained by NROPA (red solid) and UOPA (blue dotted) without receiver noise. We assume $N = 16$ and $K = 1000$.

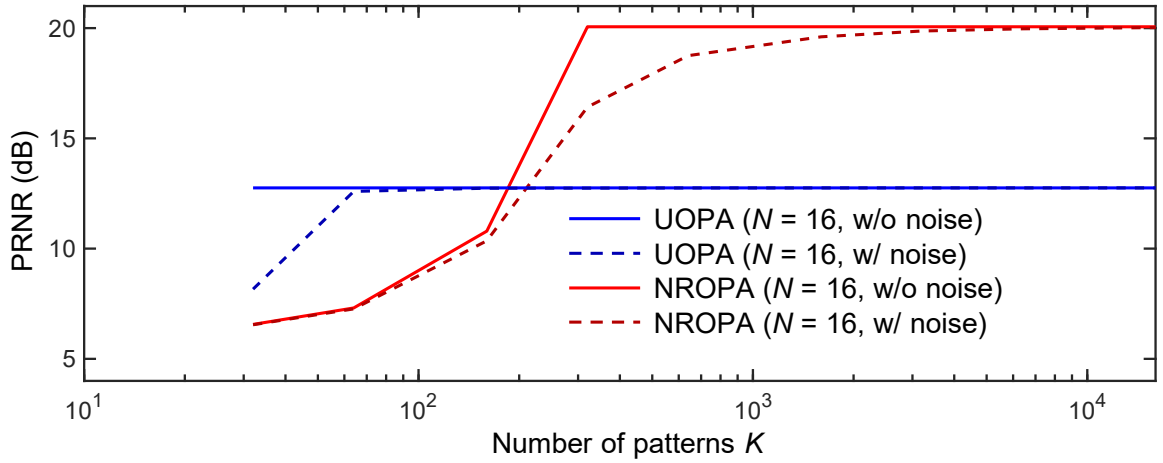

Fig. 4.13: K dependency of the PSNR of the reconstructed image.

as shown in Fig. 4.13, and $\kappa(\mathbf{I})$ describes how largely the noise will impact the reconstruction result [194]. When K is large enough, the PSNR for the NROPA-based SSPI is much better than that of UOPA-based SSPI. As we have discussed, this is because much smaller features of the target can be reconstructed by using NROPA, thanks to the broad spatial frequency spectrum information included in $\mathbf{I}$.

4. Summary

We have theoretically and numerically investigated the SSPI schemes using UOPA and NROPA with N phase shifters. Through theoretical analysis, we first derived the theoretical limit of the resolvable points for each case. While only $2N-1$ resolvable points can be attained by UOPA, the number of resolvable points can be as large as N^2-N+1 using NROPA. This value can be understood as the number of independent interference fringes that is generated from each pair of optical antennas. The spatial frequency of the interference fringes is determined by the displacement $\Delta x_{n,n'}$ between the antenna positions, and, thus, judicious engineering of the autocorrelation function $\mathscr{R}(\Delta x)$ is critical in achieving the highest spatial resolution with a limited N.

We have then numerically analyzed the singular values of the illumination matrix $\mathbf{I}$ for the respective cases of SSPI, and compared them with the beam-steering cases. When UOPA is employed, there is always a penalty in driving the phase shifters randomly compared with the beam-steering condition. This is because several pairs of antennas generate interference fringes having the same spatial frequency. As a result, the contributions from different pairs of antennas add up constructively in phase under the beam-steering condition, whereas they may cancel out destructively in the randomly driven case. In contrast, when NROPA is

employed, there is no penalty in driving the phase shifters randomly as long as the number of illuminations K is sufficiently large. This is because different pairs of optical antennas generate interference fringes with distinct spatial frequencies, and thus the magnitude of each spatial frequency component is constant, irrespective of the driving condition. The condition number $\kappa(\mathbf{I})$ converges to N at sufficiently large K, which is identical to that for the beam-steering condition.

Finally, we numerically performed SSPI for both cases and demonstrated the feasibility and effectiveness of using NROPA for SSPI instead of UOPA. Owing to the higher-frequency component of the illumination patterns generated by NROPA, significantly finer features can be reconstructed through NROPA-based SSPI, which can never be retrieved by UOPA. By the NROPA-based SSPI, therefore, we can simultaneously enjoy the minimal driving complexity of the SSPI scheme and the high spatial resolution of NROPA. It should be an attractive method in realizing low-complexity and low-cost optical sensing systems using OPAs.

Appendix

4.A Derivation of Eq. (4.23)

We consider the singular value decomposition (SVD) of $\mathbf{I}$ for the case of beam steering. Assuming that the beam is steered to $2N-1$ equally spaced angles within the FOV, the phase conditions for the k-th steering condition ($k = 1, 2, ..., 2N-1$) can be written as

$$\phi_{n;k} = \frac{2\pi nk}{2N-1}. \tag{4.32}$$

In such a case, the summation terms in Eq. (4.20) are expressed as

$$\begin{aligned}\sum_{n=1}^{N-\eta} \exp\left(\mathrm{i}\Delta\phi_{n,n+\eta;k}\right) &= (N-\eta)\exp\left[\mathrm{i}\left(\frac{2\pi\eta k}{2N-1}.\right)\right] \\ &\equiv (N-\eta)\,\omega^{\eta k} \quad (\eta = 1, 2, ..., (N-1))\end{aligned} \tag{4.33}$$

and

$$\begin{aligned}\sum_{n=1}^{N-\eta} \exp\left(\mathrm{i}\Delta\phi_{n+\eta,n;k}\right) &= (N-\eta)\exp\left[-\mathrm{i}\left(\frac{2\pi\eta k}{2N-1}.\right)\right] \quad (\eta = 1, 2, ..., (N-1)) \\ &\equiv (N-\eta)\,\omega^{-\eta k} \quad (\eta = 1, 2, ..., (N-1)),\end{aligned} \tag{4.34}$$

where

$$\omega \equiv \exp\left[\mathrm{i}\left(\frac{2\pi}{2N-1}\right)\right] \tag{4.35}$$

and

$$\Delta\phi_{n,n';k} \equiv \phi_{n;k} - \phi_{n';k}. \tag{4.36}$$

Therefore,

$$\mathbf{r}_k = \begin{bmatrix} N\omega^0 \\ (N-1)\omega^k \\ (N-2)\omega^{2k} \\ \vdots \\ \omega^{Nk} \\ (N-1)\omega^{-k} \\ (N-2)\omega^{-2k} \\ \vdots \\ \omega^{-Nk} \end{bmatrix} = \mathbf{D}\mathbf{v}_k, \tag{4.37}$$

where

$$\mathbf{v}_k \equiv \sqrt{\frac{1}{2N-1}} \begin{bmatrix} \omega^0 \\ \omega^k \\ \omega^{2k} \\ \vdots \\ \omega^{Nk} \\ \omega^{-k} \\ \omega^{-2k} \\ \vdots \\ \omega^{-Nk} \end{bmatrix} \tag{4.38}$$

is a $(2N-1)\times 1$ unit vector, and

$$\begin{aligned}\mathbf{D} &\equiv \sqrt{2N-1}\,\mathrm{diag}(N, N-1, N-2, \cdots, 1, N-1, N-2, \cdots, 1) \\ &= \sqrt{2N-1}\begin{bmatrix} N & 0 & \dots & 0 \\ 0 & N-1 & \dots & 0 \\ \vdots & \vdots & \ddots & \vdots \\ 0 & 0 & \dots & 1 \end{bmatrix}\end{aligned} \tag{4.39}$$

is a $(2N-1)\times(2N-1)$ diagonal matrix.

R can then be written as

$$\mathbf{R} = \mathbf{DV} = \mathbf{1}_{(2N-1)\times(2N-1)}\mathbf{DV}, \tag{4.40}$$

where $\mathbf{V} \equiv [\mathbf{v}_1, \mathbf{v}_2, ..., \mathbf{v}_{2N-1}]$ and $\mathbf{1}_{(2N-1)\times(2N-1)}$ denotes the $(2N-1)\times(2N-1)$ unit matrix. We should note that **V** is a $(2N-1)$-point discrete Fourier transform (DFT) matrix (with a slight rearrangement in the order of the row vectors). Thus, **V** is unitary. Since **1** is obviously a unitary matrix as well and **D** is diagonal, Eq. (4.40) represents the SVD of **R**.Therefore, the singular values of **R** (in the order of magnitude) are

$$\sigma_\xi = \begin{cases} \sqrt{2N-1}\left(N - \dfrac{\xi-1}{2}\right) & (\text{when } \xi = 2\zeta - 1, \text{where } \zeta = 1, 2, ..., N) \\ \sqrt{2N-1}\left(N - \dfrac{\xi}{2}\right) & (\text{when } \xi = 2\zeta, \text{where } \zeta = 1, 2, ..., N-1) \end{cases}, \tag{4.41}$$

from which Eq. (4.23) can be derived.

4.B Derivation of Eq. (4.31)

We can derive Eq. (4.31) following a similar procedure as described in Appendix A. Here, we consider the case of steering the beam to $2G_N + 1$ equally spaced angles within the FOV. Note that we consider steering the beam to $2G_N + 1$ points instead of $N^2 - N + 1$ points in order to make the discussion consistent with that in Appendix A. The phase condition for the k-th steering condition can be written as

$$\phi_{n,k} = \frac{2\pi G_n k}{2G_N + 1}. \tag{4.42}$$

In such a case, $\mathbf{q}$ in Eq. (4.15) is written as

$$\mathbf{q} = \mathbf{H}\mathbf{w}_k, \tag{4.43}$$

where

$$\mathbf{w}_k \equiv \sqrt{\frac{1}{N^2-N+1}} \begin{bmatrix} 1 \\ \exp\left[\mathrm{i}\left(\frac{2\pi\Delta G_{1,2}k}{2G_N+1}\right)\right] \\ \exp\left[\mathrm{i}\left(\frac{2\pi\Delta G_{1,3}k}{2G_N+1}\right)\right] \\ \vdots \\ \exp\left[\mathrm{i}\left(\frac{2\pi\Delta G_{N,N-2}k}{2G_N+1}\right)\right] \\ \exp\left[\mathrm{i}\left(\frac{2\pi\Delta G_{N,N-1}k}{2G_N+1}\right)\right] \end{bmatrix} = \sqrt{\frac{1}{N^2-N+1}} \begin{bmatrix} \alpha^0 \\ \alpha^{\Delta G_{1,2}k} \\ \alpha^{\Delta G_{1,3}k} \\ \vdots \\ \alpha^{\Delta G_{N,N-2}k} \\ \alpha^{\Delta G_{N,N-1}k} \end{bmatrix} \tag{4.44}$$

is a $\left(N^2-N+1\right)\times 1$ unit vector,

$$\alpha \equiv \exp\left[\mathrm{i}\left(\frac{2\pi}{2G_N+1}\right)\right] \tag{4.45}$$

and

$$\mathbf{H} \equiv \sqrt{N^2-N+1}\mathrm{diag}(N,1,...,1) = \sqrt{N^2-N+1} \begin{bmatrix} N & 0 & \dots & 0 \\ 0 & 1 & \dots & 0 \\ \vdots & \vdots & \ddots & \vdots \\ 0 & 0 & \dots & 1 \end{bmatrix} \tag{4.46}$$

is a $\left(N^2-N+1\right)\times\left(N^2-N+1\right)$ diagonal matrix.

When $N > 4$, a perfect Golomb ruler that can sample all the integers within G_N by $\Delta G_{n,m}$ does not exist, and thus $G_N > N(N-1)/2$. Therefore, we cannot construct a DFT matrix from $\mathbf{w}_k$, unlike the case of UOPA described in Appendix A. However, by adding elements that correspond to the missing integers, we can construct a DFT matrix, and thus we can make

the discussion similar to that in Appendix A.

First, we define the set of integers $\mathscr{N}$ with $2G_N + 1$ elements that includes all the integers within the width of $\mathscr{R}(\Delta x)$ of the Golomb ruler G_N, that is,

$$\mathscr{N} \equiv \{n \mid -G_N \leq n \leq G_N\}. \tag{4.47}$$

We then define another set of integers $\mathscr{G}$ with $N^2 - N + 1$ elements that includes all the integers that can be sampled by the Golomb ruler, that is,

$$\mathscr{G} \equiv \left\{\Delta G_{n,m} \mid 1 \leq n, m \leq N\right\}. \tag{4.48}$$

Using $\mathscr{N}$ and $\mathscr{G}$, we can define a set of integers $\mathscr{L}$ with $2G_N - N(N-1)$ elements that correspond to the integers that is within the range of $\mathscr{R}(\Delta x)$ but cannot be sampled by the Golomb ruler, that is,

$$\mathscr{L} \equiv \mathscr{N} \cap \overline{\mathscr{G}} \equiv \{L_n \mid 1 \leq n \leq 2G_N - N(N-1)\}, \tag{4.49}$$

where L_n are the each integer included in $\mathscr{L}$. Using L_n, we can define a $(2G_N + 1) \times 1$ vector $\mathbf{w}_k$ as

$$\mathbf{z}_k \equiv \sqrt{\frac{1}{2G_N + 1}} \begin{bmatrix} \mathbf{w}_k \\ \alpha^{L_1 k} \\ \alpha^{L_2 k} \\ \vdots \\ \alpha^{L_{2G_N - N(N-1)} k} \end{bmatrix}. \tag{4.50}$$

$\mathbf{w}_k$ can be written as a truncated and normalized vector of $\mathbf{z}_k$ as

$$\mathbf{w}_k = \mathbf{Y}\mathbf{z}_k, \tag{4.51}$$

where

$$\mathbf{Y} \equiv \sqrt{\frac{2G_N + 1}{N^2 - N + 1}} \begin{bmatrix} \mathbf{1}_{(N^2-N+1)\times(N^2-N+1)} & \mathbf{0}_{(N^2-N+1)\times[2G_N - N(N-1)]} \end{bmatrix} \tag{4.52}$$

As a result, $\mathbf{Q}$ can be written as

$$\mathbf{Q} = \mathbf{HW} = \mathbf{HYZ} = \mathbf{XZ} = \mathbf{1}_{\left(N^2-N+1\right)\times\left(N^2-N+1\right)}\mathbf{XZ}, \tag{4.53}$$

where $\mathbf{Z} \equiv \left[\mathbf{z}_1, \mathbf{z}_2, ..., \mathbf{z}_{2G_N+1}\right]$, $\mathbf{W} \equiv \left[\mathbf{w}_1, \mathbf{w}_2, ..., \mathbf{w}_{2G_N+1}\right]$, and $\mathbf{X} \equiv \mathbf{HY}$.

Similar to $\mathbf{V}$ in Appendix A, $\mathbf{Z}$ is a $(2G_N + 1)$-point DFT matrix (again, with some rearrangement in the order of row vectors). Thus, $\mathbf{Z}$ is obviously a unitary matrix. Furthermore,

$$\mathbf{X} = \sqrt{\frac{2G_N + 1}{N^2 - N + 1}}\left[\mathbf{H} \quad \mathbf{0}_{\left(N^2-N+1\right)\times\left[2G_N - N(N-1)\right]}\right] \tag{4.54}$$

is a $(N^2 - N + 1) \times (2G_N + 1)$ rectangular diagonal matrix , and $\mathbf{1}_{\left(N^2-N+1\right)\times\left(N^2-N+1\right)}$ is obviously a unitary matrix. Therefore, Eq. (4.53) is the SVD of $\mathbf{Q}$, and the singular values of $\mathbf{Q}$ are

$$\sigma_\xi = \begin{cases} N\sqrt{2G_N + 1} & (\xi = 1) \\ \sqrt{2G_N + 1} & (\xi = 2, 3, ..., N^2 - N + 1) \end{cases}, \tag{4.55}$$

from which Eq. (4.31) is derived.

4.C Comment on the number of resolvable points for the case of UOPA

As discussed in Section 3.2, the number of resolvable points, or rank($\mathbf{I}$), is $2N - 1$ for the case of UOPA, which is larger than that estimated simply from the ratio between the full-width-at-half-maximum (FWHM) of the beam and the FOV. In a simple beam-steering-based imaging system, where each steered beam is directly assigned to the corresponding pixel, the number of resolvable points coincides with the number of beams that can be packed inside the FOV without a significant overlap. Therefore, it is commonly calculated as FOV/FWHM, which is approximately N in case of UOPA. Figure 4.14(a) shows how the beam from a UOPA ($N = 10$) can be steered within an FOV at a spacing equal to the FWHM of each beam. Indeed, we can confirm that only 11 beams can fit inside the FOV.

However, in the single-pixel imaging (SPI) where matrix inversion process as described by Eq. (4.4) is applied, $2N - 1$ points can be resolved at the maximum. Figure 4.14(b) shows $2N - 1$ focused beams from UOPA ($N = 10$) steered within the FOV. We see that the beams largely overlap with each other in such a densely packed condition. However, through the matrix inversion process described by Eq. (4.4), such overlaps can be deconvoluted to obtain a fine image of the target. In other words, although these beams are not necessarily orthogonal with each other, they are linearly independent and their ensemble spans a $2N - 1$ dimensional

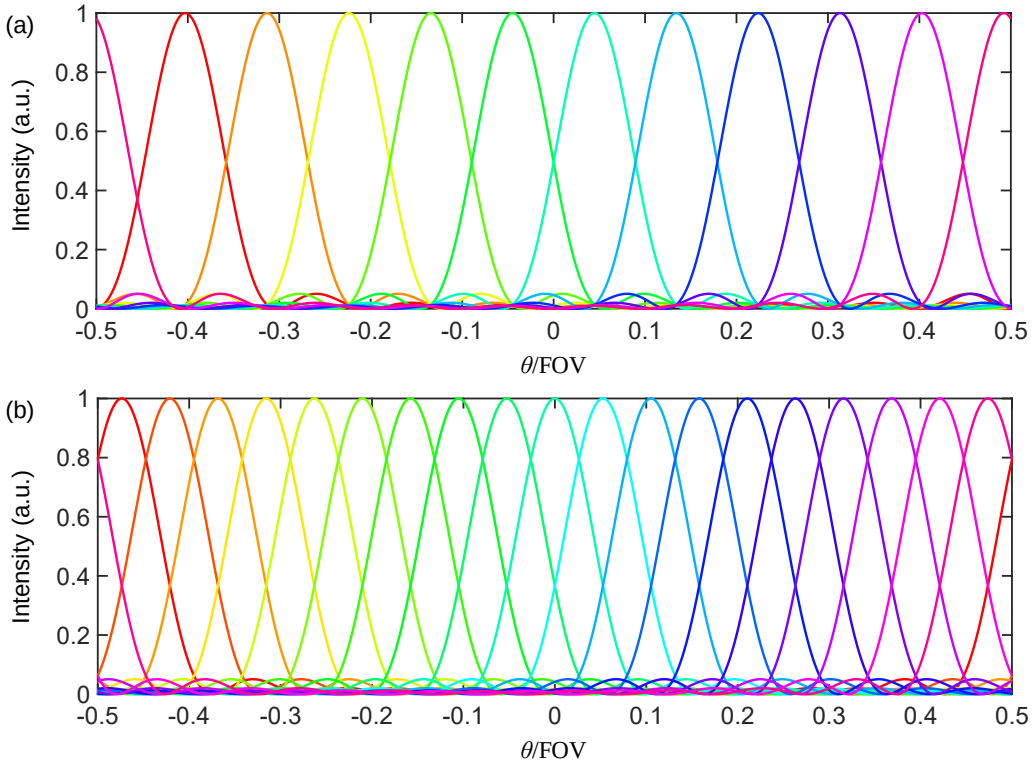

Fig. 4.14: Steered beams within an FOV for the case of UOPA ($N = 10$). (a) When the spacing of the beams are equal to the FWHM, 11 beams fit inside the FOV. (b) If the matrix inversion process is applied, $2N - 1$ beams within the FOV can be used to reconstruct the image.

vector space.

4.D Imaging results using the beam steering condition

In Fig. 4.15, we depict the imaging result when we drive the OPA under a beam-steering condition, i.e., Eq. (4.24) for the case of UOPA and Eq. (4.30) for the case of NROPA. The parameters are the same as those assumed in Section 4: $K = 1000$ (meaning that the beam is formed at 1000 equally spaced angles within the FOV), $N = 16$, and SNR = 20 dB (for the case with noise). Figures 4.15(a) and (b) show the results when we retrieve the images through the matrix inversion process, described by Eq. (4.4), for the case of UOPA and NROPA, respectively. We can see that the image qualities are similar to those in Fig. 4.11. For reference, Figs. 4.15(c) and (d) show the cases where the images are obtained by simply assigning each steered beam to the corresponding pixel without the matrix inversion process (as explained in Appedix C). In such a case, S_k, which denotes the transmitted power of the k-th beam, is directly used to plot the intensity of the k-th pixel. For the case of UOPA, we can see that the high spatial frequency components are further suppressed compared to the

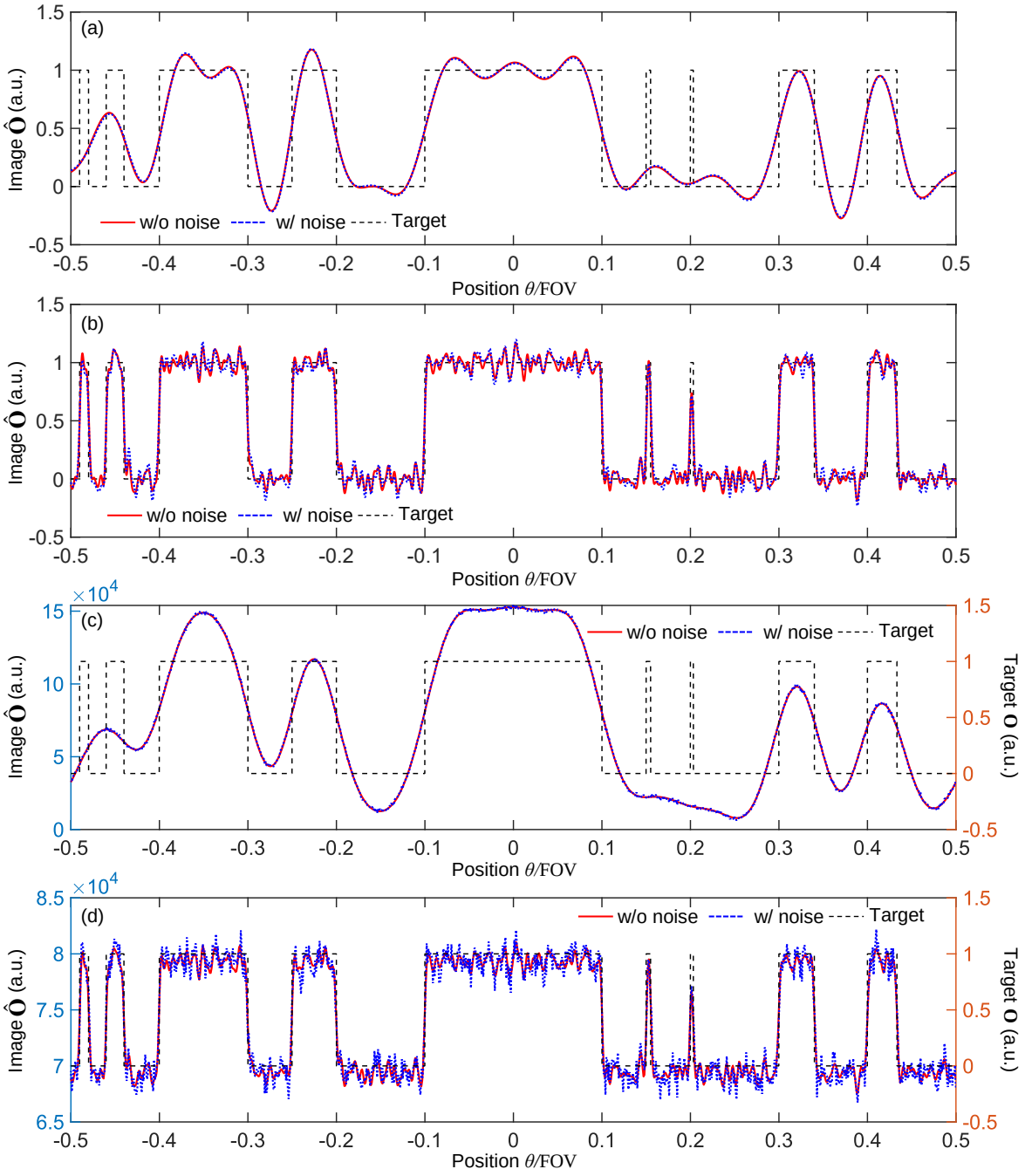

Fig. 4.15: Imaging result (K = 1000) without noise (red-solid) and with noise (blue-dotted, SNR = 20 dB) using (a) UOPA (N = 16) with matrix inversion, (b) NROPA (N = 16) with matrix inversion, (c) UOPA (N = 16) without matrix inversion, (d) NROPA (N = 16) without matrix inversion. The imaging target (black-broken) is plotted together.

case of using the matrix inversion [Fig. 4.15(a)]. This is in agreement with the discussion in Appendix C; the number of resolvable points derived from the FWHM of the beam is smaller compared to that derived from the number of independent vectors in **I**.

In contrast, for the case of NROPA, the retrieved images do not have significant difference in both cases [Figs. 4.15(b) and (d)]. This is because $\mathscr{R}(\Delta x)$ is flat other than the zero-frequency component, and all spatial frequency components contribute equally to S_k. However, due to the zero-frequency offset, the extinction ratio of the image becomes smaller in Fig. 4.15(d) compared to Fig. 4.15(b). Thus, the matrix inversion processing is still effective for the case of NROPA as well to reduce the impact of the receiver noise and enhance the extinction ratio.

4.E Singular values for the randomly driving case of UOPA

Here, we discuss the singular value distribution for the randomly driving case of UOPA, i.e., we discuss the singular value distribution of **R**. It is convenient to define the row vectors of **R**, that is,

$$\mathbf{R} = \begin{bmatrix} \mathbf{\Lambda}_1 \\ \mathbf{\Lambda}_2 \\ \vdots \\ \mathbf{\Lambda}_{2N-1}, \end{bmatrix} \tag{4.56}$$

where

$$\mathbf{\Lambda}_m = \begin{cases} \left[\sum_{n=1}^{N-m+1} \exp\left(\mathrm{i}\Delta\phi_{n,n+m-1;1}\right) \;\; \sum_{n=1}^{N-m+1} \exp\left(\mathrm{i}\Delta\phi_{n,n+m-1;2}\right) \;\; \cdots \;\; \sum_{n=1}^{N-m+1} \exp\left(\mathrm{i}\Delta\phi_{n,n+m-1;K}\right) \right]^{\mathrm{T}} & (m \le N) \\ \left[\sum_{n=1}^{2N-m} \exp\left(\mathrm{i}\Delta\phi_{n+(m-N),n;1}\right) \;\; \sum_{n=1}^{2N-m} \exp\left(\mathrm{i}\Delta\phi_{n+(m-N),n;2}\right) \;\; \cdots \;\; \sum_{n=1}^{2N-m} \exp\left(\mathrm{i}\Delta\phi_{n+(m-N),n;K}\right) \right]^{\mathrm{T}} & (m \ge N+1) \end{cases} \tag{4.57}$$

The inner product between λ_m and $\lambda_{m'}$ can be written as (assuming that $m, m' \leq N$, while the same discussion holds for other cases)

$$\mathbf{\Lambda}_m^* \mathbf{\Lambda}_{m'}^{\mathrm{T}} = \sum_{k=1}^{K} \sum_{n'=1}^{N-m'+1} \sum_{n=1}^{N-m+1} \exp\left(\mathrm{i}\Delta\phi_{n,n+m-1;k}\right) \exp\left(\mathrm{i}\Delta\phi_{n',n'+m';k}\right). \tag{4.58}$$

If $\Delta\phi_{n,n+m-1;k}$ and $\Delta\phi_{n',n'+m'-1;k}$ distributes randomly and uniformly within $(0, 2\pi)$, which is true for the randomly driving condition, $\mathbf{\Lambda}_m^* \mathbf{\Lambda}_{m'}^{\mathrm{T}}$ for $m \neq m'$ converges to 0 when K is large. Therefore, all $\mathbf{\Lambda}_m$ are mutually orthogonal. As a result, the L2 norm of $\mathbf{\Lambda}_m$ devided by K will define the singular values of $\mathbf{R}$.

At large K, L2 norm of $\mathbf{\Lambda_m}$ will converge to

$$\lim_{k\to\infty} \mathrm{norm}\left(\mathbf{\Lambda}_m\right) = \begin{cases} NK & (m = 1) \\ K\sqrt{\mathcal{E}\left[\left|\sum_{n=1}^{N-m+1} \exp\left(\mathrm{i}\Delta\phi_{n,n+m-1;k}\right)\right|^2\right]} & (2 \leq m \leq N) \\ K\sqrt{\mathcal{E}\left[\left|\sum_{n=1}^{2N-m} \exp\left(\mathrm{i}\Delta\phi_{n+(m-N),n;k}\right)\right|^2\right]} & (N+1 \leq m \leq 2N-1) \end{cases} \tag{4.59}$$

where $\mathcal{E}$ denotes the expectation value. Below, we consider the case of $2 \leq m \leq N$ for simplicity, but the same discussion holds for $N + 1 \leq m \leq 2N - 1$. The expectation value for

the case of $2 \leq m \leq N-1$ can be calculated as

$$\begin{aligned}
&\mathcal{E}\left[\left|\sum_{n=1}^{N-m+1}\exp\left(\mathrm{i}\Delta\phi_{n,n+m-1;k}\right)\right|^2\right] \\
&= \int_0^{2\pi}\frac{\mathrm{d}\Delta\phi_1}{2\pi}\int_0^{2\pi}\frac{\mathrm{d}\Delta\phi_2}{2\pi}\cdots\int_0^{2\pi}\frac{\mathrm{d}\Delta\phi_{N-m+1}}{2\pi}\left|\sum_{n=1}^{N-m+1}\exp\left(\mathrm{i}\Delta\phi_n\right)\right|^2 \\
&= \int_0^{2\pi}\frac{\mathrm{d}\Delta\phi_1}{2\pi}\int_0^{2\pi}\frac{\mathrm{d}\Delta\phi_2}{2\pi}\cdots\int_0^{2\pi}\frac{\mathrm{d}\Delta\phi_{N-m+1}}{2\pi} \\
&\left[\exp\left(-\mathrm{i}\Delta\phi_{N-m+1}\right)+\sum_{n=1}^{N-m}\exp\left(-\mathrm{i}\Delta\phi_n\right)\right]\left[\exp\left(\mathrm{i}\Delta\phi_{N-m+1}\right)+\sum_{n=1}^{N-m}\exp\left(\mathrm{i}\Delta\phi_n\right)\right] \\
&= \int_0^{2\pi}\frac{\mathrm{d}\Delta\phi_1}{2\pi}\int_0^{2\pi}\frac{\mathrm{d}\Delta\phi_2}{2\pi}\cdots\int_0^{2\pi}\frac{\mathrm{d}\Delta\phi_{N-m+1}}{2\pi}\left[1+\exp\left(-\mathrm{i}\Delta\phi_{N-m+1}\right)\sum_{n=1}^{N-m}\exp\left(\mathrm{i}\Delta\phi_n\right)\right. \\
&\qquad \left.+\exp\left(\mathrm{i}\Delta\phi_{N-m+1}\right)\sum_{n=1}^{N-m}\exp\left(-\mathrm{i}\Delta\phi_n\right)+\left|\sum_{n=1}^{N-m}\exp\left(\mathrm{i}\Delta\phi_n\right)\right|^2\right] \\
&= 1+\int_0^{2\pi}\frac{\mathrm{d}\Delta\phi_1}{2\pi}\int_0^{2\pi}\frac{\mathrm{d}\Delta\phi_2}{2\pi}\cdots\int_0^{2\pi}\frac{\mathrm{d}\Delta\phi_{N-m}}{2\pi}\left|\sum_{n=1}^{N-m}\exp\left(\mathrm{i}\Delta\phi_n\right)\right|^2 \\
&= 1+\mathcal{E}\left[\left|\sum_{n=1}^{N-m}\exp\left(\mathrm{i}\Delta\phi_{n,n+m-1;k}\right)\right|^2\right].
\end{aligned} \tag{4.60}$$

On the other hand, when $m = N$,

$$\mathcal{E}\left[\left|\exp\left(\mathrm{i}\Delta\phi_1\right)\right|^2\right] = 1. \tag{4.61}$$

Therefore,

$$\mathcal{E}\left[\left|\sum_{n=1}^{N-m+1}\exp\left(\mathrm{i}\Delta\phi_{n,n+m-1;k}\right)\right|^2\right] = N-m+1 \tag{4.62}$$

for $2 \leq m \leq N$ and

$$\mathcal{E}\left[\left|\sum_{n=1}^{2N-m}\exp\left(\mathrm{i}\Delta\phi_{n+(m-N),n;k}\right)\right|^2\right] = 2N-m \tag{4.63}$$

for $N+1 \leq m \leq 2N-1$.

As a result, by organizing in the order of magnitude, the singular values σ_n ($n = 1, 2, \ldots, 2N-$

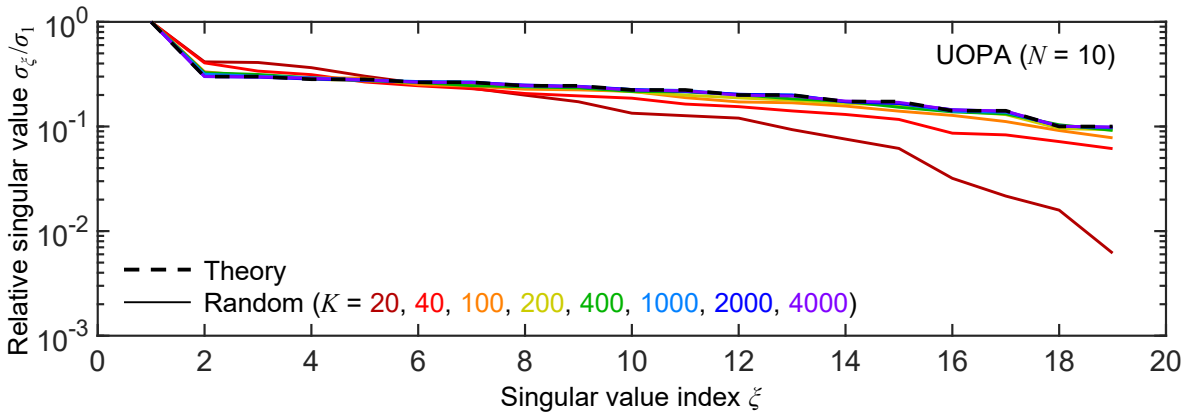

Fig. 4.16: Relative singular value distribution of **R** calculated for the randomly driving condition of UOPA with $N = 10$, which is compared with the theoretically derived singular value (black-dashed).

1) of **R** at large K can be written as

$$\begin{aligned}&[\sigma_1, \sigma_2, \sigma_3, ..., \sigma_{2N-1}] \\ &= \left[N, \sqrt{N-1}, \sqrt{N-1}, \sqrt{N-2}, \sqrt{N-2}, \sqrt{N-3}, ..., \sqrt{2}, 1, 1\right].\end{aligned} \tag{4.64}$$

Figure 4.16 compares the theoretical value derived here (black-dashed) and the singular value distribution when the phase shifters are randomly driven. We can see perfect agreement between the theory and the numerical result when K is large.

4.F Impact of limited ADC bit resolution on the singular value distribution

In [196], it has been pointed out that for SSPI using UOPA, the DAC resolution can be small as 3-values (< 2 bits) in order to obtaine a fine image. On the other hand, the impact of limited ADC resolution on the singular value distribution has not yet been clarified. Moreover, it is not yet clear if the same thing hold for the case of NROPA. In order to quantitatively investigate this point, we perform the singular value decomposition assuming that the ADC bit resolution is limited.

In Fig. 4.17, we show how the singular values of **R** (for the randomly driving case of UOPA) changes when the DAC resolution varies. Here, we assume random phase offset emulating phase error accumulated by refractive index deviation. Strikingly, there is almost no penalty compared to the case of infinite ADC-resolution (black-dashed) as long as the DAC have more

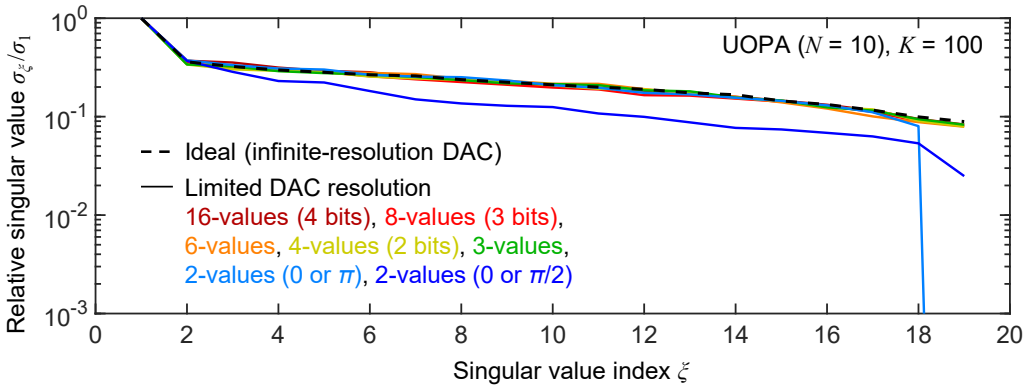

Fig. 4.17: Relative singular value distribution of **R** when the DAC bit resolution varies.

than 3 output values. Even for the 2-value-DAC (1 bit), the penalty is small. Slight difference of the result presented in [196] where no image can be obtained for the case of 2-valued DAC is that here we assumed random phase offset. If there is no phase offset, the interference fringes are always even function if $\phi = 0, \pi$. However, under the impact of random phase offset, we can sample both the even function interference fringe and the odd function interference fringe by utilizing several pairs of antennas with different phase offset difference but generate interference fringes with same spatial frequency. Nevertheless, if $\phi = 0, \pi$, only 1 out of 2 degree of freedom of the complex plane can be leveraged if only a single pair of antennas generate the corresponding spatial frequency. This is the reason of $\sigma_{19} = 0$ for the case of 2-value-DAC with $\phi = 0, \pi$. In contrast, for a 2-value-DAC with $\phi = 0, \pi/2$, both of the degree of freedom of the complex plane could be leveraged, and therefore $\sigma_{19} > 0$. The remaining penalty could be attributed to the limited range of phase shift.

In Fig. 4.18, we show how the singular values of **Q** (for the randomly driving case of NROPA) changes when the DAC resolution varies. Again, we assume random phase offset emulating phase error accumulated by refractive index deviation. Similar to the case of UOPA, there is almost no penalty compared to the case of infinite ADC-resolution (black-dashed) as long as the DAC have more than 3 output values. On the other hand, for 2-value-DAC with phase shift values of $\phi = 0, \pi$, $\sigma_\xi = 0$ for $\xi > (N^2 - N)/2 + 1$. This is because only 1 out of the 2 degree of freedom of the complex plane is utilized in such driving condition. Although there are a bit more effective singular values for the case of 2-value-DAC with phase shift values of $\phi = 0, \pi/2$, there is significant number of information lost, implying that 2-value-DAC is insufficient for driving an NROPA for SSPI.

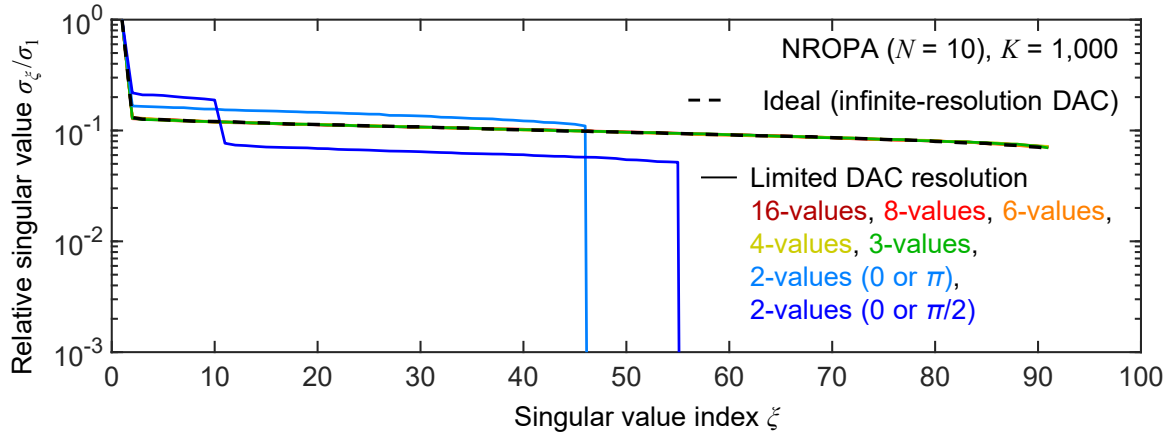

Fig. 4.18: Relative singular value distribution of $\mathbf{Q}$ when the DAC bit resolution varies.

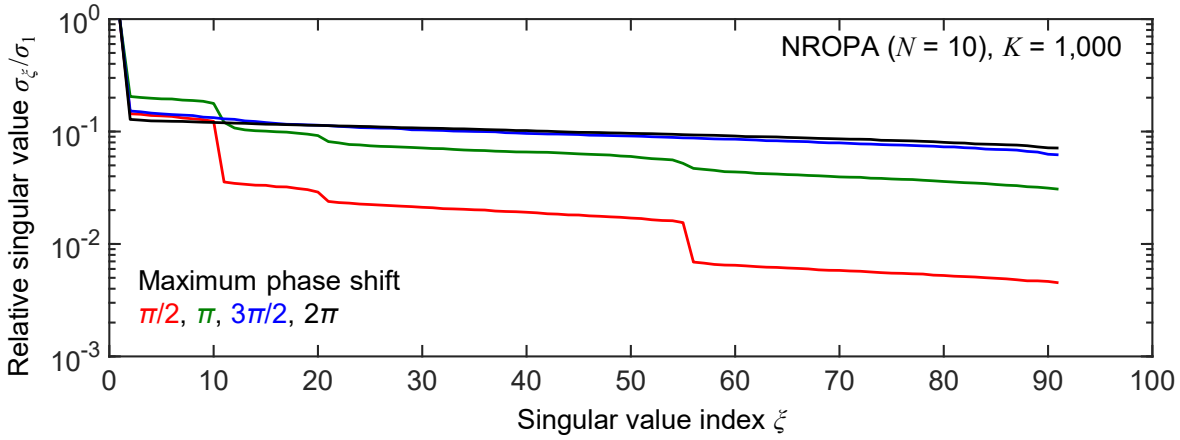

Fig. 4.19: Relative singular value distribution of $\mathbf{Q}$ when the range of phase shift is limited.

4.G Impact of limited phase shift on the singular value distribution

In [197], SSPI with limited range of phase shift for the case of UOPA has been studied. Here we provide the result of how the limited range of phase shift has a impact on the singular value distribution for the case of NROPA. In Fig. 4.19, we show how the singular values of $\mathbf{Q}$ (for the randomly driving case of NROPA) changes when the maximum value of phase shift is varied. We can see that similar to the result of UOPA in [197], if the maximum phase shift is large as $3\pi/2$, there is almost no penalty in the singular value distribution.

CHAPTER 5

EXPERIMENTAL STUDY OF SPECKLE-BASED SINGLE-PIXEL IMAGING USING NON-REDUNDANT OPTICAL PHASED ARRAY

This Chapter is intentionally omitted in this version.

CHAPTER 6

DEMONSTRATION OF OPTICAL PHASE MONITORING CIRCUIT

This Chapter is intentionally omitted in this version.

CHAPTER 7

CONCLUSION

1. Summary of accomplishments

In this work, we have explored the possibility of realizing high-resolution OPA-based sensing systems with ultimate simplicity. Key approach of this work is the concept of *NROPA*, where the redundancy is ultimately eliminated.

In Chapter 1, we have reviewed the background of this research. In particular, extensive review of the research status of OPA has been presented.

In Chapter 2, we proposed the concept of NROPA through in-depth theoretical analysis on FFP of the OPA. We have clarified, for the first time, the importance of broadening and flattening the autocorrelation function $\mathscr{R}_{aa}(\mathbf{\Delta})$ of the array layout function $a(\mathbf{r})$. We then pointed out that eliminating the duplication of the dispacement vectors $\mathbf{\Delta}_{n,m}$ between pairs of elements is critically effective. As an array that satisfy such requirement, we introduce the concept of *NRA*, which is well known in the context of VLBI or DOA. In this work, *we use the concept of NRA for emitting and synthesizing coherent beam of light*, while most of the previous work use NRA for receiving incoherent radiowaves. We present systematic numerical analysis to support our theory. The advantages and drawbacks of the NROPA is clarified through these analysis. In particular, the revolutional scalability of the spatial resolution of NROPA is presented, whose number of resolvable points scales with $O\left(N^2\right)$. This is in clear contrast to the case of UOPA, where the number of resolvable points scales only with $O\left(N\right)$.

In Chapter 3, we experimentally demonstrated the concept of NROPA through beam steering experiment using a Costas-array-based 2D NROPA with $N = 127$. We designed and fabricated a silicon photonic OPA based on multi-project wafer foundry service. An experiment system consisting of the chip, lens system, driver circuit, and control system is built to characterize the chip. Beam steering was succesfully performed by carefully optimizing the driving condition of the phase shifters. The obtained beam after running the optimization algorithm showed excellent agreement with the theory. The number of resolvable points defined by FOV/FWHM was ~19,000, which is, to the best of our knoweledge, the largerst number of resolvable points

attained by an OPA operating at a single wavelength.

In Chapter 4, we presented a systematic and comprehensive analysis of SSPI using NROPA and UOPA. Through theoretical analysis, we quantitatively clarify the number of resolvable points for each case. While only $2N-1$ points can be resolved for the case of UOPA, N^2-N+1 points can be resolved for the case of NROPA. These numbers are directly related to the number of non-zero peak of $\mathscr{R}_{aa}(\mathbf{\Delta})$, which is equal to the number of interference fringes with distinct spatial frequencies. This analysis provides, for the first time, a comprehensive and quantitative understanding of the number of resolvable points in SSPI using OPAs; prior to this work, the quantitaive resolution limit of SSPI using an OPA was not clearly understood, even for the case of UOPA. Comprehensive numerical analysis was also presented to support our theory. A test case of SSPI was numerically presented to demonstrate the effectiveness of SSPI using NROPA.

In Chapter 5, we experimentally studied the possibility of SSPI using an NROPA. We have built an experiment setup for SSPI, with several improvements from that presented in Chapter 3. Unfortunately, clear imaging is not yet demonstrated due to some experimental issues. However, the spatial frequency spectrum of the speckle patterns shows good agreement with the theory. Fine imaging should be realized in near future by solving some trivial experimental issues.

In Chapter 6, we studied the phase monitoring circuit towards the realization of practical OPA that can perform deterministic control with on-chip calibration. The NROPA and the phase monitoring circuit are excellently compatible, since an OPA with $O\left(N^2\right)$ resolvable points can be managed with only N monitoring ports. The required optical phase accuracy and photocurrent detection accuracy have been numerically and theoretically studied. Although the required phase accuracy increases with N for the relative phase monitoring circuit, it is not a big deal for NROPAs since N can be minimized. We designed and fabricated a silicon NROPA chip ($N = 16$) with integrated optical phase monitoring circuit. Good agreement between the extracted optical phase and the observed FFP is demonstrated through the characterization of the chip.

2. Concluding remarks

Overall, we have presented the pathway towards realizing high-resolution OPA with reduced complexity, in particular by minimizing the number of antennas N.

NROPA is an effective mean to generate a beam with a sharp intensity peak with a minimal number of phase shifters; $O(N^2)$ degrees of freedom can be explored with only N phase shifters, i.e., N degrees of freedom. This seemingly mistereous mismatch of the degree of freedom is enabled by the nonlinearity inherent in the conversion from the electric field to

the intensity pattern. On the other hand, we should be aware of the drawback of NROPA that accompanies with the mismatch in the degree of freedom; the optical power inside the main beam decreases inversely proportional to N. The NROPA is therefore unsuitable for applications where the total optical power in the main beam is important or the signal-to-noise ratio requirement is sevior, such as long range sensing for autonomous vehicles and free-space optical communication. On the other hand, NROPA can be powerful for applications where the intensity profile is improtant rather than the field profile, and where the optical power requirement is not strict. SSPI studied in this work is a typical system where the intensity profile is important rather than the field profile. The optical power requirement depends on the application, but short-range sensing application such as flow cytomery [**?**] could benefit from the high-resolution nature of NROPA, and moreover, could potentially enjoy the ultra-high operation speed of OPAs. Another possible application that could benefit a lot from NROPA is imaging systems based on nonlinear optics, where the intensity profile is critically important. In such systems, the impact of noise-like background intensity profile of the beams from NROPAs can be greatly suppressed thanks to the nonlinearity. The signal-to-noise ratio can potentially be improved by leveraging the higher order nonlinearities. An alternative scenario to alleviate the problem of poor signal to noise ratio is using the NROPA both at the tranceiver and at the receiver, just as in traditional RADARs, but still, the achievable signal power and signal to noise ratio should be poor compared to using UOPA. Here, we should note that in any situation, the drastic reduction of N by NROPA will enable significant reduction in system cost and complexity.

Compared to the previous work of non-uniform OPAs based on iterative optimizations or any other brute-force strategies, the concept of NROPA is supported by theory. The theoretical discussion presented in this dissertation is effective to understand the previous reports of non-uniform OPAs, whose mechanism of the resolution enhancement was not understood well. In terms of performance, we should be aware that there is a clear tradeoff between the number of resolvable points and the optical power in the main lobe. As we have discussed in Chapter 2, the peak optical intensity is independent on the array configuration (if the FOV and the antenna mode profile are the same) and is purely determined by N. Therefore, the power in the main lobe will decrease proportionally with the number of resolvable points, depending on the number of resolvable points. This means that NROPA is not completely superior to the previous non-uniform OPAs; it is a matter of balance between the optical power in the main lobe and the number of resolvable points[*1]. In that sence, NROPA is an extreme case where

[*1] We should note that the pseudo-random array has a slightly different aspect. For the case of pseudo-random array (where the antennas are no longer located based on integer-based lattice points), the number of resolvable points is enhanced by random perturbation of the antenna location, which results in the disappearance of the higher order diffraction peaks. On the otherhand, the width of the main beam, and thus the optical power in the main beam, remains almost the same. Therefore, a larger FOV and number of resolvable points can be

the optical power is ultimately sacrificed to maximize the number of resolvable points[*2]. The theoretical discussion and the NROPA concept presented in this work answer a fundamental question of what the theoretical upper limit of the resolution enhancement is. We should note that the array design for a given number of resolvable points is not trivial as well; the antennas must be located so that a single intensity peak is formed at the far field plane and that large sidelobe suppresion ratio is attained. We also should stress again that the experiment presented in this work is the state-of-the-art demonstration of a high-resolution OPA. A record-large number of resolvable points, and record-high degree of resolution enhancement through non-uniform array structure engineering, are attained, respectively. On the other hand, regarding the experiment, we still have not demonstrated the application of NROPA, which should be further explored in the future.

Another important contribution of this dissertation is the deep understanding on the number of resolvable points in SSPI using OPAs. The result is in fact very general: the limit $N^2 - N + 1$ presented in this work is universal for any sytem that consists of N modulators. The quantitative understanding before this work was limited perhaps since the previous work employs spatial light modulators with massive number of pixels and thus the limit induced by the number of modulators was not important. Through this work, we have shown that $N^2 - N + 1$ resolvable points can be obtained with only N modulators. This opens up the possibility of leveraging high-speed OPAs for SSPI, which potentially can provide orders of magnitudes improvement in the imaging framerate. However, again, we should note that the non-redundant nature of the NROPA imposes penalty in the signal-to-noise ratio requirement. Nevertheless, in SSPI, the SNR requirement can be relaxed to some extent by increasing the number of measurements K so that the impact of noise can statistically cancel out. Another thing we should note is the penalty of driving the phase shifters randomly instead of precisely tuning them according to the beam steering condition. In UOPA, the penalty in the singular values (directly leading to penalty in signal-to-noise ratio) induced by driving the phase shifters randomly is non negligiblely large (as quantitatively discussed in Chapter 4). In contrast, for NROPAs, there is almost no penalty when K is sufficiently large, which is a very surprizing nature of NROPA-SSPI revealed in this work. Thus, NROPA and SSPI is highly compatible, and NROPA-SSPI

attained for a given average spacing between antennas without sacrificing (compared to the perturbation-less case) the optical power in the main beam (the optical power in the higher order diffraction peak is lost instead). However, in order to enjoy the enhancement in the spatial resolution, the range of radiation from a single antenna must be several times larger than the FOV without perturbation. As a result, the optical power (without any perturbation to the array) is smaller compared to the case where the FOV and the range of radiation from a single antenna matches, corresponding to the distribution of the optical power to the higher order diffraction peaks. Therefore, the tradeoff between the number of resolvable points and the optical power in the main beam is universal. Nevertheless, the pseudo-random array is however powerful in increasing the FOV and in cases where making the average spacing between adjacent antennas small is difficult (like in 2D OPAs).

[*2] In contrast, UOPA is the extreme case where the optical power is maximized and the number of resolvable points is sacrificed. Nevertheless, to be honest, optical power is extremely critical in many applications, and thus UOPAs with a large N will still be the basic strategy for those applications.

is a promising imaging scheme for high-resolution SSPI with reduced system complexity*[3].

The extraordinary compatibility of the NROPA and the phase monitoring circuit should also be highlighted. The advantage of monitoring the OPA in a on-chip manner with minimal complexity makes NROPA further attractive. I also should mention that the quantitative result regarding the impact of phase error, relative phase error, and photocurrent detection error is universal but was not well known, and should benefit a vast range of research on OPAs*[4]. One good new is that the required optical phase accuracy is not as strict (~ 0.2 rad should be enough) and does not scale with N. On the other hand, for the optical phase monitoring circuit, since we monitor the relative optical phase rather than the optical phase itself, the error accumulates and thus the required detection accuracy increases with N, which could be problematic. In such context, NROPA can be further advantageous, since by minimizing N, the accumulation of error can be minimized. However, we also should be aware that NROPA is less tolerant to phase error in terms of sidelobe suppresion ratio due to its non-redundant nature. Regarding the experiment, the device presented in this work was not perfect, but the problem of the emission angle deviation of the antennas should be realtively easily solved by improving the design of the antennas. On the otherhand, one big issue is the phase error accumulation due to the optical path length between the phase monitoring section and the antennas. This phase error accumulation prevents the direct monitoring of the optical phase and will impose the requirement of an initial calibration step to extract this accumulated phase error (although it is a single step process, this accumulation of relative phase is sensitive to the environment and thus the system must be stabilized well). This should possible be solved by minizing the distance between the antennas and the phase monitoring section, either by simply optimizing the waveguide routing or by designing special structures (such as distributed reflective couplers) to partially sample the light at the input of antennas and to mix them with each other.

Finally, I should stress again that the discussion focusing on the intensity pattern and autocorrelation function presented in this work is rather original in the field of OPA, and should provide new perspective to the community. I expect that this disseration will contribute in the realization of high-resolution OPA with reduced complexity, and in the deep understanding of resolution enhancement by non-uniform OPAs.

*[3] However, we should note that SSPI in general do not have a clear application at this moment.

*[4] For example, the discussion on the phase accuracy requirement may directly answer the refractive index accuracy requirements of dispersive OPAs.

Acknowledgments

The work presented in this thesis would have never been accomplished without the numerous support that I luckily have received. Here I would like to express my gratitude to all the people who have helped me make my graduate school life fruitful, productive, and enjoyable.

Over anything else, I would like to express my deepest gratitude to my supervisor, Prof. Takuo Tanemura. Since I joined Tanemura Lab in 2018, he has continuously supported, guided, and encouraged me in numerous aspects, including research, career, and life. I still remember what he replied when I mailed him that I passed the graduate school exam and that I would join his lab; "Let's enjoy a lot of fun from next year," and indeed, it became true. The 5 years I spent in his lab will definitely be a treasure of my life. When we had discussions, he always gave us very insightful advice based on his deep experiences and knowledge, but from an equal perspective, and treated me as a full-fledged researcher, carefully listening to my opinions as well. As a supervisor, he basically let me work freely, but at the same time, he guided me carefully at the key points of research. He also patiently and carefully corrected my manuscripts in detail, which was very helpful for me in cultivating techniques and attitude towards writing. His kind and cheerful personality has always made our graduate school life enjoyable. I also really like his attitudes and philosophy as a researcher in the field of electronic engineering: being practical and academic simultaneously, and making sure that the work "makes sense." I definitely inherit those philosophies and attitudes toward research from him.

I would also like to express my sincere gratitude to my co-advisor, Prof. Yoshiaki Nakano. He always provided us with a great environment to concentrate on research in terms of budget, lab culture, and human connections. In particular, I would definitely have to acknowledge the extremely high-level research equipment accessible in our group, which is obviously the fruit of the continuous efforts of the professors, especially, Nakano-sensei. He constantly encouraged and supported us, but never enforced the direction of research; we were able to work on what we wanted to do. This culture ended up cultivating our independency and assertiveness.

I am deeply grateful to my Ph.D. defense committees: Prof. Satoshi Iwamoto, Prof. Yasuyuki Ozeki, and Prof. Tomohiro Kita. They have made numerous productive and

meaningful comments on my work, which were highly helpful in improving the quality of this dissertation. Moreover, I felt some kind of fate to have these proffesors as the defense committees with whom I have personal relations. I would like to express my gratitude to Iwamoto-sensei. At JSAP meetings, he kindly let us join the drinking party of his lab, where we enjoyed talking about many topics. In RINKO and lectures, he kindly answered and commented on many of my primitive questions, which always provided me with new and deeper insights into optical physics. I would like to express my gratitude to Ozeki-sensei for his support in broad aspects. We had numerous discussions over research, which were critical and insightful. He also kindly helped us with technical aspects of research as well, like circuit design and fiber splicing. I also should acknowledge that my basic attitude to optical physics and linear systems was cultivated through his very insightful lectures. I would like to express my gratitude to Kita-sensei for the fruitful discussions and enjoyable chats that we enjoyed at various conference sites, which made my business trips more enjoyable.

I would like to express my gratitude to Prof. Shinichi Takagi and Prof. Mitsuru Takenaka for their countless support during my undergraduate research. My basic attitude towards research was cultivated at that time, which was very useful in thriving during my Ph.D. course. The experience of working under the leading researcher of semiconductor devices was very precious, and it enriched my life. I also would like to express my gratitude to Prof. Masakazu Sugiyama for his helpful support during my graduate school life and the stimulating discussions in lab meetings. His extraordinarily enthusiastic lecture in quantum mechanics had definitely tempted me to join the field of device physics and had changed my life. I am also grateful to Prof. Toshihiko Baba for his support in the design of silicon photonic chips and for the discussions in JSAP meetings. I would also like to express my gratitude to Prof. David A. B. Miller and Prof. Olav Solgaard for hosting us when we had an extremely stimulating visit to Stanford.

My special thanks go to Sueko Ui and Hiroe Miyagawa for their countless support in document work and Eisaku Kato for his countless support in experiments and lab management. Their excellent work made it possible for us to concentrate on research. Especially, Kato-san was a very nice near-by senior to consult about various topics, including life and career.

I am also deeply grateful to my collaborators. I would like to thank Daiji Yamashita for guiding me to the concept of NRA during the initial phase of research. It was lucky for me to come to the concept of NRA in a very efficient manner. He also has helped me a lot in understanding and developing the measurement software. Thank you to Kento Komatsu for his excellent measurement program developed during his master's research. His handwritten program was highly customizable and helped me a lot to perform measurements. Not only that, I definitely would have to acknowledge his countless contribution to lab management, including network management and the training of younger students. His marvelous result

and methodology in research have always provided me with intellectual stimulation as well. Together with Yamashita-san, Komatsu-san was an excellent friend to talk over science and technology, including some rather random topics. I thank Dr. Rui Tang for the support in the design of silicon photonic chips and for the gossip we enjoyed. I also must acknowledge Yusuke Kohno for guiding me at the very initial step of research when I joined the lab for the master's course. He, together with Takahiro Suganuma, whom I also would like to thank, was an excellent role model as a senior in the lab. I would like to express my gratitude to Ryota Tanomura for his devotion to the design of grating couplers. It was also great to have a same-grade friend in the lab, which made my lab life fun instead of a lonely one. We shared a lot of information to thrive in the busy graduate school, and also many enjoyable gossips. My special thanks go to Shun Takahashi for being an excellent collaborator in the research of phase monitoring circuits. His enthusiasm towards research always has motivated me, even during the difficult time of COVID. He developed excellent electrical circuits and software, which were mandatory to obtain nice results on the phase monitoring circuits. I also would like to thank Kuanyu Wu for working on the phase monitor.

I also would like to thank my colleagues in Nakano-Sugiyama-Tanemura laboratory. I would like to thank Go Soma and Hiroki Miyano for being excellent friends in discussing physics and technology. They also kindly supported me during the fabrication of the InP device that I was working on during D2. They always shared very stimulating research and kept me interested in research. I also would like to thank Dr. Shota Ishimura for being an excellent colleague in discussing research. His deep insight into optical communication and fiber optics provided me with a lot of new perspectives. Thank you to Maiko Ito, Toshikazu Umezaki, and Rihoko Tsuchiya for sharing a pleasant time in the lab. Their personalities always made the atmosphere warm and made our graduate school life more enjoyable. In particular, my special thank goes to Maiko Ito for her continuous support and encouragement during my Ph.D. life. I thank Dr. Warakorn Yanwachirakul, or Golf-san, for kindly helping me in crystal growth when I was working on the InP device. I also thank Meita Asami, Gan Li, and Maui Hino for being very nice friends to talk and discuss numerous topics, especially the research topics of Sugiyama Lab. They were also helpful in various aspects of lab management. I also thank Jiahao Liu for helping me in the fabrication of the InP device, especially in the EO-polymer-related processes. Thank you to Dr. Abdulaziz Elfiqi, Yuto Suzuki, Shuntaro Maeda, Kosuke Saito, Koto Ariu, Chun Ren, Keita Hirashima, and Kazuki Ichinose for the collaboration and/or discussion we enjoyed in the research and for the enjoyable talk in the lab.

I also would like to thank Yuto Miyatake and Hironobu Yoshimi (together with Go Soma) for sharing their time for the "Rindoku" of various textbooks [198–200]. We learned many things from this gathering, and I would never have accomplished reading the long but very insightful textbooks without this gathering. I thank Yoshitaka Taguchi for his helpful support in electrical

circuits. Thank you to Kei Sumita for many enjoyable discussions over semiconductor device research and for our very exciting collaboration on the InP-membrane metasurface modulator. Thank you to Takahito Takeda and Shingo Kaneta-Takada, for being nice neighbors to share gossip. I also thank Prof. Kasidit Toprasertpong, Prof. Takuya Maeda, Dr. Naoto Usami, Dr. Yuki Okamoto, and Dr. Naoki Sekine for being a helpful nearby-senior sharing numerous useful tips regarding life in the Ph.D. course. Kasidit-sensei or Champ-sensei kindly hosted us when we visited him in Stanford. Maeda-sensei has shared me a lot of interesting knowledge about widegap semiconductors, power devices, and Universities in Kansai. Usami-san was a nice friend to share gossips and have constantly encouraged us when he dropped by at Engineering building 3. Okamoto-san have shared us many knowledge in vast range of field, such as MEMS technology, server maintainance, and alcohols. Especially, I would like to thank him for providing me his excellent LaTeX template for the dissertation. Sekine-san has helped me a lot in my undergraduate research and in cultivating basic attitude as a researcher, and has also provided me a lot of knowledge on semiconductor device technology, process, and physicss.

Keiichi Iguchi of Electrodesign is acknowledged for the development of the driver circuit. Micromodule Technology is acknowledged for their contribution to the wire-bonding of the chips. Optohub and NTT-AT are acknowledged for their contribution to the packaging of the chips. I also would like to acknowledge Thorlabs and Suruga Seiki for the massive number of optical components that I bought from them. I also thank Makoto Fujiwara for his technical support regarding the electron-beam lithography during the fabrication of the InP device.

I would like to thank the Materials Education program for the future leaders in Research, Industry, and Technology (MERIT) for their financial support from October 2018 to March 2021. The great thing about this program is that they support us from the master's course, which highly motivated us to proceed to the Ph.D. course. I am sure that my choice of proceeding to the Ph.D. was correct. Moreover, the various course work, including the self-directed joint research, MERIT colloquium, special lectures, and MERIT camp, were highly meaningful. I really recommend future motivated students to join this program. I am also grateful to Prof. Ryo Shimano for using his precious time to have meetings over my progress reports. I also would like to acknowledge the Japan Society for Promotion of Science for hiring me as a research fellow from April 2021 to March 2023. The work presented in this dissertation was financially supported by the JSPS Kakenhi 18H03769, 19H00757, and 21J11982

Finally, I would like to thank my family, Noboru, Hiroko, and Naojiro, for their continuous support and encouragement throughout my life.

December 2022

Taichiro Fukui

List of Publications

* shows the publications that corresponds to the content of this dissertation.

Journal Papers

1.* S. Takahashi†, **T. Fukui**†, R. Tanomura, K. Komatsu, Y. Taguchi, Y. Ozeki, Y. Nakano, and T. Tanemura, "Silicon photonic optical phased array with integarted phase monitors," submitted to IEICE Transactions on Electronics (†: Equal contribution, *corresponds to Chapter 6*).

2.* **T. Fukui**, K. Komatsu, Y. Nakano, and T. Tanemura, "Comparative analysis of speckle-based single-pixel imaging using uniform and non-redundant optical phased arrays," Journal of Optical Society of America A, vol. 39, no. 12, pp. 2325-2338, 2022 (*corresponds to Chapter 4*).

3.* **福井太一郎**, 田之村亮汰, 小松憲人, 山下大之, 高橋俊, 中野義昭, 種村拓夫, "高分解能光掃引のための非冗長光フェーズドアレイ," 光学, vol. 51, no. 6, p. 268, 2022. (**Invited Article**, **2021 年日本の光学研究**)

4.* **T. Fukui**, R. Tanomura, K. Komatsu, D. Yamashita, S. Takahashi, Y. Nakano, and T. Tanemura, "Non-redundant optical phased array," Optica, vol. 8, no. 10, pp. 1350-1358, 2021 (*corresponds to Chapters 2 and 3*).

5. **T. Fukui**, Y. Nakano, and T. Tanemura, "Resolution limit of single-pixel speckle imaging using multimode fiber and optical phased array," Journal of Optical Society of America B, vol. 38, no. 2, pp. 379-386, 2021.

6. **T. Fukui**, Y. Kohno, R. Tang, Y. Nakano, and T. Tanemura, "Single-pixel imaging using multimode fiber and silicon photonic phased array," IEEE/OSA Journal of Lightwave Technology, vol. 39, no. 3, pp. 839-844, 2021. (**Invited Article**)

7. 種村拓夫, **福井太一郎**, 小松憲人, 中野義昭, "半導体光フェーズドアレイ素子を用いた高分解イメージング," レーザー研究, vol. 50, no. 8, pp. 463-467, 2022. (**Invited Article**)

8. G. Soma, W. Yanwachirakul, T. Miyazaki, E. Kato, B. Onodera, R. Tanomura, **T. Fukui**, S. Ishimura, M. Sugiyama, Y. Nakano, and T. Tanemura, "Ultra-broadband surface-

normal coherent optical receiver with nanometallic polarizers," ACS Photonics, vol. 9, no. 8, pp. 2842-2849, 2022.

9. M. Ito, **T. Fukui**, T. Tanemura, and Y. Nakano, "Compact symmetric polarization rotator-splitter on InP," Optics Express, vol. 30, no. 3, pp. 4179-4188, 2022.
10. S. Emara, **T. Fukui**, K. Komatsu, Y. Kohno, R. Tang, T. Tanemura, and Y. Nakano, "Single-pixel imaging using carrier-depletion optical phased array with reduced phase shift requirement," IEEE Photonics Journal, vol. 13, no. 5, 6600105.
11. S. Emara, **T. Fukui**, K. Komatsu, Y. Kohno, T. Tanemura, and Y. Nakano, "Optimization based on the condition number of the speckle patterns in single-pixel imaging using optical phased arrays," Japanese Journal of Applied Physics, vol. 60, no. 7, 072006, 2021.
12. M. Ito, K. Okawa, T. Suganuma, **T. Fukui**, E. Kato, T. Tanemura, and Y. Nakano, "Efficient InGaAsP MQW-based polarization controller without active-passive integration," Optics Express, vol. 19, no. 7, pp. 10538-10545, 2021.
13. G. Soma, S. Ishimura, R. Tanomura, **T. Fukui**, M. Ito, Y. Nakano, and T. Tanemura, "Integrated dual-polarization coherent receiver without polarization splitter-rotator," Optics Express, vol. 29, no. 2, pp. 1711-1721, 2021.
14. K. Toprasertpong, K. Tahara, **T. Fukui**, Z. Lin, K. Watanabe, M. Takenaka, and S. Takagi, "Improved MFIS interface properties in HfO2-based ferroelectric FETs by low-temperature annealing," IEEE Electron Device Letters, vol. 41, no. 10, pp. 1588-1591, 2020.
15. D.-H. Ahn, S. Yoon, K. Kato, **T. Fukui**, M. Takenaka and S. Takagi, "Effects of ZrO_2/Al_2O_3 gate-stack on the performance of planar-type InGaAs TFET," IEEE Transactions on Electron Devices, vol. 66, no. 4, pp. 1862-1867, 2019.

International Conferences

1. ○**T. Fukui**, K. Sumita, M. Takenaka, S. Takagi, Y. Nakano, and T. Tanemura, "Numerical investigation of high-speed surface-normal modulator using InP high-contrast grating," International Semiconductor Laser Conference (ISLC'22), TuP-40, Matsue, Oct. 2022. (Refereed / Poster)

2.* ○**T. Fukui**, K. Komatsu, Y. Nakano, and T. Tanemura, "Scalability of non-redundant optical phased array for speckle-based single-pixel imaging," OptoElectronics and Communication Conference (OECC'22), TuE3-2, Toyama, Jul. 2022. (Refereed / Oral)

3.* ○**T. Fukui**, R. Tanomura, K. Komatsu, D. Yamashita, S. Takahashi, Y. Nakano, and T. Tanemura, "Ultra-high-resolution beam steering using non-redundant optical phased

array,” Conference on Lasers and Electro-Optics (CLEO’22), STh4J.2, San Jose, May 2022. (Refereed / Oral)

4. ○**T. Fukui**, Y. Nakano, and T. Tanemura, “Resolution enhancement of optical-phased-array-based single-pixel imaging by using a multimode fiber,” Conference on Lasers and Electro-Optics (CLEO’20), SM1O.7, San Jose, May 2020. (Refereed / Oral)
5. ○**T. Fukui**, Y. Kohno, R. Tang, Y. Nakano, and T. Tanemura, “Single-pixel imaging through multimode fiber using silicon optical phased array chip,” Optical Fiber Communication Conference (OFC’20), M2C.2, San Diego, Mar. 2020 (Refereed / Oral / **Top-scored paper**).
6. ○**T. Fukui**, Y. Nakano, and T. Tanemura, “On ghost imaging using multimode fiber and integrated optical phased array,” OptoElectronics and Communication Conference (OECC’19), WC3-4, Hakata, Jul. 2019. (Refereed / Oral)
7. ○G. Soma, W. Yanwachirakul, T. Miyazaki, E. Kato, B. Onodera, R. Tanomura, **T. Fukui**, S. Ishimura, M. Sugiyama, Y. Nakano, and T. Tanemura, “Compact surface-normal coherent optical receiver with wire-grid polarizers,” Conference on Lasers and Electro-Optics (CLEO’23). (submitted)
8. ○T. Tanemura, S. Ishimura, **T. Fukui**, R. Tanomura, G. Soma, and Y. Nakano, “Photonic integrated self-coherent transceivers for beyond-Tbps short-reach links,” International Symposium on Photonics and Electronics Convergence (ISPEC’22), Dec. 2022. (**Invited Talk**)
9. ○S. Maeda, **T. Fukui**, G. Soma, T. Tanemura, and Y. Nakano, “Design and characterization of multi-wavelength coherent receiver circuit,” International Symposium on Photonics and Electronics Convergence (ISPEC’22), Dec. 2022. (Refereed / Poster)
10. ○H. Miyano, **T. Fukui**, G. Soma, A. Otomo, T. Tanemura, and Y. Nakano, “Dimerized plasmonic-organic gratings for high-speed metasurface modulators,” Photonics in Switching and Computing (PSC’22), TuD3-2, Toyama, Jul. 2022. (Refereed / Oral)
11. ○Y. Suzuki, A. Elfiqi, **T. Fukui**, M. Ito, T. Tanemura, and Y. Nakano, “V-groove-assisted polarization splitter-rotator on multi-micron silicon photonics,” Photonics in Switching and Computing (PSC’22), MD2-6, Toyama, Jul. 2022. (Refereed / Oral)
12. J. Liu, Y. Nomoto, A. Otomo, **T. Fukui**, Y. Nakano, and ○T. Tanemura, “Experimental demonstration of TM-mode silicon high-contrast grating modulator with electro-opitc polymer,” Photonics in Switching and Computing (PSC’22), TuD3-3, Toyama, Jul. 2022. (Refereed / Oral)
13.* ○S. Takahashi, **T. Fukui**, R. Tanomura, Y. Taguchi, Y. Ozeki, Y. Nakano, and T. Tanemura, “Characterization of Silicon Optical Phased Array with On-Chip Phase Monitors,” Photonics in Switching and Computing (PSC’22), MD2-2, Toyama, Jul. 2022. (Refereed / Oral / **Best Paper Award**)

14. ○S. Ishimura, **T. Fukui**, R. Tanomura, G. Soma, Y. Nakano, and T. Tanemura, “64-QAM self-coherent transmission using symmetric silicon photonic Stokes-vector receiver,” Optical Fiber and Communication Conference (OFC’22), M4J.6, San Diego, Mar. 2022. (Refereed / Oral)
15. M. Ito, **T. Fukui**, ○T. Tanemura, and Y. Nakano, “Mode-evolution-based symmetrical polarization splitter-rotator on monolithic InP platform,” European Conference on Optical Communication (ECOC’21) , We4D.4, Online, Sep. 2021. (Referred / Oral)
16. ○S. Emara, **T. Fukui**, K. Komatsu, Y. Kohno, Y. Nakano, and T. Tanemura “Effect of limited phase shift on single-pixel imaging using carrier-depletion silicon photonic phased array,” Imaging and Applied Optics Congress, Tu2F.4, Online, Jul. 2021. (Refereed / Oral)
17. ○G. Soma, S. Ishimura, R. Tanomura, **T. Fukui**, M. Ito, Y. Nakano, and T. Tanemura, “Polarization-splitter-rotator-free dual-polarization coherent receiver with a single optical hybrid,” Conference on Lasers and Electro-Optics (CLEO’21), STu2B.4, Online, May 2021. (Refereed / Oral)
18. ○T. Tanemura, **T. Fukui**, K. Komatsu, Y. Kohno, and Y. Nakano, “Single-pixel imaging using optical phased array chip,” Asia Communications and Photonics Conference (ACP’20), S4B.6, Beijing, China, Oct. 2020. (**Invited talk**)
19. ○K. Toprasertpong, K. Tahara, **T. Fukui**, Z. Lin, K. Watanabe, M. Takenaka, and S. Takagi, “Critical Impact of Ferroelectric-Phase Formation Annealing on MFIS Interface of HfO2-Based Si FeFETs,” 2020 International Conference on Solidstate Devices and Materials (SSDM’20), A-1-02, Sep. 2020 (Refereed / Oral).
20. ○T. Tanemura, **T. Fukui**, Y. Kohno, and Y. Nakano, “Single-pixel speckle imaging using integrated optical phased array,”IEEE Photonics Society Summer Topical Meeting (SUM’20), MB2.1, Cabo San Lucas, Jul. 2020. (**Invited talk**)
21. ○D.-H. Ahn, S.-H. Yoon, K. Kato, **T. Fukui**, M. Takenaka, and S. Takagi, “EOT scaling of planar-type InGaAs TFETs by using W/ZrO2/Al2O3 gate stacks,” Semiconductor Interface Specialists Conference (SISC’18), 8.4, San Diego, Dec. 2018 (Refereed / Oral).

Workshops, Symposiums, and Domestic Conferences

1.* ○**福井太一郎**, 田之村亮汰, 小松憲人, 山下大之, 高橋俊, 中野義昭, 種村拓夫, “非冗長光フェーズドアレイを用いた高分解能ビーム偏向,” 応用物理学会春季学術講演会, 東京, Mar. 2023. （**招待講演**）
2. ○**福井太一郎**, 隅田圭, 竹中充, 高木信一, 中野義昭, 種村拓夫, “InP 高屈折率差格子と電気光学ポリマーを用いた垂直入射型光変調器の提案と数値解析,” 応用物理学

会秋季学術講演会, 22a-C101-4, 仙台, Sep. 2022. （査読なし・口頭発表）

3. ○**T. Fukui**, Y. Kohno, R. Tang, Y. Nakano, and T. Tanemura, “Single-pixel imaging using an integrated optical phased array and a multimode fiber,” IEEE Photonics Journal Club, Online, Jun. 2022. (**Invited Talk**)
4.* ○**福井太一郎**, 田之村亮汰, 小松憲人, 山下大之, 高橋俊, 中野義昭, 種村拓夫, “非冗長光フェーズドアレイによる高分解能光掃引,” 応用物理学会春季学術講演会, 東京, 22p-E303-1, Mar. 2022. （**招待講演**）
5.* ○**T. Fukui**, Y. Nakano, and T. Tanemura, “Optical phased arrays for high-resolution imaging,” Tsinghua University - The University of Tokyo Joint Symposium 2021, Materials and Devices Workshop, Online, Dec 2021. （査読なし・口頭発表）
6.* ○**福井太一郎**, 田之村亮汰, 小松憲人, 山下大之, 高橋俊, 中野義昭, 種村拓夫, “非冗長光フェーズドアレイによる超高分解能光偏向：提案と実証,” 応用物理学会秋季学術講演会, Online, Sep. 2021. （査読なし・口頭発表）
7. ○**福井太一郎**, 中野義昭, 種村拓夫, “多モードファイバと光フェーズドアレイを用いた単一ピクセルイメージングの分解能限界,” 応用物理学会春季学術講演会, 19p-Z28-2, Mar. 2021. （査読なし・口頭発表）
8. ○**T. Fukui**, Y. Nakano, and T. Tanemura, “Resolution analysis of imaging method using multimode fiber and optical phased array,” Photonic Device Workshop (PDW’19), Tokyo, Dec. 2019. （査読なし・ポスター発表）
9. ○**福井太一郎**, 河野佑亮, 唐睿, 中野義昭, 種村拓夫, “多モードファイバと光フェーズドアレイを用いた単一ピクセルイメージングの実証,” 応用物理学会秋季学術講演会, 19p-E319-4, 札幌, Sep. 2019. （査読なし・口頭発表）
10. ○**T. Fukui**, Y. Nakano, and T. Tanemura, “Analysis of integrated optical phased array for imaging through multimode fiber,” Tsinghua University - The University of Tokyo Joint Symposium 2019, Materials and Devices Workshop, Beijing, China, May 2019. （査読なし・ポスター発表）
11. ○**福井太一郎**, 中野義昭, 種村拓夫, “光フェーズドアレイと多モードファイバによる高速イメージングの検討,” 電子情報通信学会光エレクトロニクス研究会, 博多, Feb. 2019. （査読なし・口頭発表）
12. ○ 宮野広基, **福井太一郎**, 相馬豪, 李広鵬, 大友明, 種村拓夫, 中野義昭, “二量化高屈折率差格子と電気光学ポリマーを用いた垂直入射光変調器の提案と検証,” 応用物理学会春季学術講演会, 東京, Mar. 2023. （査読なし・口頭発表）
13. ○ 前田隼太郎, **福井太一郎**, 相馬豪, 種村拓夫, 中野義昭, “局発コム光源を用いた多波長コヒーレント受信回路の実験的検証,” 電子情報通信学会総合大会, Mar. 2023. （査読なし・口頭発表）
14. ○H. Miyano, **T. Fukui**, G. Soma, A. Otomo, S. Ishimura, T. Tanemura, and Y. Nakano, “Demonstration of surface-normal high-speed plasmonic modulator with electro-optic

polymer,” Photonic Device Workshop 2022, Dec. 2022. （査読なし・ポスター発表）

15. ○H. Miyano, **T. Fukui**, G. Soma, A. Otomo, S. Ishimura, T. Tanemura, and Y. Nakano, “Dimerized plasmonic grating with EO-polymer for high-speed metasurface modulator,” Tsinghua University - The University of Tokyo Joint Symposium 2022, Advanced Materials and Devices Research, Online, Dec 2022. （査読なし・口頭発表）
16. ○ 蟻生高人, 宮野広基, **福井太一郎**, 野本佳朗, 種村拓夫, 中野義昭, “電気光学ポリマーを用いた裏面垂直入射型プラズモニック光変調器の提案と解析,” 応用物理学会秋季学術講演会, 22p-A101-7, 仙台, Sep. 2022.（査読なし・口頭発表）
17. ○ 宮野広基, **福井太一郎**, 相馬豪, 大友明, 種村拓夫, 中野義昭, “二量化プラズモニック格子を用いた電気光学ポリマー垂直入射型変調器の提案,” 応用物理学会秋季学術講演会, 22p-A101-6, 仙台, Sep. 2022.（査読なし・口頭発表）
18. ○ 前田隼太郎, **福井太一郎**, 相馬豪, 種村拓夫, 中野義昭, “シリコンフォトニクス多波長セルフコヒーレント光受信器の検討,” 電子情報通信学会光エレクトロニクス研究会 Jun. 2022.（査読なし・ポスター発表）
19. ○ 種村拓夫, 小松憲人, **福井太一郎**, 中野義昭, “高分解イメージングに向けた光集積フェーズドアレイ,” 応用物理学会微小光学研究会, May 2022.（**招待講演**）
20. ○ 相馬豪, ヤンワチラークンワラーコン, 田之村亮汰, 福井太一郎, 石村昇太, 加藤豪作, 杉山正和, 中野義昭, 種村拓夫 “垂直入射型コヒーレント光受信器の実証,” 電子情報通信学会総合大会, C-3/4-22, Mar. 2022. （査読なし・口頭発表）
21. ○J. Liu, Y. Nomoto, G. Soma, **T. Fukui**, Y. Nakano, and T. Tanemura, “Numerical Investigation of efficient TM-mode normal incident modulator with high-contrast grating and electro-optic polymer,” Photonic Device Workshop 2021, Dec. 2021. （査読なし・ポスター発表）
22. ○Q. Liu, K. Komatsu, **T. Fukui**, T. Tanemura, and Y. Nakano, “Optical phased array with pulse-driven SOAs for Time-of-Flight LiDAR system,” 電子情報通信学会ソサイエティ大会, Sep. 2021. （査読なし・口頭発表）
23. ○ 鈴木優斗, エルフィキアブドラジズ, **福井太一郎**, 伊藤まいこ, 種村拓夫, 中野義昭, “厚膜シリコンフォトニクス偏波回転分離器の提案と解析,” 電子情報通信学会ソサイエティ大会, Sep. 2021. （査読なし・口頭発表）
24.* ○ 高橋俊, **福井太一郎**, 田之村亮汰, 田口富隆, 小関泰之, 中野義昭, 種村拓夫, “位相モニタ集積光フェーズドアレイ素子の検証,” 応用物理学会秋季学術講演会, Sep. 2021. （査読なし・口頭発表）
25. ○ 宮野広基, 相馬豪, **福井太一郎**, 野本佳朗, 種村拓夫, 中野義昭, “薄膜ニオブ酸リチウム基板を用いたプラズモニック垂直入射型光変調器の提案,” 応用物理学会秋季学術講演会, Sep. 2021. （査読なし・口頭発表）
26. ○ 相馬豪, 石村昇太, 田之村亮太, **福井太一郎**, 伊藤まいこ, 中野義昭, 種村拓夫, “偏波分離回転器フリー偏波多重コヒーレント光集積受信器,” 電子情報通信学会総合

大会, C-3/4-16, Mar. 2021. （査読なし・口頭発表）

27. ○ 梅崎敏和, 小松憲人, **福井太一郎**, 中野義昭, 種村拓夫, “単一ピクセルイメージングに適した高効率駆動型光集積フェーズドアレイ素子の解析,” 応用物理学会春季学術講演会, 19p-Z22-12, Mar. 2021. （査読なし・口頭発表）
28. ○ トープラサートポンカシディット, 田原建人, **福井太一郎**, 林早ヤン, 渡辺耕坪, 竹中充, 高木 信一, “HfO_2 系 FeFET における結晶化アニール温度と Si 界面特性のトレードオフ,” 応用物理学会春季学術講演会, 16p-Z26-4, Mar. 2021. （査読なし・口頭発表）
29. ○ 土屋里穂子, ヤンワチラークンワラーコン, 加藤豪作, 田之村亮汰, **福井太一郎**, 種村拓夫, 中野義昭, “1 μm 帯イメージングに向けた GaAs/InGaP 光集積フェーズドアレイ素子の設計,” Photonic Device Workshop 2020, P-(21), Nov. 2020. （査読なし・ポスター発表）
30. ○ 宮崎俊輝, 小笠原誠, 張家キ, **福井太一郎**, 大友明, 中野義昭, 種村拓夫, “電気光学ポリマーを用いた垂直入射型光位相変調器の設計と試作,” Photonic Device Workshop 2020, P-(20), Nov. 2020. （査読なし・ポスター発表）
31. ○ 種村拓夫, **福井太一郎**, 河野佑亮, 小松憲人, 中野義昭, “光集積フェーズドアレイによる単一ピクセルイメージング,” 電子情報通信学会ソサイエティ大会, Sep. 2020. （招待講演）
32. ○T. Tanemura, Y. Kohno, **T. Fukui**, and Yoshiaki Nakano, “Single-pixel imaging using integrated optical phased arrays,”Photonic Device Workshop 2019, (13), Tokyo, Dec. 2019. （**招待講演**）
33. ○S. Onoduka, **T. Fukui**, T. Tanemura, and Y. Nakano, “Design of semiconductor optical amplifier for high power optical phased array,” Photonic Device Workshop 2019, P-(2), Tokyo, Dec. 2019. （査読なし・ポスター発表）
34. ○S. Emara, **T. Fukui**, T. Tanemura, and Y. Nakano, “Effect of limited phase shift on single-pixel imaging using optical phased array,” Photonic Device Workshop 2019, P-(24), Tokyo, Dec. 2019. （査読なし・ポスター発表）
35. ○ トープラサートポンカシディット, 田原健人, **福井太一郎**, 竹中充, 高木信一, “TiN/$Hf_{0.5}Zr_{0.5}O_2$/Si MFS キャパシタの電気特性に与える基板タイプの影響,” 応用物理学会秋季学術講演会, 19a-E305-10, 札幌, Sep. 2019. （査読なし・口頭発表）
36. ○C. Liao, K. Toprasertpong, **T. Fukui**, M. Takenaka, Shinichi Takagi, “Evaluation of surface potential of ferroelectric-gate MOS capacitors by C-V analyses,” 応用物理学会秋季学術講演会, 19a-E305-12, 札幌, Sep. 2019. （査読なし・口頭発表）
37. ○ R. Tsuchiya, **T. Fukui**, R. Tanomura, T. Tanemura, and Y. Nakano, “Design and Fabrication of Optical Phased-Array Beam-Steering Device Coupled with 3D Waveguide,”Tsinghua University - The University of Tokyo Joint Symposium 2019, Materials and Devices Workshop, Beijing, China, May 2019. （査読なし・ポスター発表）

38. ○ 土屋里穂子, **福井太一郎**, 田之村亮汰, 種村拓夫, 中野義昭, “三次元導波路を結合した光集積フェーズドアレイ型ビーム走査素子の設計と試作,” 電子情報通信学会光エレクトロニクス研究会, 伊香保, Apr. 2019. （査読なし・ポスター発表）
39. ○ 梅崎敏和, **福井太一郎**, 田之村亮汰, 山下大之, 河野佑亮, 中野義昭, 種村拓夫, “深層学習による光集積フェーズドアレイ素子の駆動条件最適化手法の検討,” 電子情報通信学会光エレクトロニクス研究会, 伊香保, Apr. 2019. （査読なし・ポスター発表）
40. ○ 安大煥, 尹尚希, 加藤公彦, **福井太一郎**, 竹中充 , 高木信一, “ZrO_2 による EOT スケーリングを用いた Planar-type 量子井戸 InGaAs TFET の性能向上,” 応用物理学会春季学術講演会, 9p-S221-1, Mar. 2019. （**招待講演**）
41. ○ 安大煥, 尹尚希, 加藤公彦, **福井太一郎**, 竹中充, 高木信一, “ZrO_2 ゲートスタックによる Planar-type InGaAs TFET の Sub-60mV/dec 特性の実現,” 応用物理学会秋季学術講演会, 21a-CE-4, 名古屋, Sep. 2018. （査読なし・口頭発表）

Patents

1. 宮野広基, 相馬豪, **福井太一郎**, 種村拓夫, 野本佳朗, “プラズモン型 LN 光変調器,” 特願 2021-133941, 2021 年 8 月 19 日出願.
2. 鈴木優斗, エルフィキアブドラジズ, **福井太一郎**, 伊藤まいこ, 中野義昭, 種村拓夫, “偏波分離回転器”, 特願 2021-140541, 2021 年 7 月 29 日.
3. 相馬豪, **福井太一郎**, 種村拓夫, 田之村亮汰, 石村昇太, 中野義昭, “コヒーレント光受信器,” 特願 2020-115195, 2020 年 7 月 2 日出願.
4. 石村昇太, 種村拓夫, **福井太一郎**, 田之村亮汰, “光送信装置及び光通信システム,” 特願 2019-184056, 2019 年 10 月 4 日出願.
5. 石村昇太, 種村拓夫, **福井太一郎**, 田之村亮汰, “光受信装置,” 特願 2019-184057, 2019 年 10 月 4 日出願.

6.* **福井太一郎**, 種村拓夫, 中野義昭, 山下大之, 田之村亮汰, “光照射装置、イメージング装置、およびレーザー加工装置,” 特願 2019-000901, 2019 年 1 月 7 日出願.

Awards

1.* **フォトニクス奨励賞**, 応用物理学会フォトニクス分科会, Mar. 2023.
2.* **Best paper award**, Photonics in Switching and Computing (PSC’22), Jul. 2022. (Coauthored, 2nd Author)
3.* **応用物理学会講演奨励賞**, 応用物理学会, Nov. 2021.
4. **Honorable mention award**, “Corning Outstanding Student Paper Competition” in Optical Fiber Communication Conference (OFC’20), Mar 2020.
5. **優秀修士論文賞**, 東京大学工学系研究科電気系工学専攻, Mar 2020.

6. **Best Student Poster Award**, Photonic Device Workshop 2019.

References

[1] Y. Li and J. Ibanez-Guzman, "Lidar for autonomous driving: The principles, challenges, and trends for automotive lidar and perception systems," *IEEE Signal Process. Mag.*, vol. 37, no. 4, pp. 50–61, Jul. 2020.

[2] Japan Cabinet Office, "Society 5.0," https://www8.cao.go.jp/cstp/society5_0/.

[3] International Society of Automation, "What is industry 4.0?" https://blog.isa.org/what-is-industry-40.

[4] E. O. Potma and X. S. Xie, "CARS microscopy for biology and medicine," *Opt. Photonics News*, vol. 15, no. 11, p. 40, Nov. 2004.

[5] J. W. Lichtman and J.-A. Conchello, "Fluorescence microscopy," *Nat. Methods*, vol. 2, no. 12, pp. 910–919, Dec. 2005.

[6] Y. Ozeki, W. Umemura, Y. Otsuka, S. Satoh, H. Hashimoto, K. Sumimura, N. Nishizawa, K. Fukui, and K. Itoh, "High-speed molecular spectral imaging of tissue with stimulated raman scattering," *Nat. Photonics*, vol. 6, no. 12, pp. 845–851, Nov. 2012.

[7] J. Xiong, E.-L. Hsiang, Z. He, T. Zhan, and S.-T. Wu, "Augmented reality and virtual reality displays: emerging technologies and future perspectives," *Light Sci Appl*, vol. 10, no. 1, p. 216, Oct. 2021.

[8] Y. Kaymak, R. Rojas-Cessa, J. Feng, N. Ansari, M. Zhou, and T. Zhang, "A survey on acquisition, tracking, and pointing mechanisms for mobile Free-Space optical communications," *IEEE Communications Surveys & Tutorials*, vol. 20, no. 2, pp. 1104–1123, 2018.

[9] S. T. S. Holmström, U. Baran, and H. Urey, "MEMS laser scanners: A review," *J. Microelectromech. Syst.*, vol. 23, no. 2, pp. 259–275, Apr. 2014.

[10] Y. Wang, G. Zhou, X. Zhang, K. Kwon, P.-A. Blanche, N. Triesault, K.-S. Yu, and M. C. Wu, "2D broadband beamsteering with large-scale MEMS optical phased array," *Optica*, vol. 6, no. 5, pp. 557–562, May 2019.

[11] X. Zhang, K. Kwon, J. Henriksson, J. Luo, and M. C. Wu, "A large-scale microelectromechanical-systems-based silicon photonics LiDAR," *Nature*, vol. 603,

no. 7900, pp. 253–258, Mar. 2022.

[12] R. G. Hunsperger, *Integrated Optics*. Springer New York, 1995.

[13] C. R. Pollock and M. Lipson, *Integrated Photonics*. Springer US, 2003.

[14] L. A. Coldren, S. W. Corzine, and M. L. Mashanovitch, *Diode Lasers and Photonic Integrated Circuits*. John Wiley & Sons, Mar. 2012.

[15] B. Jalali and S. Fathpour, "Silicon photonics," *J. Lightwave Technol.*, vol. 24, no. 12, pp. 4600–4615, Dec. 2006.

[16] G. Roelkens, L. Liu, D. Liang, R. Jones, A. Fang, B. Koch, and J. Bowers, "III-V/silicon photonics for on-chip and intra-chip optical interconnects," *Laser Photonics Rev.*, vol. 4, no. 6, pp. 751–779, 2010.

[17] C. Li, X. Cao, K. Wu, X. Li, and J. Chen, "Lens-based integrated 2D beam-steering device with defocusing approach and broadband pulse operation for lidar application," *Opt. Express*, vol. 27, no. 23, pp. 32 970–32 983, Nov. 2019.

[18] D. Inoue, T. Ichikawa, A. Kawasaki, and T. Yamashita, "Demonstration of a new optical scanner using silicon photonics integrated circuit," *Opt. Express*, vol. 27, no. 3, pp. 2499–2508, Feb. 2019.

[19] C. Rogers, A. Y. Piggott, D. J. Thomson, R. F. Wiser, I. E. Opris, S. A. Fortune, A. J. Compston, A. Gondarenko, F. Meng, X. Chen, G. T. Reed, and R. Nicolaescu, "A universal 3D imaging sensor on a silicon photonics platform," *Nature*, vol. 590, no. 7845, pp. 256–261, Feb. 2021.

[20] X. Gu, T. Shimada, and F. Koyama, "Giant and high-resolution beam steering using slow-light waveguide amplifier," *Opt. Express*, vol. 19, no. 23, pp. 22 675–22 683, Nov. 2011.

[21] H. Ito, Y. Kusunoki, J. Maeda, D. Akiyama, N. Kodama, H. Abe, R. Tetsuya, and T. Baba, "Wide beam steering by slow-light waveguide gratings and a prism lens," *Optica*, vol. 7, no. 1, pp. 47–52, Jan. 2020.

[22] S. Hu, A. Hassan, X. Gu, M. Nakahama, S. Shinada, and F. Koyama, "Surface grating VCSEL-integrated amplifier/beam scanner with high power and single mode operation," *Appl. Phys. Express*, May 2021.

[23] A. M. A. Hassan, X. Gu, M. Nakahama, S. Shinada, M. Ahmed, and F. Koyama, "High power surface grating slow-light VCSEL," *Appl. Phys. Express*, vol. 14, no. 9, p. 092006, Aug. 2021.

[24] T. Tamanuki, H. Ito, and T. Baba, "Thermo-optic beam scanner employing silicon photonic crystal slow-light waveguides," *J. Lightwave Technol.*, vol. 39, no. 4, pp. 904–911, Feb. 2021.

[25] S. Suyama, H. Ito, R. Kurahashi, H. Abe, and T. Baba, "Doppler velocimeter and vibrometer FMCW LiDAR with si photonic crystal beam scanner," *Opt. Express*, vol. 29,

no. 19, pp. 30 727–30 734, Sep. 2021.

[26] T. Baba, T. Tamanuki, H. Ito, M. Kamata, R. Tetsuya, S. Suyama, H. Abe, and R. Kurahashi, "Silicon photonics FMCW LiDAR chip with a slow-light grating beam scanner," *IEEE J. Sel. Top. Quantum Electron.*, vol. 28, no. 5, p. 8300208, Sep. 2022.

[27] R. Li, S. Hu, X. Gu, and F. Koyama, "Solid-state slow-light beam scanner with ultra-large field of view and high resolution," *J. Lightwave Technol.*, vol. 40, no. 6, pp. 1855–1861, Mar. 2022.

[28] M. J. R. Heck, "Highly integrated optical phased arrays: photonic integrated circuits for optical beam shaping and beam steering," *Nanophotonics*, vol. 6, no. 1, pp. 93–107, Jan. 2017.

[29] H. Hashemi, "A review of semiconductor-based monolithic optical phased array architectures," *IEEE Open Journal of the Solid-State Circuits Society*, vol. 1, pp. 222–234, 2021.

[30] S. Lin, Y. Chen, and Z. J. Wong, "High-performance optical beam steering with nanophotonics," *Nanophotonics*, vol. 11, no. 11, pp. 2617–2638, Jun. 2022.

[31] L. B. Soldano and E. C. M. Pennings, "Optical multi-mode interference devices based on self-imaging: principles and applications," *J. Lightwave Technol.*, vol. 13, no. 4, pp. 615–627, Apr. 1995.

[32] C. Dragone, "Efficient $N \times N$ star couplers using fourier optics," *J. Lightwave Technol.*, vol. 7, no. 3, pp. 479–489, Mar. 1989.

[33] J. W. Goodman, *Introduction to Fourier Optics*. Macmillan Learning, 1996.

[34] D. N. Hutchison, J. Sun, J. K. Doylend, R. Kumar, J. Heck, W. Kim, C. T. Phare, A. Feshali, and H. Rong, "High-resolution aliasing-free optical beam steering," *Optica*, vol. 3, no. 8, pp. 887–890, Aug. 2016.

[35] Y. Li, B. Chen, Q. Na, Q. Xie, M. Tao, L. Zhang, Z. Zhi, Y. Li, X. Liu, X. Luo, G. Lo, F. Gao, X. Li, and J. Song, "Wide-steering-angle high-resolution optical phased array," *Photonics Res.*, vol. 9, no. 12, p. 2511, Dec. 2021.

[36] W. Xu, L. Zhou, L. Lu, and J. Chen, "Aliasing-free optical phased array beam-steering with a plateau envelope," *Opt. Express*, vol. 27, no. 3, pp. 3354–3368, Feb. 2019.

[37] C. T. Phare, M. C. Shin, J. Sharma, S. Ahasan, H. Krishnaswamy, and M. Lipson, "Silicon optical phased array with grating lobe-free beam formation over 180 degree field of view," in *Conference on Lasers and Electro-Optics*, May 2018, p. SM3I.2.

[38] Y. Liu and H. Hu, "Silicon optical phased array with a 180-degree field of view for 2D optical beam steering," *Optica*, vol. 9, no. 8, p. 903, Aug. 2022.

[39] M. R. Kossey, C. Rizk, and A. C. Foster, "End-fire silicon optical phased array with half-wavelength spacing," *APL Photonics*, vol. 3, no. 1, p. 011301, Jan. 2018.

[40] M. Zadka, Y.-C. Chang, A. Mohanty, C. T. Phare, S. P. Roberts, and M. Lipson, "On-

chip platform for a phased array with minimal beam divergence and wide field-of-view," *Opt. Express*, vol. 26, no. 3, pp. 2528–2534, Feb. 2018.

[41] S. Khajavi, D. Melati, P. Cheben, J. H. Schmid, Q. Liu, D. X. Xu, and W. N. Ye, "Compact and highly-efficient broadband surface grating antenna on a silicon platform," *Opt. Express*, vol. 29, no. 5, pp. 7003–7014, Mar. 2021.

[42] Y. Ninomiya, "Ultrahigh resolving electrooptic prism array light deflectors," *IEEE J. Quantum Electron.*, vol. 9, no. 8, pp. 791–795, Aug. 1973.

[43] H. Sasaki and R. M. de La Rue, "Electro-optic y-junction modulator/switch," *Electron. Lett.*, vol. 12, no. 18, pp. 459–460, Sep. 1976.

[44] D. R. Wight, J. M. Heaton, B. T. Hughes, J. C. H. Birbeck, K. P. Hilton, and D. J. Taylor, "Novel phased array optical scanning device implemented using GaAs/AlGaAs technology," *Appl. Phys. Lett.*, vol. 59, no. 8, pp. 899–901, Aug. 1991.

[45] J. M. Heaton, D. R. Wight, J. T. Parker, B. T. Hughes, J. C. H. Birbeck, and K. P. Hilton, "A phased array optical scanning (PHAROS) device used as a 1-to-9 way switch," *IEEE J. Quantum Electron.*, vol. 28, no. 3, pp. 678–685, Mar. 1992.

[46] K. Moriki, Y. Ohnishi, H. Katoh, T. Inoue, T. Sakaguchi, and T. H. Iga, "GaAlAs/GaAs optical beam scanner using phased array waveguides," *Jpn. J. Appl. Phys.*, vol. 31, no. 3R, p. 807, Mar. 1992.

[47] E. Fluck, F. Horst, B. J. Offrein, R. Germann, W. M. Salemink, and G.-L. Bona, "Compact versatile thermooptical space switch based on beam steering by a waveguide array," *IEEE Photonics Technol. Lett.*, vol. 11, no. 11, pp. 1399–1401, Nov. 1999.

[48] T. Tanemura, M. Takenaka, A. Al Amin, K. Takeda, T. Shioda, M. Sugiyama, and Y. Nakano, "InP–InGaAsP integrated 1×5 optical switch using arrayed phase shifters," *IEEE Photonics Technol. Lett.*, vol. 20, no. 12, pp. 1063–1065, Jun. 2008.

[49] I. M. Soganci, T. Tanemura, K. A. Williams, N. Calabretta, T. de Vries, E. Smalbrugge, M. K. Smit, H. J. S. Dorren, and Y. Nakano, "Monolithically integrated InP 1×16 optical switch with wavelength-insensitive operation," *IEEE Photonics Technol. Lett.*, vol. 22, no. 3, pp. 143–145, Feb. 2010.

[50] I. M. Soganci, T. Tanemura, K. Takeda, M. Zaitsu, M. Takenaka, and Y. Nakano, "Monolithic InP 100-port photonic switch," in *36th European Conference and Exhibition on Optical Communication*, Sep. 2010, p. PD1.5.

[51] T. Tanemura, I. M. Soganci, T. Oyama, T. Ohyama, S. Mino, K. A. Williams, N. Calabretta, H. J. S. Dorren, and Y. Nakano, "Large-capacity compact optical buffer based on inp integrated phased-array switch and coiled fiber delay lines," *J. Lightwave Technol.*, vol. 29, no. 4, pp. 396–402, Feb. 2011.

[52] M.-J. Kwack, T. Tanemura, A. Higo, and Y. Nakano, "Monolithic InP strictly non-blocking 8×8 switch for high-speed WDM optical interconnection," *Opt. Express*,

vol. 20, no. 27, pp. 28 734–28 741, Dec. 2012.

[53] I. M. Soganci, T. Tanemura, and Y. Nakano, "Integrated phased-array switches for large-scale photonic routing on chip," *Laser Photon. Rev.*, vol. 6, no. 4, pp. 549–563, Jul. 2012.

[54] T. Tanemura, L. Langouche, and Y. Nakano, "Strictly non-blocking 8×8 silicon photonic switch based on optical phased array," in *2015 European Conference on Optical Communication (ECOC)*, Sep. 2015, pp. 1–3.

[55] T. Tanemura and Y. Nakano, "Design and scalability analysis of optical phased-array 1 $\times N$ switch on planar lightwave circuit," *IEICE Electronics Express*, vol. 5, no. 16, pp. 603–609, 2008.

[56] K. Van Acoleyen, W. Bogaerts, J. Jagerska, N. Le Thomas, R. Houdre, and R. Baets, "Off-chip beam steering with a one-dimensional optical phased array on silicon-on-insulator," *Opt. Lett.*, vol. 34, no. 9, pp. 1477–1479, May 2009.

[57] K. Van Acoleyen, H. Rogier, and R. Baets, "Two-dimensional optical phased array antenna on silicon-on-insulator," *Opt. Express*, vol. 18, no. 13, pp. 13 655–13 660, Jun. 2010.

[58] J. K. Doylend, M. J. R. Heck, J. T. Bovington, J. D. Peters, L. A. Coldren, and J. E. Bowers, "Two-dimensional free-space beam steering with an optical phased array on silicon-on-insulator," *Opt. Express*, vol. 19, no. 22, pp. 21 595–21 604, Oct. 2011.

[59] H. Abediasl and H. Hashemi, "Monolithic optical phased-array transceiver in a standard SOI CMOS process," *Opt. Express*, vol. 23, no. 5, pp. 6509–6519, Mar. 2015.

[60] S. Chung, H. Abediasl, and H. Hashemi, "A monolithically integrated large-scale optical phased array in silicon-on-insulator CMOS," *IEEE J. Solid-State Circuits*, vol. 53, no. 1, pp. 275–296, Jan. 2018.

[61] T. Kim, P. Bhargava, C. V. Poulton, J. Notaros, A. Yaacobi, E. Timurdogan, C. Baiocco, N. Fahrenkopf, S. Kruger, T. Ngai, Y. Timalsina, M. R. Watts, and V. Stojanović, "A single-chip optical phased array in a wafer-scale silicon photonics/CMOS 3D-integration platform," *IEEE J. Solid-State Circuits*, vol. 54, no. 11, pp. 3061–3074, Nov. 2019.

[62] J. K. Doylend, M. J. R. Heck, J. T. Bovington, J. D. Peters, M. L. Davenport, L. A. Coldren, and J. E. Bowers, "Hybrid III/V silicon photonic source with integrated 1D free-space beam steering," *Opt. Lett.*, vol. 37, no. 20, pp. 4257–4259, Oct. 2012.

[63] J. C. Hulme, J. K. Doylend, M. J. R. Heck, J. D. Peters, M. L. Davenport, J. T. Bovington, L. A. Coldren, and J. E. Bowers, "Fully integrated hybrid silicon two dimensional beam scanner," *Opt. Express*, vol. 23, no. 5, pp. 5861–5874, Mar. 2015.

[64] W. Xie, T. Komljenovic, J. Huang, M. Tran, M. Davenport, A. Torres, P. Pintus, and J. Bowers, "Heterogeneous silicon photonics sensing for autonomous cars," *Opt.*

Express, vol. 27, no. 3, pp. 3642–3663, Feb. 2019.

[65] W. Guo, P. R. A. Binetti, C. Althouse, M. L. Mašanović, H. P. M. M. Ambrosius, L. A. Johansson, and L. A. Coldren, "Two-dimensional optical beam steering with InP-based photonic integrated circuits," *IEEE J. Sel. Top. Quantum Electron.*, vol. 19, no. 4, pp. 6 100 212–6 100 212, Jul. 2013.

[66] J. Zhang, G. Muliuk, J. Juvert, S. Kumari, J. Goyvaerts, B. Haq, C. Op de Beeck, B. Kuyken, G. Morthier, D. Van Thourhout, R. Baets, G. Lepage, P. Verheyen, J. Van Campenhout, A. Gocalinska, J. O'Callaghan, E. Pelucchi, K. Thomas, B. Corbett, A. J. Trindade, and G. Roelkens, "III-V-on-Si photonic integrated circuits realized using micro-transfer-printing," *APL Photonics*, vol. 4, no. 11, p. 110803, Nov. 2019.

[67] C. Xiang, J. Guo, W. Jin, L. Wu, J. Peters, W. Xie, L. Chang, B. Shen, H. Wang, Q.-F. Yang, and Others, "High-performance lasers for fully integrated silicon nitride photonics," *Nat. Commun.*, vol. 12, no. 1, pp. 1–8, 2021.

[68] A. Shams-Ansari, D. Renaud, R. Cheng, L. Shao, L. He, D. Zhu, M. Yu, H. R. Grant, L. Johansson, M. Zhang, and M. Lončar, "Electrically pumped laser transmitter integrated on thin-film lithium niobate," *Optica*, vol. 9, no. 4, p. 408, Apr. 2022.

[69] F. Aflatouni, B. Abiri, A. Rekhi, and A. Hajimiri, "Nanophotonic projection system," *Opt. Express*, vol. 23, no. 16, pp. 21 012–21 022, Aug. 2015.

[70] Y. Hirano, Y. Miyamoto, M. Miura, Y. Motoyama, K. Machida, T. Yamada, A. Otomo, and H. Kikuchi, "High-speed optical-beam scanning by an optical phased array using electro-optic polymer waveguides," *IEEE Photonics J.*, vol. 12, no. 2, p. 6600807, Apr. 2020.

[71] K. Komatsu, Y. Kohno, Y. Nakano, and T. Tanemura, "Large-scale monolithic InP-based optical phased array," *IEEE Photonics Technol. Lett.*, vol. 33, no. 20, pp. 1123–1126, Oct. 2021.

[72] Z. Zhang, H. Yu, Q. Huang, Z. Zhou, B. Chen, T. Dai, H. Qiu, Y. Wang, and J. Yang, "High-speed and low-power silicon optical phased array based on the carrier-depletion mechanism," *IEEE Photonics Technol. Lett.*, vol. 34, no. 5, pp. 271–274, Mar. 2022.

[73] C. V. Poulton, A. Yaacobi, D. B. Cole, M. J. Byrd, M. Raval, D. Vermeulen, and M. R. Watts, "Coherent solid-state lidar with silicon photonic optical phased arrays," *Opt. Lett.*, vol. 42, no. 20, pp. 4091–4094, Oct. 2017.

[74] C. V. Poulton, M. J. Byrd, P. Russo, E. Timurdogan, M. Khandaker, D. Vermeulen, and M. R. Watts, "Long-range LiDAR and free-space data communication with high-performance optical phased arrays," *IEEE J. Sel. Top. Quantum Electron.*, vol. 25, no. 5, p. 7700108, sep 2019.

[75] C. V. Poulton, M. J. Byrd, P. Russo, B. Moss, O. Shatrovoy, M. Khandaker, and M. R. Watts, "Coherent lidar with an 8,192-element optical phased array and driving laser,"

IEEE J. Sel. Top. Quantum Electron., vol. 28, no. 5, p. 6100508, Sep. 2022.

[76] C.-P. Hsu, B. Li, B. Solano-Rivas, A. R. Gohil, P. H. Chan, A. D. Moore, and V. Donzella, "A review and perspective on optical phased array for automotive LiDAR," *IEEE J. Sel. Top. Quantum Electron.*, vol. 27, no. 1, p. 8300416, Jan. 2021.

[77] K. Komatsu, Y. Ozeki, Y. Nakano, and T. Tanemura, "Ghost imaging using integrated optical phased array," in *Optical Fiber Communication Conference*, Mar. 2017, p. Th3H.4.

[78] Y. Kohno, K. Komatsu, R. Tang, Y. Ozeki, Y. Nakano, and T. Tanemura, "Ghost imaging using a large-scale silicon photonic phased array chip," *Opt. Express*, vol. 27, no. 3, pp. 3817–3823, Feb. 2019.

[79] L. Li, W. Chen, X. Zhao, and M. Sun, "Fast optical phased array calibration technique for random phase modulation lidar," *IEEE Photonics J.*, vol. 11, no. 1, p. 6900410, Feb. 2019.

[80] H. A. Clevenson, S. J. Spector, L. Benney, M. G. Moebius, J. Brown, A. Hare, A. Huang, J. Mlynarczyk, C. V. Poulton, E. Hosseini, M. R. Watts, R. Dawson, J. P. Laine, and B. F. Lane, "Incoherent light imaging using an optical phased array," *Appl. Phys. Lett.*, vol. 116, no. 3, p. 031105, Jan. 2020.

[81] T. Fukui, Y. Kohno, R. Tang, Y. Nakano, and T. Tanemura, "Single-pixel imaging using multimode fiber and silicon photonic phased array," *J. Lightwave Technol.*, vol. 39, no. 3, pp. 839–844, Feb. 2021.

[82] T. Fukui, Y. Nakano, and T. Tanemura, "Resolution limit of single-pixel speckle imaging using multimode fiber and optical phased array," *J. Opt. Soc. Am. B*, vol. 38, no. 2, pp. 379–386, Feb. 2021.

[83] S. Emara, T. Fukui, K. Komatsu, Y. Kohno, R. Tang, T. Tanemura, and Y. Nakano, "Single-pixel imaging using carrier-depletion optical phased array with reduced phase shift requirement," *IEEE Photonics J.*, vol. 13, no. 5, p. 6600105, Oct. 2021.

[84] S. Emara, T. Fukui, K. Komatsu, Y. Kohno, T. Tanemura, and Y. Nakano, "Optimization based on the condition number of the speckle patterns in single-pixel imaging using optical phased arrays," *Jpn. J. Appl. Phys.*, vol. 60, no. 7, p. 072006, Jul. 2021.

[85] N. Dostart, B. Zhang, M. Brand, D. Feldkhun, M. Popović, and K. Wagner, "Fourier-basis structured illumination imaging with an array of integrated optical phased arrays," *J. Opt. Soc. Am. A*, vol. 38, no. 10, pp. B19–B28, Oct. 2021.

[86] R. Fatemi, A. Khachaturian, and A. Hajimiri, "A nonuniform sparse 2-D large-FOV optical phased array with a low-power PWM drive," *IEEE J. Solid-State Circuits*, vol. 54, no. 5, pp. 1200–1215, May 2019.

[87] M. Chul Shin, A. Mohanty, K. Watson, G. R. Bhatt, C. T. Phare, S. A. Miller, M. Zadka, B. S. Lee, X. Ji, I. Datta, and M. Lipson, "Chip-scale blue light phased array," *Opt.*

Lett., vol. 45, no. 7, pp. 1934–1937, Apr. 2020.

[88] C. V. Poulton, M. J. Byrd, M. Raval, Z. Su, N. Li, E. Timurdogan, D. Coolbaugh, D. Vermeulen, and M. R. Watts, "Large-scale silicon nitride nanophotonic phased arrays at infrared and visible wavelengths," *Opt. Lett.*, vol. 42, no. 1, pp. 21–24, Jan. 2017.

[89] C. Sun, B. Li, W. Shi, J. Lin, N. Ding, H. K. Tsang, and A. Zhang, "Large-scale and broadband silicon nitride optical phased arrays," *IEEE J. Sel. Top. Quantum Electron.*, vol. 28, no. 6, pp. 1–10, Nov. 2022.

[90] N. A. Tyler, D. Fowler, S. Malhouitre, S. Garcia, P. Grosse, W. Rabaud, and B. Szelag, "SiN integrated optical phased arrays for two-dimensional beam steering at a single near-infrared wavelength," *Opt. Express*, vol. 27, no. 4, pp. 5851–5858, Feb. 2019.

[91] Z. Wang, J. Liao, Y. Sun, X. Han, Y. Cao, and R. Zhao, "Chip scale GaAs optical phased arrays for high speed beam steering," *Appl. Opt.*, vol. 59, no. 27, pp. 8310–8313, Sep. 2020.

[92] W. Zhou, D. Wu, Q.-Y. Lu, S. Slivken, and M. Razeghi, "Single-mode, high-power, mid-infrared, quantum cascade laser phased arrays," *Sci. Rep.*, vol. 8, no. 1, p. 14866, Oct. 2018.

[93] M. Prost, Y. Ling, S. Cakmakyapan, Y. Zhang, K. Zhang, J. Hu, Y. Zhang, and S. J. B. Yoo, "Solid-state MWIR beam steering using optical phased array on germanium-silicon photonic platform," *IEEE Photonics J.*, vol. 11, no. 6, pp. 1–9, Dec. 2019.

[94] J. Midkiff, K. M. Yoo, J.-D. Shin, H. Dalir, M. Teimourpour, and R. T. Chen, "Optical phased array beam steering in the mid-infrared on an InP-based platform," *Optica*, vol. 7, no. 11, pp. 1544–1547, Nov. 2020.

[95] L. Zhang, Y. Li, Y. Hou, Y. Wang, M. Tao, B. Chen, Q. Na, Y. Li, Z. Zhi, X. Liu, X. Li, F. Gao, X. Luo, G.-Q. Lo, and J. Song, "Investigation and demonstration of a high-power handling and large-range steering optical phased array chip," *Opt. Express*, vol. 29, no. 19, pp. 29 755–29 765, Sep. 2021.

[96] A. J. Zilkie, P. Srinivasan, A. Trita, T. Schrans, G. Yu, J. Byrd, D. A. Nelson, K. Muth, D. Lerose, M. Alalusi, K. Masuda, M. Ziebell, H. Abediasl, J. Drake, G. Miller, H. Nykanen, E. Kho, Y. Liu, H. Liang, H. Yang, F. H. Peters, A. S. Nagra, and A. G. Rickman, "Multi-micron silicon photonics platform for highly manufacturable and versatile photonic integrated circuits," *IEEE J. Sel. Top. Quantum Electron.*, vol. 25, no. 5, p. 8200713, Sep. 2019.

[97] SiLC, "The evolution of 3d vision technology," https://www.silc.com/technology/.

[98] J. Sun, E. Timurdogan, A. Yaacobi, E. S. Hosseini, and M. R. Watts, "Large-scale nanophotonic phased array," *Nature*, vol. 493, no. 7431, pp. 195–199, Jan. 2013.

[99] S. A. Miller, Y.-C. Chang, C. T. Phare, M. C. Shin, M. Zadka, S. P. Roberts, B. Stern,

X. Ji, A. Mohanty, O. A. Jimenez Gordillo, U. D. Dave, and M. Lipson, "Large-scale optical phased array using a low-power multi-pass silicon photonic platform," *Optica*, vol. 7, no. 1, pp. 3–6, Jan. 2020.

[100] J. Witzens, "High-Speed silicon photonics modulators," *Proc. IEEE*, vol. 106, no. 12, pp. 2158–2182, Dec. 2018.

[101] R. Soref and B. Bennett, "Electrooptical effects in silicon," *IEEE J. Quantum Electron.*, vol. 23, no. 1, pp. 123–129, Jan. 1987.

[102] G. T. Reed, G. Mashanovich, F. Y. Gardes, and D. J. Thomson, "Silicon optical modulators," *Nat. Photonics*, vol. 4, no. 8, pp. 518–526, Jul. 2010.

[103] M. R. Watts, W. A. Zortman, D. C. Trotter, R. W. Young, and A. L. Lentine, "Vertical junction silicon microdisk modulators and switches," *Opt. Express*, vol. 19, no. 22, pp. 21 989–22 003, Oct. 2011.

[104] P. Dong, L. Chen, and Y.-K. Chen, "High-speed low-voltage single-drive push-pull silicon Mach-Zehnder modulators," *Opt. Express*, vol. 20, no. 6, pp. 6163–6169, Mar. 2012.

[105] E. Temporiti, A. Ghilioni, G. Minoia, P. Orlandi, M. Repossi, D. Baldi, and F. Svelto, "Insights into silicon photonics Mach–Zehnder-Based optical transmitter architectures," *IEEE J. Solid-State Circuits*, vol. 51, no. 12, pp. 3178–3191, Dec. 2016.

[106] W. M. Green, M. J. Rooks, L. Sekaric, and Y. A. Vlasov, "Ultra-compact, low RF power, 10 gb/s silicon Mach-Zehnder modulator," *Opt. Express*, vol. 15, no. 25, pp. 17 106–17 113, Dec. 2007.

[107] S. Akiyama, T. Baba, M. Imai, T. Akagawa, M. Takahashi, N. Hirayama, H. Takahashi, Y. Noguchi, H. Okayama, T. Horikawa, and T. Usuki, "12.5-gb/s operation with 0.29-v 揃 cm $V_\pi L$ using silicon Mach-Zehnder modulator based-on forward-biased pin diode," *Opt. Express*, vol. 20, no. 3, pp. 2911–2923, Jan. 2012.

[108] L. Liao, D. Samara-Rubio, M. Morse, A. Liu, D. Hodge, D. Rubin, U. Keil, and T. Franck, "High speed silicon Mach-Zehnder modulator," *Opt. Express*, vol. 13, no. 8, pp. 3129–3135, Apr. 2005.

[109] J. Fujikata, M. Takahashi, S. Takahashi, T. Horikawa, and T. Nakamura, "High-speed and high-efficiency si optical modulator with MOS junction, using solid-phase crystallization of polycrystalline silicon," *Jpn. J. Appl. Phys.*, vol. 55, no. 4, p. 042202, Mar. 2016.

[110] H. Sattari, T. Graziosi, M. Kiss, T. J. Seok, S. Han, M. C. Wu, and N. Quack, "Silicon photonic MEMS phase-shifter," *Opt. Express*, vol. 27, no. 13, pp. 18 959–18 969, Jun. 2019.

[111] P. Edinger, A. Y. Takabayashi, C. Errando-Herranz, U. Khan, H. Sattari, P. Verheyen, W. Bogaerts, N. Quack, and K. B. Gylfason, "Silicon photonic microelectromechanical

phase shifters for scalable programmable photonics," *Opt. Lett.*, vol. 46, no. 22, pp. 5671–5674, Nov. 2021.

[112] G. Jo, P. Edinger, S. J. Bleiker, X. Wang, A. Y. Takabayashi, H. Sattari, N. Quack, M. Jezzini, J. S. Lee, P. Verheyen, I. Zand, U. Khan, W. Bogaerts, G. Stemme, K. B. Gylfason, and F. Niklaus, "Wafer-level hermetically sealed silicon photonic MEMS," *Photonics Res.*, vol. 10, no. 2, pp. A14–A21, Feb. 2022.

[113] E. Timurdogan, C. V. Poulton, M. J. Byrd, and M. R. Watts, "Electric field-induced second-order nonlinear optical effects in silicon waveguides," *Nat. Photonics*, vol. 11, no. 3, pp. 200–206, Mar. 2017.

[114] U. Chakraborty, J. Carolan, G. Clark, D. Bunandar, G. Gilbert, J. Notaros, M. R. Watts, and D. R. Englund, "Cryogenic operation of silicon photonic modulators based on the DC Kerr effect," *Optica*, vol. 7, no. 10, pp. 1385–1390, Oct. 2020.

[115] R. S. Jacobsen, K. N. Andersen, P. I. Borel, J. Fage-Pedersen, L. H. Frandsen, O. Hansen, M. Kristensen, A. V. Lavrinenko, G. Moulin, H. Ou, C. Peucheret, B. Zsigri, and A. Bjarklev, "Strained silicon as a new electro-optic material," *Nature*, vol. 441, no. 7090, pp. 199–202, May 2006.

[116] B. Chmielak, M. Waldow, C. Matheisen, C. Ripperda, J. Bolten, T. Wahlbrink, M. Nagel, F. Merget, and H. Kurz, "Pockels effect based fully integrated, strained silicon electro-optic modulator," *Opt. Express*, vol. 19, no. 18, pp. 17 212–17 219, Aug. 2011.

[117] B. R. Bennett, R. A. Soref, and J. A. Del Alamo, "Carrier-induced change in refractive index of InP, GaAs and InGaAsP," *IEEE J. Quantum Electron.*, vol. 26, no. 1, pp. 113–122, Jan. 1990.

[118] D. Liang, X. Huang, G. Kurczveil, M. Fiorentino, and R. G. Beausoleil, "Integrated finely tunable microring laser on silicon," *Nat. Photonics*, vol. 10, no. 11, pp. 719–722, Nov. 2016.

[119] J.-H. Han, F. Boeuf, J. Fujikata, S. Takahashi, S. Takagi, and M. Takenaka, "Efficient low-loss InGaAsP/Si hybrid MOS optical modulator," *Nat. Photonics*, vol. 11, no. 8, pp. 486–490, Aug. 2017.

[120] T. Hiraki, T. Aihara, K. Hasebe, K. Takeda, T. Fujii, T. Kakitsuka, T. Tsuchizawa, H. Fukuda, and S. Matsuo, "Heterogeneously integrated III–V/Si MOS capacitor Mach–Zehnder modulator," *Nat. Photonics*, vol. 11, no. 8, pp. 482–485, Aug. 2017.

[121] M. Takenaka, J.-H. Han, F. Boeuf, J.-K. Park, Q. Li, C. P. Ho, D. Lyu, S. Ohno, J. Fujikata, S. Takahashi, and S. Takagi, "III–V/Si hybrid MOS optical phase shifter for Si photonic integrated circuits," *J. Lightwave Technol.*, vol. 37, no. 5, pp. 1474–1483, Mar. 2019.

[122] G. Poberaj, H. Hu, W. Sohler, and P. Günter, "Lithium niobate on insulator (LNOI) for micro-photonic devices," *Laser Photonics Rev.*, vol. 6, no. 4, pp. 488–503, Jul. 2012.

[123] A. Boes, B. Corcoran, L. Chang, J. Bowers, and A. Mitchell, "Status and potential of lithium niobate on insulator (LNOI) for photonic integrated circuits," *Laser Photon. Rev.*, vol. 12, no. 4, p. 1700256, Apr. 2018.

[124] C. Wang, M. Zhang, X. Chen, M. Bertrand, A. Shams-Ansari, S. Chandrasekhar, P. Winzer, and M. Lončar, "Integrated lithium niobate electro-optic modulators operating at CMOS-compatible voltages," *Nature*, vol. 562, no. 7725, pp. 101–104, Oct. 2018.

[125] L. M. Augustin, R. Santos, E. den Haan, S. Kleijn, P. J. A. Thijs, S. Latkowski, D. Zhao, W. Yao, J. Bolk, H. Ambrosius, S. Mingaleev, A. Richter, A. Bakker, and T. Korthorst, "InP-based generic foundry platform for photonic integrated circuits," *IEEE J. Sel. Top. Quantum Electron.*, vol. 24, no. 1, p. 6100210, Jan. 2018.

[126] S. Arafin and L. A. Coldren, "Advanced InP photonic integrated circuits for communication and sensing," *IEEE J. Sel. Top. Quantum Electron.*, vol. 24, no. 1, p. 6100612, Jan. 2018.

[127] J. J. G. M. van der Tol, Y. Jiao, J. P. Van Engelen, V. Pogoretskiy, A. A. Kashi, and K. Williams, "InP membrane on silicon (IMOS) photonics," *IEEE J. Quantum Electron.*, vol. 56, no. 1, p. 6300107, Feb. 2020.

[128] N. C. Harris, Y. Ma, J. Mower, T. Baehr-Jones, D. Englund, M. Hochberg, and C. Galland, "Efficient, compact and low loss thermo-optic phase shifter in silicon," *Opt. Express*, vol. 22, no. 9, pp. 10 487–10 493, May 2014.

[129] M. Jacques, A. Samani, E. El-Fiky, D. Patel, Z. Xing, and D. V. Plant, "Optimization of thermo-optic phase-shifter design and mitigation of thermal crosstalk on the SOI platform," *Opt. Express*, vol. 27, no. 8, pp. 10 456–10 471, Apr. 2019.

[130] S. Liu, J. Feng, Y. Tian, H. Zhao, L. Jin, B. Ouyang, J. Zhu, and J. Guo, "Thermo-optic phase shifters based on silicon-on-insulator platform: state-of-the-art and a review," *Frontiers of Optoelectronics*, vol. 15, no. 1, p. 9, Apr. 2022.

[131] K. Van Acoleyen, W. Bogaerts, and R. Baets, "Two-dimensional dispersive off-chip beam scanner fabricated on silicon-on-insulator," *IEEE Photonics Technol. Lett.*, vol. 23, no. 17, pp. 1270–1272, Sep. 2011.

[132] N. Dostart, B. Zhang, A. Khilo, M. Brand, K. Al Qubaisi, D. Onural, D. Feldkhun, K. H. Wagner, and M. A. Popović, "Serpentine optical phased arrays for scalable integrated photonic lidar beam steering," *Optica*, vol. 7, no. 6, pp. 726–733, Jun. 2020.

[133] A. Rizzo, U. Dave, A. Novick, A. Freitas, S. P. Roberts, A. James, M. Lipson, and K. Bergman, "Fabrication-robust silicon photonic devices in standard sub-micron silicon-on-insulator processes," 2022, arXiv:2205.11481.

[134] Y. Misugi, H. Okayama, and T. Kita, "Demonstration of 2D beam steering using large-scale passive optical phased array enabled by multimode waveguides with reduced phase

error," *Appl. Phys. Express*, vol. 15, no. 10, p. 102002, Sep. 2022.

[135] L. Chrostowski, X. Wang, J. Flueckiger, Y. Wu, Y. Wang, and S. Talebi Fard, "Impact of fabrication non-uniformity on chip-scale silicon photonic integrated circuits," in *Optical Fiber Communication Conference*, Mar. 2014, p. Th2A.37.

[136] Y. Yang, Y. Ma, H. Guan, Y. Liu, S. Danziger, S. Ocheltree, K. Bergman, T. Baehr-Jones, and M. Hochberg, "Phase coherence length in silicon photonic platform," *Opt. Express*, vol. 23, no. 13, pp. 16 890–16 902, Jun. 2015.

[137] W. Li, J. Chen, D. Liang, D. Dai, and Y. Shi, "Silicon optical phased array with calibration-free phase shifters," *Opt. Express*, vol. 30, no. 24, p. 44029, Nov. 2022.

[138] M. J. R. Heck, J. F. Bauters, M. L. Davenport, D. T. Spencer, and J. E. Bowers, "Ultra-low loss waveguide platform and its integration with silicon photonics," *Laser Photon. Rev.*, vol. 8, no. 5, pp. 667–686, Sep. 2014.

[139] C. V. Poulton, M. J. Byrd, M. Raval, Z. Su, N. Li, E. Timurdogan, D. Coolbaugh, D. Vermeulen, and M. R. Watts, "Large-scale silicon nitride nanophotonic phased arrays at infrared and visible wavelengths," *Opt. Lett.*, vol. 42, no. 1, pp. 21–24, Jan. 2017.

[140] B. Bhandari, C. Wang, J.-Y. Gwon, J.-M. Heo, S.-Y. Ko, M.-C. Oh, and S.-S. Lee, "Dispersive silicon-nitride optical phased array incorporating arrayed waveguide delay lines for passive line beam scanning," *Sci. Rep.*, vol. 12, no. 1, p. 18759, Nov. 2022.

[141] B. V. Gurses, R. Fatemi, A. Khachaturian, and A. Hajimiri, "Large-scale crosstalk-corrected thermo-optic phase shifter arrays in silicon photonics," *IEEE J. Sel. Top. Quantum Electron.*, vol. 28, no. 6, p. 6101009, Nov. 2022.

[142] S. Guerber, D. Fowler, J. Faugier-Tovar, K. A. Carim, B. Delplanque, and B. Szelag, "Wafer-level calibration of large-scale integrated optical phased arrays," *Opt. Express*, vol. 30, no. 20, pp. 35 246–35 255, Sep. 2022.

[143] W. Ma, S. Tan, K. Wang, W. Guo, Y. Liu, L. Liao, L. Zhou, J. Zhou, X. Li, L. Liang, and W. Li, "Practical two-dimensional beam steering system using an integrated tunable laser and an optical phased array," *Appl. Opt.*, vol. 59, no. 32, pp. 9985–9994, Nov. 2020.

[144] T. Komljenovic and P. Pintus, "On-chip calibration and control of optical phased arrays," *Opt. Express*, vol. 26, no. 3, pp. 3199–3210, Feb. 2018.

[145] H. Zhang, Z. Zhang, C. Peng, and W. Hu, "Phase calibration of on-chip optical phased arrays via interference technique," *IEEE Photonics J.*, vol. 12, no. 2, pp. 1–10, Apr. 2020.

[146] S. Mano and T. Katagi, "A method for measuring amplitude and phase of each radiating element of a phased array antenna," *Electron. Commun. Jpn. Part 1 Commun.*, vol. 65, no. 5, pp. 58–64, 1982.

[147] Q. Zhang, L. Zhang, Z. Li, W. Wu, G. Wang, X. Sun, and W. Zhang, "An antenna array initial condition calibration method for integrated optical phased array," *Acta Photonica Sin.*, vol. 49, no. 7, p. 0726001, 2020.

[148] J. O. Kjellman, M. Prost, A. Marinins, H. K. Tyagi, T. D. Kongnyuy, S. Dwivedi, M. S. Dahlem, P. Soussan, X. Rottenberg, and R. Jansen, "Densely integrated phase interrogators for low-complexity on-chip calibration of optical phased arrays," *J. Lightwave Technol.*, vol. 40, no. 16, pp. 5660–5667, Aug. 2022.

[149] A. Hosseini, D. Kwong, Y. Zhao, Y.-S. Chen, F. Crnogorac, R. F. W. Pease, and R. T. Chen, "Unequally spaced waveguide arrays for silicon nanomembrane-based efficient large angle optical beam steering," *IEEE J. Sel. Top. Quantum Electron.*, vol. 15, no. 5, pp. 1439–1446, Sep. 2009.

[150] D. Kwong, A. Hosseini, Y. Zhang, and R. T. Chen, "1×12 unequally spaced waveguide array for actively tuned optical phased array on a silicon nanomembrane," *Appl. Phys. Lett.*, vol. 99, no. 5, p. 051104, Aug. 2011.

[151] T. Komljenovic, R. Helkey, L. Coldren, and J. E. Bowers, "Sparse aperiodic arrays for optical beam forming and LIDAR," *Opt. Express*, vol. 25, no. 3, pp. 2511–2528, Feb. 2017.

[152] B. Yang, H. Chen, S. Yang, and M. Chen, "An improved aperiodic OPA design based on large antenna spacing," *Opt. Commun.*, vol. 475, p. 125852, Nov. 2020.

[153] A. Kazemian, P. Wang, Y. Zhuang, and Y. Yi, "Optimization of the silicon-based aperiodic optical phased array antenna," *Opt. Lett.*, vol. 46, no. 4, pp. 801–804, Feb. 2021.

[154] M.-J. Sun and J.-M. Zhang, "Single-pixel imaging and its application in three-dimensional reconstruction: a brief review," *Sensors*, vol. 19, no. 3, p. 732, Feb. 2019.

[155] M. P. Edgar, G. M. Gibson, and M. J. Padgett, "Principles and prospects for single-pixel imaging," *Nat. Photonics*, vol. 13, no. 1, pp. 13–20, Jan. 2019.

[156] G. M. Gibson, S. D. Johnson, and M. J. Padgett, "Single-pixel imaging 12 years on: a review," *Opt. Express*, vol. 28, no. 19, pp. 28 190–28 208, Sep. 2020.

[157] A. Gatti, E. Brambilla, M. Bache, and L. A. Lugiato, "Ghost imaging with thermal light: Comparing entanglement and classical correlation," *Phys. Rev. Lett.*, vol. 93, no. 9, p. 093602, Aug. 2004.

[158] J. H. Shapiro, "Computational ghost imaging," *Phys. Rev. A*, vol. 78, no. 6, p. 061802, Dec. 2008.

[159] Y. Bromberg, O. Katz, and Y. Silberberg, "Ghost imaging with a single detector," *Phys. Rev. A*, vol. 79, no. 5, p. 053840, May 2009.

[160] O. Katz, Y. Bromberg, and Y. Silberberg, "Compressive ghost imaging," *Appl. Phys.*

Lett., vol. 95, no. 13, p. 131110, Sep. 2009.

[161] R. G. Baraniuk, "Compressive sensing," *IEEE Signal Process. Mag.*, vol. 24, no. 4, pp. 118–121, Jul. 2007.

[162] M. F. Duarte, M. A. Davenport, D. Takhar, J. N. Laska, T. Sun, K. F. Kelly, and R. G. Baraniuk, "Single-pixel imaging via compressive sampling," *IEEE Signal Process. Mag.*, vol. 25, no. 2, pp. 83–91, Mar. 2008.

[163] S. S. Welsh, M. P. Edgar, R. Bowman, P. Jonathan, B. Sun, and M. J. Padgett, "Fast full-color computational imaging with single-pixel detectors," *Opt. Express*, vol. 21, no. 20, pp. 23 068–23 074, Oct. 2013.

[164] W. C. Babcock, "Intermodulation interference in radio systems frequency of occurrence and control by channel selection," *The Bell System Technical Journal*, vol. 32, no. 1, pp. 63–73, Jan. 1953.

[165] J. P. Robinson, "Optimum Golomb rulers," *IEEE Trans. Comput.*, no. 12, pp. 943–944, Dec. 1979.

[166] J. Robinson and A. Bernstein, "A class of binary recurrent codes with limited error propagation," *IEEE Trans. Inf. Theory*, vol. 13, no. 1, pp. 106–113, Jan. 1967.

[167] J. B. Shearer, "Some new optimum Golomb rulers," *IEEE Trans. Inf. Theory*, vol. 36, no. 1, pp. 183–184, Jan. 1990.

[168] A. Dollas, W. T. Rankin, and D. McCracken, "A new algorithm for Golomb ruler derivation and proof of the 19 mark ruler," *IEEE Trans. Inf. Theory*, vol. 44, no. 1, pp. 379–382, Jan. 1998.

[169] "OGR-27 / Overall Project Stats," https://stats.distributed.net/projects.php?project_id=27.

[170] M. Atkinson, N. Santoro, and J. Urrutia, "Integer sets with distinct sums and differences and carrier frequency assignments for nonlinear repeaters," *IEEE Trans. Commun.*, vol. 34, no. 6, pp. 614–617, Jun. 1986.

[171] A. W. Lam and D. V. Sarwate, "On optimum time-hopping patterns," *IEEE Trans. Commun.*, vol. 36, no. 3, pp. 380–382, Mar. 1988.

[172] K. Drakakis, "A review of the available construction methods for Golomb rulers," *Adv. Math. Commun.*, vol. 3, no. 3, pp. 235–250, 2009.

[173] N. Ayari, T. Van Luong, and A. Jemai, "A hybrid genetic algorithm for Golomb ruler problem," in *ACS/IEEE International Conference on Computer Systems and Applications - AICCSA 2010*, May 2010, pp. 1–4.

[174] M. M. A. Polash, M. A. H. Newton, and A. Sattar, "Constraint-based search for optimal Golomb rulers," *Journal of Heuristics*, vol. 23, no. 6, pp. 501–532, Dec. 2017.

[175] S. Bansal, "A comparative study of nature-inspired metaheuristic algorithms in search of near-to-optimal Golomb rulers for the FWM crosstalk elimination in WDM systems,"

Appl. Artif. Intell., vol. 33, no. 14, pp. 1199–1265, Dec. 2019.

[176] C. A. M. Ojeda, D. F. D. Urbano, and C. A. T. Solarte, "Near-Optimal g-Golomb rulers," *IEEE Access*, vol. 9, pp. 65 482–65 489, 2021.

[177] A. Moffet, "Minimum-redundancy linear arrays," *IEEE Trans. Antennas Propag.*, vol. 16, no. 2, pp. 172–175, Mar. 1968.

[178] J. P. Costas, "A study of a class of detection waveforms having nearly ideal range—doppler ambiguity properties," *Proc. IEEE*, vol. 72, no. 8, pp. 996–1009, Aug. 1984.

[179] S. W. Golomb, "Algebraic constructions for Costas arrays," *J. Combin. Theory Ser. A*, vol. 37, no. 1, pp. 13–21, Jul. 1984.

[180] S. W. Golomb and H. Taylor, "Constructions and properties of Costas arrays," *Proc. IEEE*, vol. 72, no. 9, pp. 1143–1163, Sep. 1984.

[181] J. K. Beard, "Generating Costas arrays to order 200," in *2006 40th Annual Conference on Information Sciences and Systems*, Mar. 2006, pp. 1130–1133.

[182] J. K. Beard, J. C. Russo, K. G. Erickson, M. C. Monteleone, and M. T. Wright, "Costas array generation and search methodology," *IEEE Trans. Aerosp. Electron. Syst.*, vol. 43, no. 2, pp. 522–538, Apr. 2007.

[183] L. Barker, K. Drakakis, and S. Rickard, "On the complexity of the verification of the Costas property," *Proc. IEEE*, vol. 97, no. 3, pp. 586–593, Mar. 2009.

[184] M. J. E. Golay, "Point arrays having compact, nonredundant autocorrelations," *J. Opt. Soc. Am.*, vol. 61, no. 2, pp. 272–273, 1971.

[185] F. Cassaing and L. M. Mugnier, "Optimal sparse apertures for phased-array imaging," *Opt. Lett.*, vol. 43, no. 19, pp. 4655–4658, Oct. 2018.

[186] P. Pal and P. P. Vaidyanathan, "Nested arrays: A novel approach to array processing with enhanced degrees of freedom," *IEEE Trans. Signal Process.*, vol. 58, no. 8, pp. 4167–4181, Aug. 2010.

[187] S. Qin, Y. D. Zhang, and M. G. Amin, "Generalized coprime array configurations for direction-of-arrival estimation," *IEEE Trans. Signal Process.*, vol. 63, no. 6, pp. 1377–1390, Mar. 2015.

[188] C.-L. Liu and P. P. Vaidyanathan, "Super nested arrays: Linear sparse arrays with reduced mutual Coupling—Part I: Fundamentals," *IEEE Trans. Signal Process.*, vol. 64, no. 15, pp. 3997–4012, Aug. 2016.

[189] A. Ahmed and Y. D. Zhang, "Generalized non-redundant sparse array designs," *IEEE Trans. Signal Process.*, vol. 69, pp. 4580–4594, 2021.

[190] T. Su, G. Liu, K. E. Badham, S. T. Thurman, R. L. Kendrick, A. Duncan, D. Wuchenich, C. Ogden, G. Chriqui, S. Feng, J. Chun, W. Lai, and S. J. B. Yoo, "Interferometric imaging using Si_3N_4 photonic integrated circuits for a SPIDER imager," *Opt. Express*, vol. 26, no. 10, pp. 12 801–12 812, May 2018.

[191] S. Roberts, X. Ji, J. Cardenas, M. Corato-Zanarella, and M. Lipson, "Measurements and modeling of atomic scale sidewall roughness and losses in integrated photonic devices," *Adv. Opt. Mater.*, vol. 10, no. 18, p. 2102073, Sep. 2022.

[192] Micromodule Technology, Inc., http://www.micro-module.co.jp/.

[193] W.-K. Ma, T.-H. Hsieh, and C.-Y. Chi, "DOA estimation of quasi-stationary signals via Khatri-Rao subspace," in *2009 IEEE International Conference on Acoustics, Speech and Signal Processing*. ieeexplore.ieee.org, Apr. 2009, pp. 2165–2168.

[194] G. H. Golub and C. F. Van Loan, *Matrix computations*. 2715 North Charles Street, Baltimore, Maryland 21218-4363: JHU Press, 2013.

[195] P. C. Hansen, "The truncated SVD as a method for regularization," *BIT Numer. Math.*, vol. 27, no. 4, pp. 534–553, Dec. 1987.

[196] K. Komatsu, "Research on integrated InP optical phased array for high-speed imaging applications," Master's thesis, The University of Tokyo, Mar. 2017.

[197] S. A. Emara, "Study on single-pixel speckle imaging based on optical phased arrays with reduced complexity," Ph.D. dissertation, The University of Tokyo, Sep. 2021.

[198] A. Yariv and P. Yeh, *Photonics: Optical Electronics in Modern Communications*. Oxford university press, 2007.

[199] J. D. Joannopoulos, S. G. Johnson, J. N. Winn, and R. D. Meade, *Photonic Crystals: Molding the Flow of Light*, 2nd ed. Princeton University Press, Mar. 2008.

[200] S. L. Chuang, *Physics of Photonic Devices*. John Wiley & Sons, Nov. 2012.